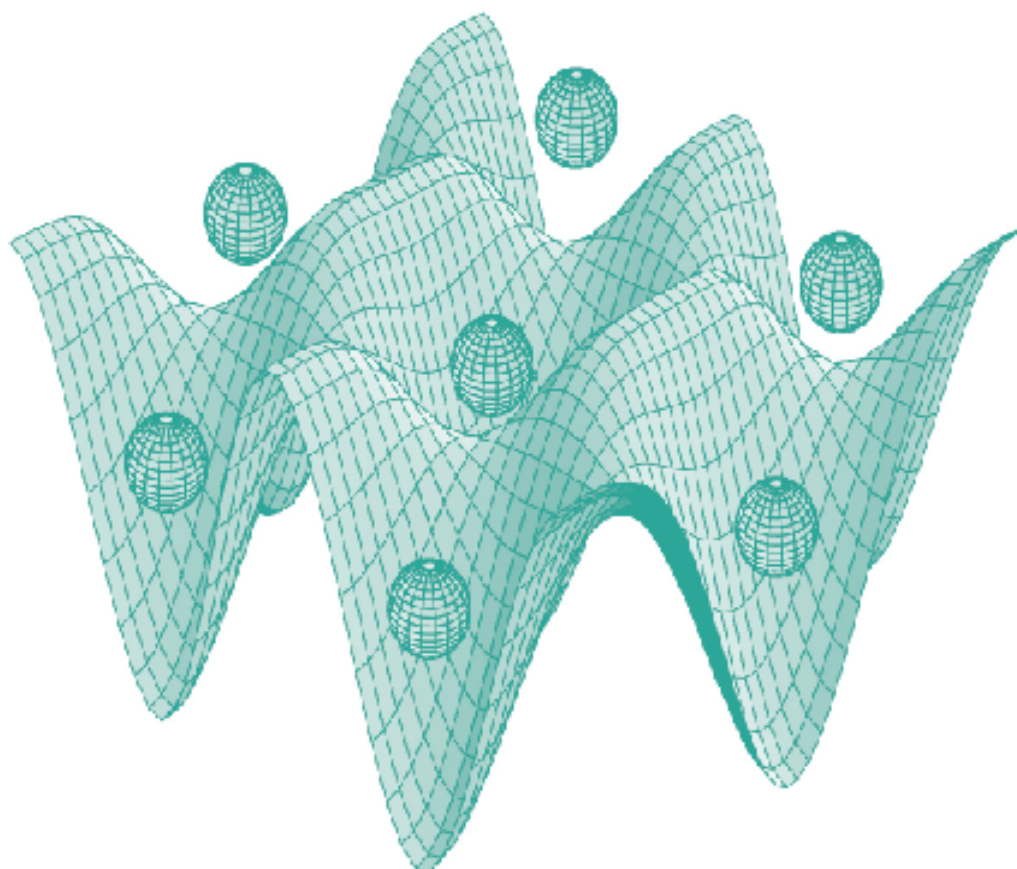




STUDIA UNIVERSITATIS
BABEȘ-BOLYAI



PHYSICA

2/2016

**STUDIA
UNIVERSITATIS BABEŞ-BOLYAI
PHYSICA**

**2/2016
December**

EDITORIAL OFFICE OF STUDIA UBB PHYSICA:

1, M. Kogălniceanu St., Cluj-Napoca, ROMANIA, Phone: +40 264 405300

http://www.studia.ubbcluj.ro/serii/physica/index_en.html

EDITOR-IN-CHIEF:

Professor Aurel POP, Ph.D., Babeş-Bolyai University, Cluj-Napoca, Romania

EDITORIAL BOARD:

Professor Simion AŞTILEAN, Ph.D., Babeş-Bolyai University, Cluj-Napoca, Romania

Professor Istvan BALLAI, Ph.D., The University of Sheffield, United Kingdom

Zoltan BALINT, Ph.D., Ludwig Boltzmann Institute Graz, Austria

Professor Titus BEU, Ph.D., Babeş-Bolyai University, Cluj-Napoca, Romania

Prof. Boldizsár JANKÓ, Ph.D., University of Notre Dame, USA

Professor Emil BURZO, Ph.D., Babeş-Bolyai University, Cluj-Napoca, Romania,
member of Romanian Academy

Professor Vasile CHIŞ, Ph.D., Babeş-Bolyai University, Cluj-Napoca, Romania

Professor Olivier ISNARD, Ph.D., University J. Fourier & Institut Neel, Grenoble,
France

Professor Ladislau NAGY, Ph.D., Babeş-Bolyai University, Cluj-Napoca, Romania

Professor Zoltan NEDA, Ph.D., Babeş-Bolyai University, Cluj-Napoca, Romania

Professor Jurgen POPP, Ph.D., Dr.h.c., Institute of Physical Chemistry, Friedrich-
Schiller-University Jena, Germany

Professor György SZABÓ, Ph.D., Research Institute for Technical Physics and
Materials Science, Hungarian Academy of Sciences, Budapest, Hungary

Professor Simion SIMON, Ph.D., Babeş-Bolyai University, Cluj-Napoca, Romania

Professor Romulus TETEAN, Ph.D., Babeş-Bolyai University, Cluj-Napoca, Romania

Professor Dietrich ZAHN, Ph.D., Dr.h.c., Technical University, Chemnitz, Germany

EXECUTIVE EDITOR:

Lecturer Claudiu LUNG, Ph.D., Babeş-Bolyai University, Cluj-Napoca, Romania

YEAR
MONTH
ISSUE

Volume 61 (LXI) 2016
DECEMBER
2

STUDIA UNIVERSITATIS BABEȘ-BOLYAI PHYSICA

2

Dedicated to Professor Dr. Sorin Dan Anghel on His 65th Anniversary

STUDIA UBB EDITORIAL OFFICE: B.P. Hasdeu no. 51, 400371 Cluj-Napoca, Romania,
Phone + 40 264 405352

CUPRINS – CONTENT – SOMMAIRE – INHALT

A. POP, <i>Foreword: Anniversary of Professor Sorin Dan Anghel</i>	5
M. ABDALLA, LARISA MILENA ȚIMBOLMAȘ, N. LEOPOLD, SANDA CÎMPEAN, V. CHIȘ, <i>Excited State Properties of the Camphorquinone Photoinitiator</i>	7
S. BORBÉLY, <i>Nonuniform Numerical Grid for the Numerical Solution of the Schrödinger Equation</i>	21
R. DUDRIC, G. SOUCA, I.G. DEAC, R. TETEAN, <i>Magnetocaloric and Magnetic Properties of Nanocrystalline $La_{0.75}Pb_{0.25}MnO_3$ Synthesized by High Energy Ball Milling</i>	31

E. FILEP, L. KENÉZ, N. KUTASI, L. FERENCZ, <i>Formation of Ammonia in a Linear Plasma Reactor</i>	39
I. GROSU, <i>Spin Susceptibility in Two Dimensions</i>	49
R. HIRIAN, S. MICAN, O. ISNARD, L. BARBU, V. POP, <i>Effect of Starting Powder Premixing on the Interphase Exchange Coupling in Nd₂Fe₁₄B + 10 WT % Fe Nanocomposites Obtained Trough Mechanical Milling</i>	55
A.S. MARE, A. MARCU, <i>On the Structure and Stability of Neutron Stars. A General Relativistic Approach</i>	65
GABRIELA SOUCA, S. MICAN, A. STEFANCU, V. CHIȘ, R. TETEAN, N. LEOPOLD, <i>Structural and Magnetic Characterization of Fe₃O₄ Nanoparticles Synthesized at Room Temperature</i>	83
M. TODICA, C.V. POP, O. BALIBANU, <i>Simple Method for Investigation of Low Frequency Damped Oscillations of Elastomers</i>	91
A.M. JUNCAN, C. LUNG, <i>Formulation and Optimizing of a Anti-Aging Cosmetic Cream</i>	101

Foreword

Anniversary of Professor Sorin Dan ANGHEL

Professor Sorin Dan ANGHEL was born in 1951, Sighisoara, Romania, and graduated Babes-Bolyai University Cluj-Napoca in 1975. After graduating Faculty of Physics, he was assigned by the Ministry of Education to work as a physicist in industry at Geologic and Geophysics Prospections for Hydrocarbons Enterprise, Bucharest (1975-1979). Between 1979-1987 continued to work as a physicist at Heavy Machinery Factory, Cluj-Napoca. Since 1984 to 1991 he held activities at Research Institute for Analytical Instrumentation (ICIA) Cluj-Napoca, as Senior Research Scientist III in Laboratory for Gas Discharges and Atomic Spectroscopy. Prof. S.D. Anghel earned in 1991 his PhD in Physics.

Since 1991 worked at Babeş-Bolyai University, Faculty of Physics as teaching assistant professor (1991-1999), associate professor (1999-2003) and professor (2003-present), respectively.

Professor Sorin Dan ANGHEL presented courses, lectures and laboratory for disciplines: Electronics, Instrumentation and sensors and Plasma Physics.

Understanding the importance of modern directions in science and technologies, he introduced new information from the field of applied physics, in sensors and electronic courses. The courses are very clearly presented and at high scientific level. The teaching activities performed by Sorin Dan ANGHEL are much appreciated by the students.

At doctoral school presented lectures on “Nanostructures and polymeric systems”, and in the position of PhD coordinator he supervised doctoral theses.

The scientific research activity of Sorin Dan ANGHEL is directed over plasma study, particularly over the radiofrequency(RF) plasmas generated at atmospheric pressure in argon, helium, air etc.

The main directions of research are:

- a) The building of devices for generating of Inductively Coupled Plasma (ICP) - 27.12 MHz, 1-3 kW, Capacitively Coupled Plasma (CCP) - 10 MHz, 0.5-80 W, Dielectric Barrier Discharge (DBD) - 20 kHz-2 MHz, 1-20 W and Plasma in/on Liquids - 10 MHz, 16 W, respectively;

- b) Fundamental studies over the generated plasmas: plasma parameters, electrical modelling, studies based on Fourier analysis of the influence of the plasma on the waveform of generated oscillations by the RF oscillator;
- c) Applications of generated plasmas at : spectral sources for analysis of liquid samples, spectral sources for direct analysis of conductive and nonconductive solid samples, treatment of microorganisms by non-thermal capacitively coupled plasma, nanoparticle synthesis, dyes degradation and plasma activated water.

The scientific results of Prof. Sorin Dan ANGHEL were published in 60 papers in ISI quoted journals (*J. Phys. D: Appl. Phys.*, *Plasma Sci. Technol.*, *IEEE Transactions on Plasma Science*, *J. Nanopart. Res.*, *J. Electrostat.*, *Spectrochim. Acta Part B*, *Nucl. Instr. and Methods in Phys. Research Sect. B*, *Plasma Sourc. Sci. and Technol.*, *Meas. Sci. Technol.*, *J. Anal. At. Spectrom.*, *Mikrochimica Acta*, *Analytical Letters*, *Talanta*, *Roum. Journ. Phys.*, etc.). He has Hirsch indices $H=10$ (Scopus 2017).

His theoretical and experimental researches as well as his pedagogic experience were fructified into a series of 10 books, frequently used by the students in area of their courses. These are remarkable for their accuracy and clarity as well as scientific level the monographies: "Plasma physics and applications", "Fundamentals of analogic and digital electronics" (Cluj, Romania, University Press 2001 and 2007), and Thermally Non-aggressive Atmospheric Pressure Plasma (LAP LAMBERT Academic Publishing, Saarbrucken 2013).

Professor Sorin Dan ANGHEL is member of Romanian and international scientific societies as: Romanian Physical Society, European Physical Society, Balkan Physical Society.

He has held several management positions: Dean of the Faculty of Physics, Cluj-Napoca, Head of the Plasma Physics Laboratory, Senat member of "Babes-Bolyai" University, Member of Faculty of Physics Council.

Professor Sorin Dan ANGHEL has extensive experience in the management of national / international scientific projects, gaining many scientific contracts and grants.

Professor Sorin Dan ANGHEL was member of the Editorial Board of Journal *Studia UBB Physica*, and reader to a series of international scientific journals. He was invited to sustain plenary presentations at many national and international meetings and conferences.

Today, at sixty-five years old, Prof. Sorin Dan ANGHEL continue his scientific activity work with doctoral students.

Happy birthday and all the best!

Prof.dr. Aurel Pop

Dean-Faculty of Physics

Dedicated to Professor Dr. Sorin Dan Anghel on His 65th Anniversary

EXCITED STATE PROPERTIES OF THE CAMPHORQUINONE PHOTOINITIATOR

M. ABDALLA^a, LARISA MILENA ȚIMBOLMAȘ^a, N. LEOPOLD^a,
SANDA CÎMPEAN^b, V. CHIȘ^{a*}

ABSTRACT. The photophysics of the photoinitiator Camphorquinone was investigated computationally in this work, by using time-dependent Density Functional Theory methods. DFT calculations. We fully assigned the UV-Vis electronic transition of the Camphorquinone monomer. Moreover, the emission energy as well as the structural differences between the geometries of the molecule in the ground and excited state have been analyzed.

Keywords: *Camphorquinone; photo-initiator; excited state; TD-DFT*

1. INTRODUCTION

The commonly used resin based composites (RBCs) in dentistry are based on poly methyl methacrylates filled with particles whose role is to give strength, wear resistance and the reduction of the polymerization shrinkage [1, 2]. Basically, a dental composite contains a resin based matrix, fillers and coupling agents. The resin based matrix (Fig.1) consists of monomers (e.g., Bisphenol A-glycidyl methacrylate (Bis-GMA), Urethane dimethacrylate (UDMA)), low viscosity co-monomers like Triethylene glycol dimethacrylate (TEGDMA), initiators, co-initiators, inhibitors and pigments.

^a Babeș-Bolyai University, Faculty of Physics, 1 Kogălniceanu, Cluj-Napoca, Romania

^b Department of Conservative Dentistry and Endodontics, Faculty of Dental Medicine, Iuliu Hatieganu University of Medicine and Pharmacy, 33 Motilor, Cluj-Napoca, Romania

* Corresponding author: vasile.chis@phys.ubbcluj.ro

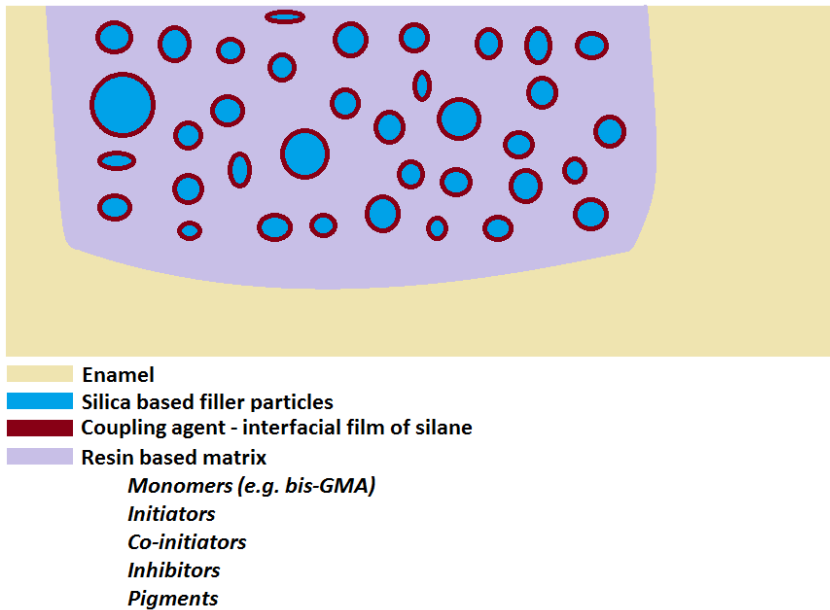


Fig. 1. Ingredients of the composite materials used in dentistry

Polymerization Initiators (photosensitizer) for new composites are chemical compounds able to absorb light and to initiate the polymerization process. Even though there are three primary absorbers in the composite (the initiator, the monomer/co-monomer resin and the pigment added to achieve the correct tooth shade) only the light absorbed by the initiator will be used in the photo-curing process [3].

One of the most used initiator in the commercially available composites is Camphorquinone (CQ, Fig.2), for which the absorption range corresponds to visible light wavelength between 400-500 nm, with λ_{\max} at about 470 nm. CQ abstracts a hydrogen atom from the tertiary amine added as co-initiator, resulting in free-radical generation. Obviously, the optimum efficiency is obtained when the absorption peak of the photoinitiator is in resonance with the spectral emission from the light curing unit.

Polymerization co-initiator is a chemical compound that interacts with the activated camphorquinone to produce reactive species able to initiate and sustain the polymerization process. The type of co-initiator as well as the photoinitiator/coinitiator ratio can affect drastically the degree of conversion, polymerization rate or the biocompatibility of the materials [4].

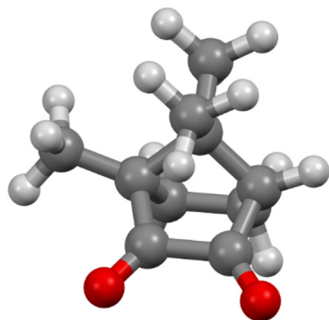


Fig. 2. Optimized molecular structure of Camphorquinone at B3LYP/6-311+g(2d,p) level of theory

Tertiary amines are commonly used as co-initiators in the resin-based composites. Examples of such amines used in the photoactivated composites are basically Dimethylaminoethylmetacrylate (DMAEMA) and Ethyl-4-dimethylamino-benzoate (EDMAB, see Fig. 3).

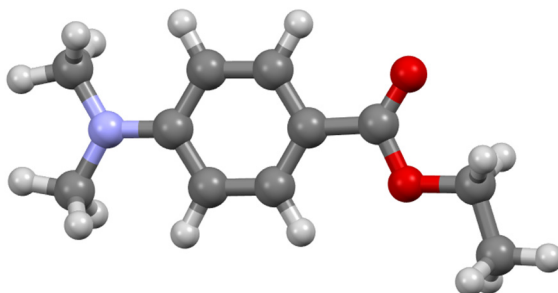


Fig. 3. Optimized molecular structure of EDMAB at B3LYP/6-311+g(2d,p) level of theory

In this work, we aimed to shed more light on the excited state of camphorquinone photoinitiator. For this purpose we calculated both, the absorption and emission energies for this compound and compared the computational data to the reported experimental results [5, 6]. Also, an analysis of the electronic transitions is included here, as well as the geometry of the molecule in its first excited state.

2. COMPUTATIONAL DETAILS

Absorption spectrum and the geometry of the CQ in the first excited state was calculated using the time-dependent DFT (TD-DFT) methodology [7], implemented in the Gaussian09 package [8]. For these purposes we used the B3LYP functional [9-12], coupled with the 6-311+g(2d,p) basis set.

The simulated UV-vis spectrum of CQ in the 140–500 nm range has been obtained by summation of the contributions from transitions to the first 30 singlet excited electronic states. The UV spectral line-shapes were convoluted with Gaussian functions with FWHM of 0.44 eV.

The nature of the excited states has been analyzed using the Natural Transition Orbitals (NTO) formalism proposed by Martin [13], that offers compact description of the electronic excitations with the advantage that only one or two occupied/virtual pairs of orbitals are enough for a clear interpretation of the physical nature of the excited states involved in absorption and emission processes [14].

The solvent effects have been considered by using the implicit Polarizable Continuum Model (PCM) [15].

All the calculations have been performed with the Gaussian Rev E.01 [8] software package and the results have been analyzed using the GaussView program [16].

Figures representing the structures of CQ were have been created using the Mercury 3.3 [17] software package.

3. RESULTS AND DISCUSSIONS

3.1 Absorption spectrum of Camphorquinone

Camphorquinone (CQ) is widely used as a type II photoinitiator for the photocuring of restorative dental composite resins [18, 19]. The excitation energy of the photoinitiator must be in resonance with the energy of the photons emitted by the lamps or LEDs used for curing. Moreover, another important requirement is to have no competing absorptions by the components of the composites at the excitation energy of the photoinitiator. Thus, from practical applications, information about the photoinitiator absorption spectrum is essential [20 Neu05]. From fundamental perspective, of great importance is also the geometry change of the photoinitiator as a result of electronic excitation.

The UV-Vis spectra of CQ were reported recently by Longhi et al. [5] in ethanol, Okulus et al. in chloroform and in methanol [6]. The experimental spectra show a weak transition around 470 nm, with a slight influence of the solvent.

Fig. 4 illustrates the calculated absorption spectrum of CQ in acetonitrile, at PCM-B3LYP/6-311+G(2d,p) level of theory. The most intense electronic transitions for this compound occur in the UV range. A weak transition is calculated at 484 nm, in the visible range and this corresponds to the λ_{\max} of CQ and it is correlated to the activating energy of the photoinitiator. Both, the band position and molar absorptivity for this transition are in excellent agreement with the experimental data.

Acetonitrile was used as solvent because of its polar aprotic nature (dipole moment: 3.92D), and consequently it will hardly be involved in intermolecular hydrogen bonds with the CQ monomers. For comparison purposes, ethanol was also used as implicit solvent but no significant difference was observed in the calculated UV-Vis spectrum compared to acetonitrile.

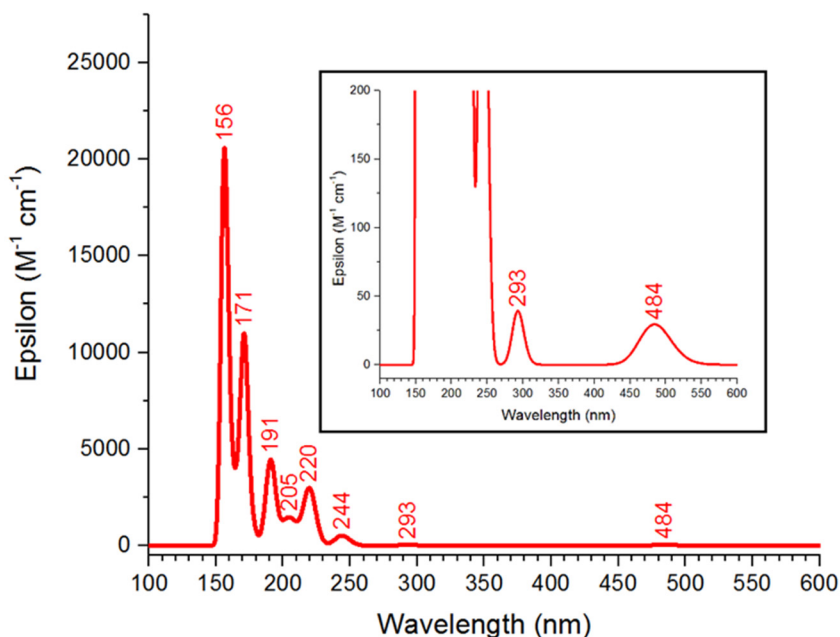


Fig. 4. B3LYP/6-311+g(2d,p) calculated absorption spectrum of camphorquinone in acetonitrile (PCM was used as solvent model; inset: zoom in the low-values region of the molar absorptivity)

All the calculated excitation energies of the CQ monomer in acetonitrile are listed in Table 1. To better understand the properties of the excited states of CQ we obtained the NTOs based on the calculated density matrices.

As seen in Fig. 4 and Table 1, the most intense transitions appear at wavelengths between 130 and 260 nm and they are due to transitions to S26, S19, S11, S5 and S3 excited states. S3, S5 and S11 excited states involve the frontier orbitals HOMO and LUMO as final or initial state of transition, while the S19 and S26 states imply transition between either low lying occupied orbitals like HOMO-10, HOMO-12 and HOMO-14 or to high unoccupied orbitals like LUMO9. On the other hand, the transition corresponding to the excitation to the S2 state is predicted at 272 nm and it is due to the HOMO-1-> LUMO and HOMO-2-> LUMO transitions with 63 % and 13 % contributions, respectively.

The state of interest for CQ as a photoinitiator is S1, with the calculated $\lambda = 484$ nm, resulted as a 97 % HOMO-LUMO transition. As seen in Fig. 4, this transition, but also the transition to the S2 state is characterized by a much lower molar absorptivity than the excitations calculated at lower wavelengths.

Table 1. Theoretical UV-Vis absorption spectral data calculated for the CQ monomer and in acetonitrile at PCM-B3LYP/6-311+G(2d,p) level of theory

Excited state	λ (nm)	$f^a)$	transitions ^{b)}	Contributions (%) ^{c)}
S1	446.0	0.0003	H→L	97
S2	272.0	0.0002	H-1→L	63
			H-2→L	13
S3	214	0.0084	H-2→L	60
			H-3→L	29
S5	190	0.0265	H-3→L	65
S11	172	0.0484	H→L+2	60
S19	151	0.0285	H-10→L	12
			H-1→L+9	11
S26	142	0.0972	H-14→L	45
			H-12→L	8

a) only those transitions corresponding to the bands reported in Fig. 3.2.1.1 are included
b) H – HOMO and L – LUMO
c) only the first two major contributions are included

Thus, the calculated ϵ values for S1 and S2 transitions (29.6 and 19.9 $M^{-1}cm^{-1}$, respectively) is about three order of magnitudes lower than those corresponding to the higher energy transitions (23287 $M^{-1}cm^{-1}$ for the S26 state). The experimental ϵ value reported for S1 transition of CQ in ethanol [21] is 28 $M^{-1}cm^{-1}$ and the experimentally reported λ_{max} for CQ are: 470 nm in chloroform [6] and ethanol [21] and 472 nm in toluene [22].

Commonly, in order to describe a particular transition to an excited state one uses the molecular orbitals. However, for some transitions there can exist more contributions to that particular transitions, making very difficult the analysis of based on the frontier MOs. An alternative is to use the natural transition orbitals (NTOs) which are a transformed version of the canonical orbitals and can be calculated on the basis of the transition densities [23]. This formalism offers compact description of the electronic excitations with the advantage that only one or two occupied/virtual pairs of orbitals are enough for a clear interpretation of the physical nature of the excited states involved in absorption and emission processes. The advantage of using NTOs is that a particular transition can be described by using a single pair of such orbitals – one occupied and one unoccupied.

It is a common practice to denote the occupied NTOs as “hole transition orbitals” and the unoccupied NTOs as “particle transition orbitals” [24, 25]. Fig. 5 illustrates the NTOs for the main electronic transitions of CQ monomer in acetonitrile.

Quantum chemical calculations give a clear picture of the emergence of electronic transition to S1 state. Thus, as observed in Fig. 5, both, the hole and particle NTOs are delocalized onto the ketone groups of CQ. Moreover, the particular shapes of the two NTOs suggest a $n \rightarrow \pi^*$ transition, that is, an electronic transition described as promotion of an electron from a non-bonding (lone-pair) orbital localized on the oxygen atoms of CQ to the antibonding π^* orbital, also localized mainly on the two oxygen atoms.

3.2. Emission energy and fluorescence lifetime of Camphorquinone

The excitation energy and the identity of the molecular orbitals involved are only a part of the parameters used to describe the molecular excited states. Other important parameters of the excited states are the (vertical) emission energy and fluorescence lifetime. Both of them are very sensitive to the molecular conformation or to the environment of the chromophore. While the emission energy can be routinely measured, obtaining the experimental values of the fluorescence lifetime is much more challenging but it still can be done by using time-resolved fluorescence technique.

From computational point of view, the calculation of these parameters imply geometry optimization of the molecule in a particular excited state. Nowadays, such calculations can be done using high performance computers.

Figure 6 summarizes the points on the ground and excited potential energy surface that need to be calculated for obtaining the emission energy.

Particularly, for estimating the vertical emission energy we need the energy minimum on the potential surface of the excited state and the energy calculated on the geometry of the excited state. The difference between the two values gives the vertical emission energy.

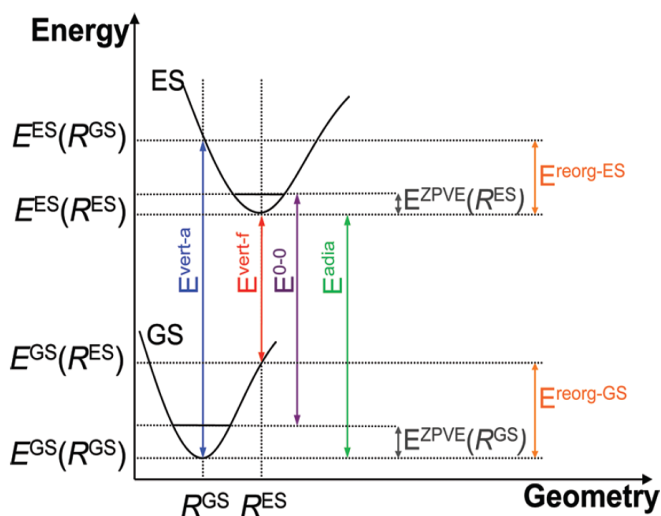


Fig. 6. Ground and excited states energies necessary to be computed for obtaining the emission energy of a molecules

Based on the model of vertical transitions, the radiative emission rate k_r can be obtained by [26]:

$$k_r = \frac{4}{3} \frac{\Delta E^3}{c^3} \mu_{10}^2$$

where c is the speed of light, ΔE is the energy of the $S_1 \rightarrow S_0$ transition and μ_{10} is the dipole strength. ΔE and μ_{10} must be evaluated at the energetic minimum corresponding to the excited state [27].

Having obtained k_r , the radiative fluorescence lifetime is calculated as $\tau_f = 1/k_r$.

Table 2 summarizes the calculate parameters necessary for the estimation of the vertical emission energy and the radiative fluorescence lifetime.

We have to mention that no experimental result was reported in the literature related to the fluorescence lifetime of CQ. Our estimation for the radiative part of the fluorescence lifetime is very large compared to other molecules and this is due to the very low value of the dipole strength and consequently, of the oscillator strength f . The experimentally estimated value for the radiative lifetime of CQ was obtained on the basis of the Strickler-Berg formula [28]:

$$\frac{1}{\tau_f} = 2.88 \cdot 10^9 n^2 \langle \tilde{\nu}_0^{-3} \rangle^{-1} \frac{g_{gs}}{g_{es}} \int \epsilon(\nu) d \ln(\nu)$$

where the integration is done over the entire absorption band of the fluorophore, n is the refractive index of the solvent, ν_0 is the wavenumber corresponding to the absorption maximum, ϵ is the molar absorptivity of the fluorophore, g_{gs} and g_{es} are the degeneracies of the ground and excited states, respectively.

The quantity can be calculated as:

$$\langle \tilde{\nu}_0^{-3} \rangle^{-1} = \frac{\int \nu^{-3} F(\nu) d\nu}{\int F(\nu) d\nu}$$

where $F(\nu)$ is the intensity of the fluorescence signal.

Table 2. PCM-B3LYP/6-311+G(2d,p) calculated parameters for the excited state of camphorquinone in acetonitrile

	Calculated	Experimental
μ_{10}^2 (a.u.)	0.0097	n.a.
f	0.0003	n.a.
λ_{abs} (nm)	446	469
λ_{em} (nm)	502	514
τ_r (ns)	6451	5133
Φ	n.a.	n.a.
τ_f (ns)	n.a.	n.a.
τ_{nr} (ns)	n.a.	n.a.
$\Delta\lambda_{Stokes}$ (nm)	56	45

3.3. Geometry of the ground and excited state

The experimental geometry of Camphorquinone has been retrieved from the The Cambridge Crystallographic Data Centre (CCDC) (Refcode: CAMPQU, CCDC number: 1120029) [29]. The molecule crystallizes in the I2 space group with the unit cell parameters: $a = 12.081 \text{ \AA}$, $b = 6.731 \text{ \AA}$, $c = 23.43 \text{ \AA}$, $\alpha = 90^\circ$, $\beta = 96.25^\circ$ and $\gamma = 90^\circ$.

Experimental and calculated geometrical parameters (bond lengths and valence angles) of CQ are summarized in Table 3. Besides the parameters of the ground state (S0) in gas-phase and acetonitrile we included also the parameters of the first excited state of CQ. As easily can be observed, the geometrical parameters of the ground state geometry are well reproduced by calculations. The largest discrepancies between the experimental and computed data are noted for the C3-C7 bond length and the C3C2O12 bond angle. Such discrepancies can be attributed to the fact that the calculations were performed on a single molecule and such a model cannot capture the intermolecular interactions inherent in solid phase.

Table 3. Experimental and B3LYP/6-311+G(2d,p) calculated geometrical parameters of Camphorquinone

Geometrical parameter	Experimental	Calculated B3LYP/6-311+G(2d,p)		
	X-ray	S0 (gas-phase)	S0 (acetonitrile)	S1 (acetonitrile)
C1-C2	1.554	1.571	1.569	1.492
C2-C3	1.511	1.516	1.506	1.549
C3-C4	1.535	1.554	1.557	1.552
C4-C5	1.535	1.556	1.554	1.557
C5-C6	1.549	1.562	1.566	1.559
C6-C7	1.558	1.577	1.580	1.558
C3-C7	1.533	1.561	1.564	1.544
C7-C8	1.522	1.537	1.536	1.534
C7-C9	1.537	1.532	1.532	1.546
C6-C10	1.510	1.515	1.516	1.513
C6-C1	1.496	1.527	1.517	1.581
C1-O11	1.204	1.200	1.205	1.223
C2-O12	1.179	1.200	1.205	1.227
C1C2C3	102.9	103.6	103.9	104.4
C2C3C4	103.5	104.5	104.3	104.6
C3C4C5	103.1	130.4	103.5	102.7
C4C5C6	105.3	104.6	104.7	103.9
C5C6C1	103.6	103.3	103.0	103.0

Geometrical parameter	Experimental	Calculated B3LYP/6-311+G(2d,p)		
	X-ray	S0 (gas-phase)	S0 (acetonitrile)	S1 (acetonitrile)
C5C6C7	101.8	102.1	102.0	102.9
C5C6C10	115.9	115.1	115.1	115.9
C6C1C2	105.4	104.5	104.8	104.5
C6C7C8	113.4	113.3	113.3	115.0
C6C7C9	113.0	114.0	113.9	113.0
C6C1O11	130.4	129.2	130.1	126.8
C3C2O12	131.0	126.3	130.8	127.7

* bond lengths in Å; angles in degrees

We were also interested in the change of CQ's geometry as a result of electronic excitation. For this purpose, the geometry of CQ was optimized in acetonitrile in ground (S0) and the first excited state (S1). Fig. 7 shows the two superimposed optimized geometries.

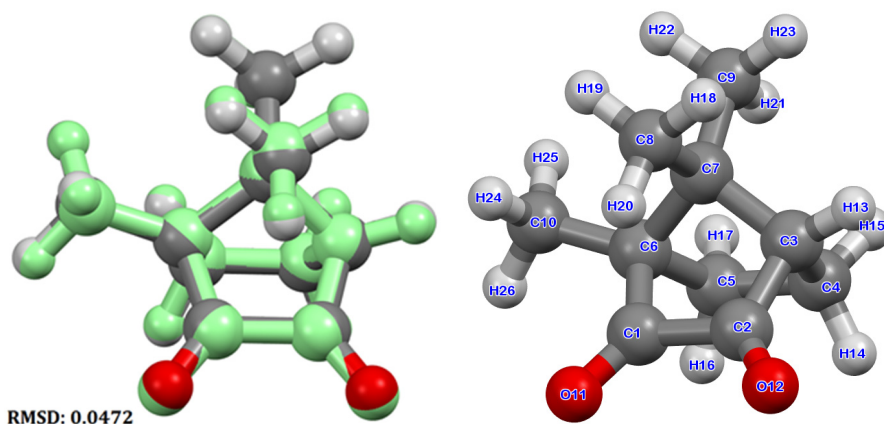


Fig. 7. left: Superimposed B3LYP/6-311+G(2d,p) of CQ in acetonitrile in ground state and excited state (light green); right: atom number scheme for CQ

According to theoretical results, the geometry of CQ is slightly distorted in the excited state, quantitatively, the average root mean square deviation (rmsd) between the backbone atoms being 0.0472 Å. The only geometrical parameters affected in an appreciable manner are the C1-C2 and C6-C1 bond lengths and the

bond angles involving the oxygen atoms (C6C1O11 and C3C2O12). Less deviations can be observed for the bonds involving the C7 atom (shortening of about 0.02 Å) and also, for the two C=O bonds which suffer a lengthening of cca. 0.02 Å. This distortion of the geometry in the S1 excited state is reflected in the relatively small Stokes shift observed for the calculated (and experimental) absorption and emission spectra of CQ (see Table 3.).

4. CONCLUSIONS

Absorption and emission spectra of the photoinitiator camphorquinone have been calculated at TD-DFT-B3LYP/6-31+G(2d,p) level of theory. The transition to the first excited state of Camphorquinone is an $n \rightarrow \pi^*$ transition and it was explained on the basis of the natural transition orbitals. The calculated electronic absorption energy ($\lambda_{\text{max}} = 484 \text{ nm}$) was in excellent agreement with the available experimental data.

The vertical emission energy (514 nm), as well as the radiative fluorescence lifetime (6.45 μs) has been computed for CQ. The most important structural parameters affected by the transition to the first excited state are those describing the two carbonyl groups.

ACKNOWLEDGMENTS

The research undertaken for this article was conducted using the Babeș-Bolyai University Research infrastructure financed by the Romanian Government through the project MADECIP (POSCEE COD SMIS CSNR 48801/1862)

REFERENCES

- [1] R.L. Bowen, *J. Am. Dental Assoc.*, 66 (1963) 57-64; R.L Bowen, W.A. Marjenhoff, *Adv. Dent. Res.*, 6 (1992) 44-49.
- [2] J.F. Glenn, Composition and properties of unfilled and composite restorative materials. In: D.C. Smith, D.F. Williams, editors. *Biocompatibility of dental materials*. Vol III. 10th ed. Boca Ration (FL): CRC Press; 1982. p. 98-125.
- [3] L.J. Schneider, L.A. Cavalcante, S.A. Prah, C.S. Pfeifer, J.L. Ferracane, *Dent. Mat.*, 28 (2012) 392-397.

- [4] J.G. Leprince, M. Hadis, A.C. Shortall, J.L. Ferracane, J. Devaux, G. Leloup et al., *Dent. Mat.*, 27 (2011) 157-164.
- [5] G. Longhi, E. Castiglioni, S. Abbate, F. Lebon, D.A. Lightner, *Chirality*, 25 (2013) 589-599.
- [6] Z. Okulus, T. Buchwald, M. Szybowicz, A. Voelkel, *Mat. Chem. Phys.* 145 (2014) 304-312.
- [7] M.R. Casida, C. Jamorski, K.C. Casida, D.R. Salahub, *J. Chem. Phys.* 108 (1988) 4439-4449.
- [8] Gaussian 09, Revision E.01, M.J. Frisch, G.W. Trucks, H.B. Schlegel, G.E. Scuseria, M.A. Robb, J.R. Cheeseman, G. Scalmani, V. Barone, B. Mennucci, G.A. Petersson, H. Nakatsuji, M. Caricato, X. Li, H.P. Hratchian, A.F. Izmaylov, J. Bloino, G. Zheng, J.L. Sonnenberg, M. Hada, M. Ehara, K. Toyota, R. Fukuda, J. Hasegawa, M. Ishida, T. Nakajima, Y. Honda, O. Kitao, H. Nakai, T. Vreven, J.A. Montgomery, Jr., J.E. Peralta, F. Ogliaro, M. Bearpark, J.J. Heyd, E. Brothers, K.N. Kudin, V.N. Staroverov, R. Kobayashi, J. Normand, K. Raghavachari, A. Rendell, J.C. Burant, S.S. Iyengar, J. Tomasi, M. Cossi, N. Rega, J.M. Millam, M. Klene, J.E. Knox, J.B. Cross, V. Bakken, C. Adamo, J. Jaramillo, R. Gomperts, R.E. Stratmann, O. Yazyev, A.J. Austin, R. Cammi, C. Pomelli, J.W. Ochterski, R.L. Martin, K. Morokuma, V.G. Zakrzewski, G.A. Voth, P. Salvador, J.J. Dannenberg, S. Dapprich, A.D. Daniels, Ö. Farkas, J.B. Foresman, J.V. Ortiz, J. Cioslowski, and D.J. Fox, Gaussian, Inc., Wallingford CT, 2009.
- [9] A.D. Becke, *J. Chem. Phys.* 1993, 98, 5648.
- [10] C. Lee, W. Yang, R.G. Parr, *Phys. Rev. B*, 37 (1988) 785.
- [11] S. H. Vosko, L. Wilk, M. Nusair, *Can. J. Phys.* 1980, 58, 1200.
- [12] P.J. Stephens, F.J. Devlin, C.F. Chabalowski, M.J. Frisch, *J. Phys. Chem.* 98 (1994) 11623-11627.
- [13] R.L. Martin, *J. Chem. Phys.* 118 (2003) 4775-4777.
- [14] S. Marković and J. Tošović, *J. Phys. Chem. A* 119 (2015) 9352-9362.
- [15] J. Tomasi, B. Mennucci and R. Cammi, *Chem. Rev.* 105 (2005) 2999-3093.
- [16] GaussView, Version 5, Roy Dennington, Todd Keith, and John Millam, Semichem Inc., Shawnee Mission, KS, 2009.
- [17] C.F. Macrae, P.R. Edgington, P. McCabe, E. Pidcock, G.P. Shields, *J. Appl. Crystallogr.* 39 (2006) 453-457.
- [18] T. Corrales, F. Catalina, C. Peinado, N.S. Allen, *J. Photochem. Photobiol. A: Chemistry*, 159 (2003) 103-114.
- [19] E. Andrzejewska, L.-A. Linden, J.F. Rabek, *Macromol. Chem. Phys.* 199 (1998) 441.
- [20] M.G. Neumann, W.G. Miranda Jr, C.C. Schmitt, F.A. Rüggeberg, I.C. Correa, *J. Dent.* 33 (2005) 525-532.
- [21] D.C.R.S. de Oliveira, M.G. Rocha, A. Gatti, A.B. Correr, J.L. Ferracane, M.A.C. Sinhoreti, *J. Dent.* 43 (2015) 1565-1572.
- [22] K. Ikemura, T. Endo, *Dent. Mat. J.* 29 (2010) 481-501.
- [23] M.A.L. Marques, E. K.U. Gross, in: *Time dependent density functional theory*, eds. C. Fiolhais, F. Nogueira, M. Marques, p. 144-184, Springer-Verlag, Berlin 2003.
- [24] J.B. Foresman and Æ. Frisch, *Exploring Chemistry with Electronic Structure Methods* (third edition), Gaussian Inc., 2015, Wallingford, CT USA.

- [25] X. Zheng, Q. Peng, J. Lin, Y. Wang, J. Zhou, Y. Jiao, Y. Bai, Y. Huang, F. Li, X. Liu, X. Pua and Z. Lu, *J. Mater. Chem. C* 3 (2015) 6970-6978.
- [26] [Lou02] B. Lounis, M. Onil, *Rep Prog. Phys.*, 68, (2005) 1129-1179.
- [27] M. Savarese, A. Aliberti, D. De Santo, E. Battista, F. Causa, P. A. Netti and N. Rega, *J. Phys. Chem. A*, 116 (2012) 7491-7497.
- [28] S. J. Strickler, R. A. Berg, *J. Chem. Phys.*, 37 (1962) 814-822.
- [29] Cambridge Crystallographic Data Centre (CCDC) (Refcode: CAMPQU, CCDC number: 1120029). (accessed: 05.02.2017)

Dedicated to Professor Dr. Sorin Dan Anghel on His 65th Anniversary

NONUNIFORM NUMERICAL GRID FOR THE NUMERICAL SOLUTION OF THE SCHRÖDINGER EQUATION

S. BORBÉLY*

ABSTRACT. In the present work the numerical grids used during the numerical solution of the Schrödinger equation will be investigated. It will be shown, that by employing a nonuniform optimized numerical grid the number of gridpoints and implicitly the computational effort for the solution of the Schrödinger equation can be significantly reduced. As a test system the harmonic oscillator, and the finite-elements discrete variable representation (FEDVR) numerical will be used, but the obtained results can be extended to other systems and numerical grids too.

Keywords: *ab initio solution of Schrödinger equation, numerical grid optimization, harmonic oscillator*

INTRODUCTION

The processes induced in atomic systems by ultrashort high intensity laser pulses are highly nonlinear [1,2]. The theoretical investigation of these processes (ex. multiphoton ionization, tunneling and over the barrier ionization, high harmonics generation) is a complicated task due to the non-linearity. Since the theoretical models developed for the description of the interaction between traditional light sources (thermal sources, discharge lamps, low intensity lasers, synchrotron radiation) are suitable only for the description of linear processes (i.e. single photon ionization), the development of a new generation of theoretical models became necessary. In the last few decades a large number of theoretical models were developed for the

* Babeş-Bolyai University, Faculty of Physics, Kogălniceanu Street 1, 400084 Cluj-Napoca, Romania;
e-mail: sandor.borbely@phys.ubbcluj.ro

theoretical description [1,2] of the above mentioned nonlinear processes, which can be divided into two groups. The first group is formed by the models which are based on the approximate solution of the time-dependent Schrödinger equation. The advantage of these models is that they can be relatively easily computed, and they provide qualitatively good results. However, they have disadvantages too: In most of the cases they do not provide quantitative agreement to the experimental data, and they can not describe all the nonlinear processes simultaneously. The second group is formed by the models, which are based on the *ab initio* numerical solution of the Schrödinger equation. These models provide results with excellent agreement with the experimental data, however, they imply a large computational effort. The Schrödinger equation for systems with a single active particle (electron) can be solved numerically on a simple workstation, however for larger systems with 2 or more active particles high performance computing clusters are required.

The models based on the *ab initio* solution of the Schrödinger equation have two major components: the first is the numerical grid (or numerical basis) on which the wave function is represented, while the second is the method which is used for the time-propagation of the wave function. The optimal implementation of these two components can significantly reduce the computational effort needed for the solution of the Schrödinger equation.

For the time-propagation there is a large set of advanced and highly optimized methods (Crank-Nicolson [3], short-iterative Lánczos [4], Adams-Bashforth-Moulton [5], etc.) available, which can be implemented with adaptive time-steps. In the case of these time propagators there is little room for further optimization. In contrast to this, the currently used numerical grids for the representation of the wave function can be further optimized. Compared to the simplest approach (finite difference representation – i.e. equidistant numerical grid) the more elaborate approaches (b-spline basis [8], finite-element discrete representation – FEDVR [6,7]) perform much better, achieving a significant performance increase of the numerical program. In the atomic physics community the use of FEDVR [6,7] or b-spline [8] discretization is a well spread practice during the numerical solution of the time-dependent Schrödinger equation. In most of these cases the finite elements (FEDVR) or the basis nodes (b-spline) are uniformly distributed. In some cases a denser grid is used in the vicinity of the nucleus, with a monotonously decreasing density as we depart from the center.

Here, in the framework of the FEDVR representation an approach for the further optimization of the numerical grid will be presented. As the result of this optimization, the number of gridpoints (FEDVR basis) which are required for the high precision representation of the ground state wave function of the chosen system (one-dimensional harmonic oscillator) is significantly reduced.

The present work is structured as follows: After this short introduction, in the Theory section, the discretization of the Schrödinger in the FEDVR basis is presented. This is followed by the introduction of the negative imaginary time propagation method, which will be used for the calculation of the ground state of our system. At the end of the section the optimization algorithm is presented. In the next section the numerical convergence test for the homogeneous FEDVR grids and the results of the numerical grid optimization are presented, while in the last section conclusions are drawn. Throughout the paper atomic units are used.

THEORY AND METHODS

In order to test the grid optimization algorithm one of the simplest physical systems, the one dimensional harmonics oscillator was chosen. The Hamiltonian of this system has the following form:

$$\hat{H} = -\frac{\partial^2}{2\partial x^2} + \frac{x^2}{2}, \quad (1)$$

where the mass and the elastic constant of the oscillator is set to 1. The harmonic oscillator was chosen, since the analytical form of it's eigenstates is known, which later on can be used as reference in order to asses the precision of the numerical solution. The stationary Schrödinger equation for our harmonic oscillator has the following form:

$$\hat{H}\psi(x) = E\psi(x), \quad (2)$$

where $\psi(x)$ is the wave function, while E is the energy of the oscillator. The analytical solution of the eigenequation (2) are known. From these solutions the wave function describing the ground state of our oscillator is given:

$$\psi_g(x) = \pi^{-1/4} e^{-x^2/2}. \quad (3)$$

The first step during the numerical solution of Eq. (2) is the discretization of the wave function, i.e. how the continuous wave function is represented by a finite set of real numbers, which can be stored in a computer. Here one of the most advanced discretization approach, the finite element discrete variable representation (FEDVR) is used. In the framework of this approach [6,7,9] the configuration space is divided into finite elements (i.e. into segments with variable length), and inside each segment the wave function is represented in local polynomial basis. The polynomial

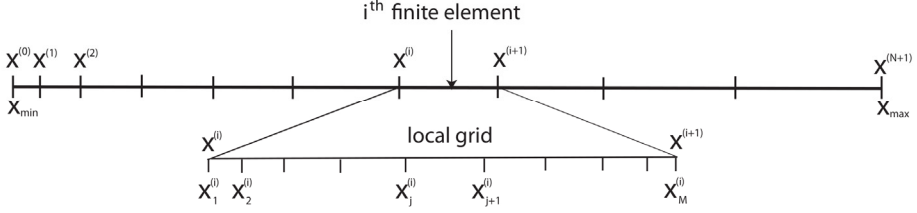


Fig. 1. The illustration of the FEDVR grid

basis functions are built on top of a set of local gridpoints (see Fig. 1), which are chosen to be Gauss integration nodes. For each finite element the Lagrange interpolation polynomials can be written as

$$L_m^{(i)}(x) = \begin{cases} \prod_{j \neq m} \frac{x - x_j^{(i)}}{x_m^{(i)} - x_j^{(i)}} & \text{if } x \in [x_1^{(i)}, x_M^{(i)}] \\ 0 & \text{elsewhere} \end{cases} \quad (4)$$

where $x_j^{(i)}$ are the local gridpoints of the i -th finite element, and M is the number of gridpoints (i.e. the number of basis functions) inside the finite element. Using these polynomials the FEDVR basis can be defined as

$$f_m^{(i)}(x) = \begin{cases} \frac{L_1^{(i)}(x) + L_M^{(i-1)}(x)}{w_1^{(i)} + w_M^{(i-1)}} & \text{if } m = 1 \\ \frac{L_m^{(i)}(x)}{w_m^{(i)}} & \text{if } m = 2, \dots, M-1 \\ \frac{L_M^{(i)}(x) + L_1^{(i+1)}(x)}{w_M^{(i)} + w_1^{(i+1)}} & \text{if } m = M \end{cases}, \quad (5)$$

where $w_m^{(i)}$ are the integration weights corresponding to the $x_m^{(i)}$ quadrature points. With the help of this orthonormal basis set the wave function can be expressed as

$$\psi(x) = \sum_{i,j} w_j^{(i)} c_j^{(i)} f_j^{(i)}(x), \quad (6)$$

there the $c_j^{(i)}$ expansion coefficients are simply the value of the wave function in the corresponding gridpoints: $c_j^{(i)} \equiv \psi(x_j^{(i)})$. Based on Eq. (6) it can be shown that, as the result of the discretization, the Schrödinger equation (2) is transformed into a matrix eigenequation:

$$H\Psi = E\Psi \quad (7)$$

where Ψ is the wave function vector (which contains as elements the value of the wave function in the FEDVR gridpoints), and H is the Hamiltonian matrix. This way the solution of the Schrödinger equation is reduced to the solution of a matrix eigenequation, which is standard task in computational sciences. If all the eigenvectors and eigenvalues are sought, then one of the standard linear solvers (lapack [10], SLEPc [11]) can be used, which is a computationally expensive task for a large Hamiltonian matrix. In contrast to this, when only the ground state of a Hamiltonian is searched, an alternative approach, the negative imaginary time propagation (NITP) should be used, which is much less expensive.

In the framework of the NITP approach an arbitrary initial guess of the wave function (ex. a constant function) is propagated in negative imaginary time according to the time dependent Schrödinger equation:

$$-\frac{\partial}{\partial t} \psi(t') = \hat{H}\psi(t'). \quad (8)$$

During this propagation the initial guess will converge towards the ground state wave function of the Hamiltonian. Since the NITP is non-unitary the wave function should be normalized to 1 at each time propagation step.

The precision of the numerically obtained ground state wave function depends on the parameters of the underlying numerical grid on which it is solved. In the case of FEDVR grids, the solution depends on the finite element boundaries, and on the number of basis functions inside the finite elements

$$\psi_g^{num}(x) \equiv \psi_g^{num}(x; x_1^{(1)}, \dots, x_M^{(n)}, M). \quad (9)$$

Before the optimization of the solution, an optimization parameter should be defined, which can measure the precision of the numerical solution. Based on the exact analytical solution [see Eq. (3)] this measure can be defined as

$$\varepsilon(x_1^{(1)}, \dots, x_M^{(n)}, M) \equiv \sum_{i,j} w_j^{(i)} \left| \psi_g(x_j^{(i)}) - \psi_g^{num}(x_j^{(i)}) \right|^2, \quad (10)$$

which measures the deviation of the numerical wave function from the analytical one. The goal of the present paper is to find the optimal values for the finite element boundaries, for which ε is minimal.

The optimization algorithm in the present paper is started from a uniform FEDVR grid, where the size of each finite element is the same ($x_m^{(i)} - x_1^{(i)} = \Delta x$). In an optimization loop the position of the finite element boundaries are modified by $\pm \delta x$ one after the other. If as a result of a finite element boundary modification ε decreases, then the modification is accepted, otherwise it is rejected. The optimization loop is repeated until none of the finite element boundary modifications are accepted. Then, the modification step-size is refined ($\delta x \rightarrow \delta x / 2$), and the optimization is continued. In the present paper this refinement is applied 5 times after which the optimization is stopped.

RESULTS AND DISCUSSIONS

Since the Hamiltonian of the harmonic oscillator (1) is symmetric with respect to $x = 0$, the uniform FEDVR grid was chosen to be symmetric too: $x_{min} \equiv x_1^{(1)} = -x_M^{(n)} \equiv x_{max}$, thus the size of the simulation box is $x_{box} = 2x_{max}$, while the size of each finite element is $\Delta x = x_{box} / n$. For the sake of simplicity, throughout the calculations the number of basis functions inside the finite elements was fixed to $M = 9$.

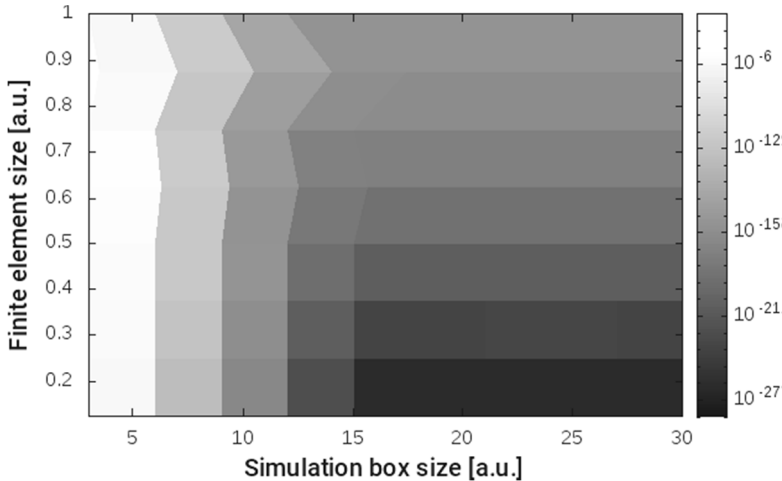


Fig. 2. The precision of the numerical solution (ε) as a function of the simulation box size and of the size of the finite element.

Before the application of the optimization algorithm the numerical convergence tests should be performed for the uniform FEDVR grid. The precision of the numerical wave function is shown as the function of the simulation box size (x_{box}) and of the finite element size (Δx) on Fig. 2, where it can be observed the large basin of the parameter space, where the numerical solution is converged. For the better understanding of the convergence properties cuts of the convergence map were prepared. On Fig. 3 the convergence parameter is shown as a function of the finite element size for fixed simulation box size $x_{box} = 30$ a.u. It can be observed that by increasing the density of the numerical grid, the precision of the numerical solution can be increased by orders of magnitude. For the finite element size of 0.125 a.u. the convergence parameter reached the 10^{-26} limit and it's further significant decrease is limited by the double precision floating point representation of real numbers in the computer program. Next, the convergence parameter is shown as a function of the simulation box size for fixed finite element size ($\Delta x = 0.125$). It can be observed the numerical wave function is converging fast as the size of the simulation is increased. For the simulation box sizes larger than 15 a.u. the precision of the numerical wave function can not be increased further, since it is limited by the precision imposed by the numerical grid density.

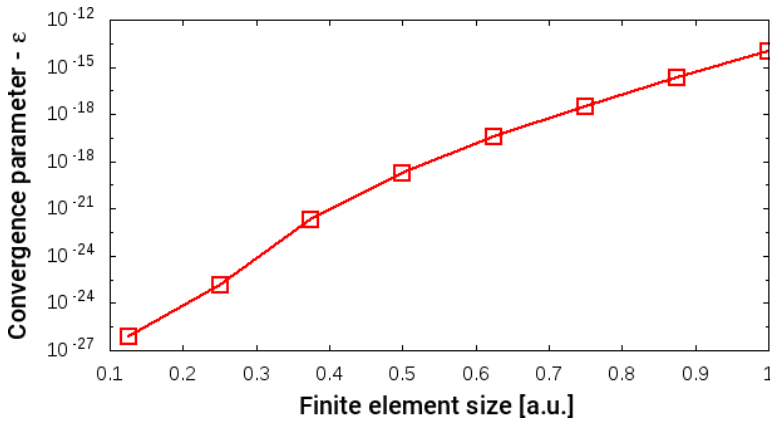


Fig. 3. The precision of the numerical solution as a function of Δx for fixed $x_{box} = 30$ a.u.

Based on the above conclusions the optimization algorithm is applied for a simulation box size fixed at $x_{box} = 16$ a.u. During the optimization the symmetry of

the Hamiltonian is exploited, which reduced significantly the parameter space (the number of free parameters is reduced by half). The initial value of the finite element boundary modification size was set at $\delta x = 0.02$ a.u., which was refined 5 times.

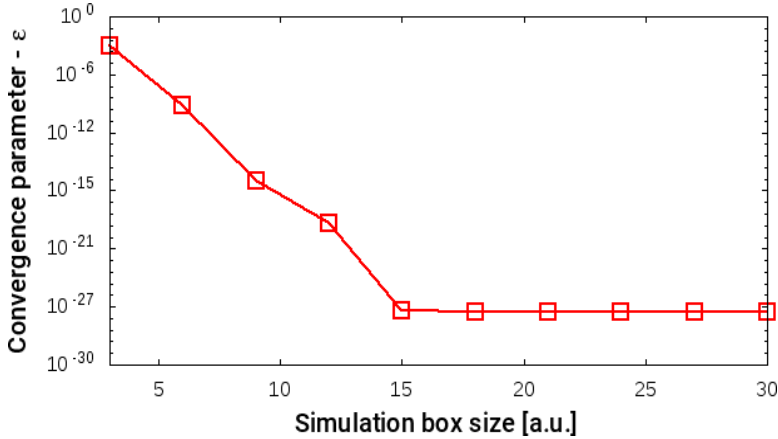


Fig. 4. The precision of the numerical solution as a function of x_{box} for fixed $\Delta x = 0.125$.

The results of the optimization are summarized in Table 1, where for different grid densities (i.e. for different gridpoint numbers N_{gp}) the precision of the numerically obtained wave functions are shown for homogeneous (ε_{hom}) and for optimized grids (ε_{opt}). From these results one can observe, that by performing the grid optimization the precision of the obtained numerical wave function can be significantly (by 4 or 5 orders of magnitudes) increased. Or, alternatively, a target wave function precision can be achieved with less gridpoints (i.e. with less computational resources) on an optimized grid. For example the $\varepsilon = 10^{-19}$ target precision can be achieved with 275 points on a homogenous grid, while the same precision can be reached with only 129 points on an optimized grid. At first sight this reduction of gridpoint number by a factor of 2 does not seem significant. However, the computational resource demand of the numerical solution of the Schrödinger equation scales polynomially as a function of the total gridpoint number, which means that in a 3D problem the reduction of the 1D gridpoint number leads to a significant (orders of magnitude) reduction of the computation time.

Table 1. The precision of the numerical solution before and after optimization for different grid densities. The size of the simulation box is fixed at 16 a.u.

Δx	N_{gp}	ε_{hom}	ε_{opt}	$\varepsilon_{hom} / \varepsilon_{opt}$
2	65	7.24E-011	2.11E-013	343.12
1	129	3.74E-014	3.96E-019	94358.10
0.5	257	2.85E-019	2.35E-023	12131.81
0.25	513	6.44E-024	2.71E-024	2.37

The presented results also show that the optimization does not always leads to significant improvement of the results. When the results are already converged on a homogeneous grid the optimization of the grid does not lead to significant improvements (see the data in the last row of Table 1). In the other extreme case, when the homogeneous grid is sparse, the results of the grid optimization is also less spectacular (see the data in the first row of Table 1).

CONCLUSIONS AND OUTLOOK

In the present work the numerical grids used during the solution of the Schrödinger equation were investigated using as benchmark system the one dimensional harmonic oscillator. For the numerical representation of the wave function, the finite elements discrete variable representation (FEDVR) approach was used, which is one of the most advanced numerical discretization approach currently used by the atomic physics community. In the first step the convergence of the numerical results as a function of grid parameters was investigated in details for homogeneous FEDVR grids. Then, a grid optimization method was implemented, which was used to obtain the ground state of the harmonic oscillator with the same precision as in the case of homogeneous grids, but with much less gridpoints. It was also observed that grid optimization is not efficient if on the original grid the solution is close to the converged one, or the initial grid is too sparse.

It should be mentioned that optimization algorithm used here does not guarantees that the global minimum of $\varepsilon(x_1^{(1)}, \dots, x_M^{(n)}, M)$ is found, it is very likely that it finds only a local minimum. However, even if this happens, the obtained improvement (the reduction of the gridpoint number by a factor of 2) is important, since it can significantly reduce the computational resources needed for the numerical solution of the Schrödinger equation. The optimization method used here can be easily extended to other type of numerical grids (ex. B-spline), and to time-dependent problems.

REFERENCES

1. F. Grossmann, *Theoretical Femtosecond Physics*, second edition, Springer, Heidelberg, 2013.
2. C.J. Joachain, N.J. Kylstra, R.M. Potvliege, *Atoms in Intense Laser Fields*, Cambridge University Press, Cambridge, 2012.
3. J. Crank, P. Nicolson, *Advances in Computational Mathematics*, **6**, 207 (1996).
4. T.J. Park and J.C. Light, *The Journal of Chemical Physics*, **85**, 5870 (1986).
5. E. Hairer, S.P. Norsett, G. Wanner, *Solving ordinary differential equations I: Nonstiff problems*, Springer Verlag, Berlin 1993.
6. B. I. Schneider and L. A. Collins, *Journal of Non-Crystalline Solids*, **351**, 1551 (2005).
7. T. N. Rescigno and C. W. McCurdy, *Phys. Rev. A*, **62**, 032706 (2000).
8. M. G. Cox, *Journal of the Institute of Mathematics and its Applications*, **15**, 95 (1975).
9. A. Tóth, *Ionization of Atoms by Intense Laser Pulses*, Egyetemi Műhely Publisher, Cluj-Napoca, 2014.
10. E. Anderson *et al.*, *LAPACK Users' Guide*, third edition, pub. Society for Industrial and Applied Mathematics, Philadelphia, PA, 1999.
11. V. Hernandez, J. E. Roman, V. Vidal, *ACM Trans. Math. Software*, **31(3)**, 351 (2005).

Dedicated to Professor Dr. Sorin Dan Anghel on His 65th Anniversary

MAGNETOCALORIC AND MAGNETIC PROPERTIES OF NANOCRYSTALLINE $\text{La}_{0.75}\text{Pb}_{0.25}\text{MnO}_3$ SYNTHESIZED BY HIGH ENERGY BALL MILLING

R. DUDRIC^{a*}, G. SOUCA^a, I.G. DEAC^a and R. TETEAN^a

ABSTRACT. Nanocrystalline $\text{La}_{0.75}\text{Pb}_{0.25}\text{MnO}_3$ powders were synthesized by grinding the constituent oxides in air at room temperature, using a high-energy planetary mill. The reaction process, evaluated by analyzing the evolution of the crystalline structure in the XRD patterns, is completed after about 12 h. The magnetic measurements indicate that the manganite nanoparticles with sizes smaller than 15 nm obtained by reacting milling have significant defects at the surface, leading to a serious decrease of the magnetic moments in comparison to the bulk material. A significant magnetocaloric effect was found at temperatures ranging from below to above room temperature, with the maximum entropy change located at temperatures near the magnetic transition one. The high RCP(S) values together with the broadened magnetic entropy curve suggest the possibility to use these materials for magnetic refrigeration devices.

Keywords: nanoparticles; LPMO; high energy ball milling; magnetocaloric effect;

INTRODUCTION

The doped manganese perovskites, with general composition $\text{R}_{1-x}\text{A}_x\text{MnO}_3$, where R is a La or a rare-earth ion and A is an alkaline-earth ion, have been intensively investigated in the last years due to their interesting and intriguing physical properties such as colossal magnetoresistance (CMR), phase separation (PS), charge ordering (CO), orbital ordering (OO) and spin glass (SG) behavior and for their potential technical

^a Faculty of Physics, Kogalniceanu 1, 400084 Cluj-Napoca, Babes-Bolyai University, Romania

* Corresponding author e-mail: roxana.pacurariu@phys.ubbcluj.ro

applications [1–8]. Their rich electronic phase diagrams reflect the fine balance of interactions, which determine the electronic ground state. Many of the lanthanum manganite compounds, $\text{La}_{1-x}\text{A}_x\text{MnO}_3$, where $\text{A}=\text{Ca}$, Sr or Ba , were found to exhibit large or unusual magneto-caloric effect (MCE) values under moderate external magnetic field [9]. On the other hand, these materials display considerably small magnetic hysteresis and their Curie temperature can be tuned easily. $\text{La}_{1-x}\text{Pb}_x\text{MnO}_3$ (LPMO) manganites are also promising for applications, considering the ferromagnetic metallic (FMM) phase at room temperature along with large magnetoresistance and good MCE at temperatures ranging from below to above room temperature [10-13]. However, the investigation of polycrystalline LPMO manganites has been restricted due to evaporation of Pb at temperatures higher than 900°C which are required for the conventional powder solid-state reaction synthesis. Using a PbO atmosphere in the furnace is one approach to overcome PbO loss which obviously cannot impart perfect homogeneity and uniform microstructure to the final products [14]. Another approach to maintain better homogeneity and stoichiometry is lowering reaction temperature below the melting point of PbO by using sol-gel route [15], but the chemical solution methods they are generally complicated and the agents used can be very expensive. A satisfactory method for obtaining fine and homogeneous manganites powder may be mechanochemical synthesis, which is a powerful method for the production of novel, high performance and low cost materials such as ferrites or intermetallics. The mechanochemical synthesis can deliver the designed phases and structures by a single step of the high-energy ball milling conducted in an enclosed activation chamber at room temperature. In recent years, high-energy ball milling was used to the mechanosynthesis of stoichiometric $\text{La}_{0.8}\text{Pb}_{0.2}\text{MnO}_3$ manganites by grinding constituent oxides at room temperature [16].

In this paper we report the single step synthesis of nanocrystalline $\text{La}_{0.75}\text{Pb}_{0.25}\text{MnO}_3$ manganite powders via high-energy milling of oxide precursors and the investigation of the magnetic and magnetocaloric properties.

EXPERIMENTAL

$\text{La}_{0.75}\text{Pb}_{0.25}\text{MnO}_3$ nanoparticles were synthesized from 99.99% purity oxides of La_2O_3 , PbO , MnO and MnO_2 . The oxides were mixed in stoichiometric proportions and mechanically milled in air using a high-energy planetary mill (Fritsch Pulverisette 4) with 440C hardened steel balls and milling vial. The milling speed of the vial was 900 rpm and the ball-to-powder ratio of 10:1. The powder milling process was interrupted several times and small amounts of powder were

taken out of the vial. In order to prevent the excessive overheating of the containers, the experiments were carried out by alternating 120 min of milling with 30 min of rest. For magnetic measurements the powders were pressed into pellets of 10 mm diameter under a pressure of 1 tonne/cm², heated in air to 600°C for 12 h and slowly cooled to room temperature.

The crystallographic properties of the samples were investigated by X-ray diffraction (XRD) at room temperature by using a Bruker D8 Advance AXS diffractometer with Cu K α radiation in the 2 θ region 20°-65°. The crystallite-sizes were calculated using the Debye-Scherrer formula:

$$D = \frac{k\lambda}{\beta \cos\theta} \quad (1)$$

where β is the peak full width at half maximum (in radians) at the observed peak angle ϑ , k is the crystallite shape factor (was considered 0.94) and λ is the X-ray wavelength (0.154 nm).

Magnetic measurements were carried out using a 12 T VSM from Cryogenics in the temperature range 4.2 – 350 K and external magnetic field up to 4 T. Both zero-field-cooled (ZFC) and field-cooled (FC) measurements were performed.

The magnetic entropy changes were determined from magnetization isotherms, between zero field and a maximum field (H_0) using the thermodynamic relation:

$$\Delta S_m(T, H_0) = S_m(T, H_0) - S_m(T, 0) = \frac{1}{\Delta T} \int_0^{H_0} [M(T + \Delta T, H) - M(T, H)] dT \quad (2)$$

where ΔT is the temperature increment between measured magnetization isotherms ($\Delta T = 5\text{K}$). The magnetic cooling efficiency was evaluated by calculating the relative cooling power (RCP) based on the magnetic entropy change:

$$\text{RCP}(S) = -\Delta S_m(T, H_0) \times \delta T_{\text{FWHM}} \quad (3)$$

where ΔS_m represents the maximum magnetic entropy change and δT_{FWHM} its full-width at half-maximum.

RESULTS AND DISCUSSION

Fig 1 shows the XRD patterns at room temperature of the powders milled for different periods of time ($t_{\text{mill}} = 2 \text{ h}, 5 \text{ h}, 7 \text{ h}, 9 \text{ h}, 11 \text{ h}, 12 \text{ h}$).

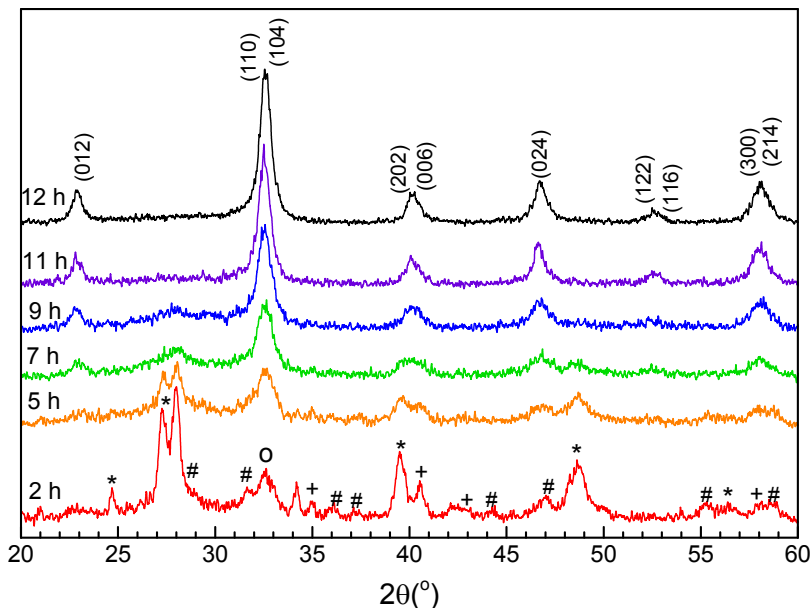


Fig. 1. XRD patterns of the mixture milled for different periods of time:
 (*) La_2O_3 , (+) MnO/MnO_2 , (#) PbO , (o) $\text{La}_{0.75}\text{Pb}_{0.25}\text{MnO}_3$

For milling time higher than 5 h the perovskite phase is preponderant and single phase $\text{La}_{0.75}\text{Pb}_{0.25}\text{MnO}_3$ powders were obtained after 12 h milling time. The profiles of the diffraction peaks in Fig 1 are broadened, suggesting that the synthesized powders are crystallites of nanoscale size. For milling time of 11 h and 12 h, for which the percentage of the LPMO phase is higher than 95 %, the lattice parameters, c/a ratios and crystallite-sizes (calculated using the Debye-Scherrer formula) were obtained from the XRD patterns and collected in Table 1. The values obtained from Rietveld refinement for the a lattice parameter and c/a ratio are clearly smaller than the values obtained previously for $\text{La}_{0.762}\text{Pb}_{0.238}\text{Mn}_{0.98}\text{O}_{3.04}$ synthesized by standard ceramic reaction ($c = 13.351 \text{ \AA}$, $c/a = 2.418$) [13], suggesting that for nanocrystalline LPMO powders the lattice contracts preferably in the a -direction rather than in the c -direction.

Table 1. Lattice parameters, c/a ratio and crystallite sizes estimated from XRD patterns

Milling time	a (Å)	c (Å)	c/a	χ^2	Crystallite size (nm)
11 h	5.51(2)	13.40(0)	2.43(1)	1.30	11
12 h	5.51(6)	13.40(7)	2.43(0)	1.18	14

The magnetization of the powder milled for 12 h and pressed into pellet, in zero field cooling (ZFC) and field cooling (FC) modes was measured. With decreasing temperature the magnetization shows an increase in the temperature range of 50 – 300 K, as shown in Fig 2a. The magnetic order temperature, defined as the temperature corresponding to the minimum of $\delta M/\delta T$ is about 255 K, smaller than for bulk LPMO, as it can be seen in the inset of Fig 2a. It has been shown that while synthesizing perovskite nanoparticles, the reactive milling technique creates significant defects not only at particles surface but also inside them that result the diminution of the exchange interaction strength. Fig 2b shows the $M(B)$ curves at 5 K in magnetic fields up to 4 T. The saturation magnetization of our nanocrystalline

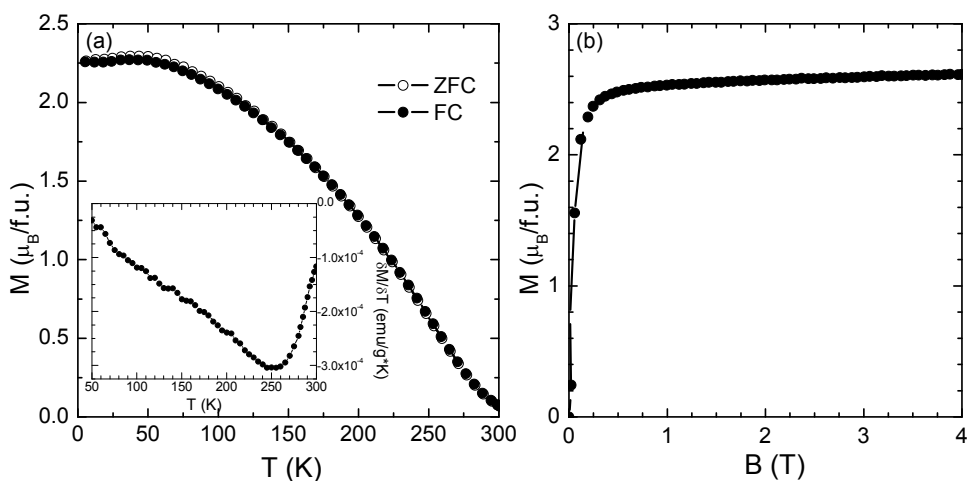


Fig 2. a) Temperature dependence of ZFC and FC magnetizations in 0.2 T;
b) Magnetic field dependence of the magnetization at 5 K

sample, of about 2.6 $\mu_B/f.u.$ at 5 K, is smaller than the bulk value of 3.2 $\mu_B/f.u.$, which may be an effect of the small particles size. A model for the nanoparticles in which the inner part has the same properties as the bulk compound (oxygen

stoichiometry, magnetic and transport properties), but the outer layer containing most of defects in the crystallographic structure shows a magnetically disordered state, is conceded widely to explain the size dependence of magnetization [17,18]. For nanoparticles of sizes lower than 15 nm the surface contribution is large and therefore leads to the diminution of the total magnetization.

The temperature dependence of the magnetic entropy change for $\text{La}_{0.75}\text{Pb}_{0.25}\text{MnO}_3$ in magnetic field of 4 T, determined from magnetization data, is plotted in Fig 3. The maximum value of $|\Delta S_m|$ is about 1.15 J/kgK, slightly smaller than the reported value of 1.3 J/kgK for bulk $\text{La}_{0.8}\text{Pb}_{0.2}\text{MnO}_3$ [10], which is expected considering the decreased value of the magnetization. The maximum value of the magnetic entropy change is located at about 250 K, close to the magnetic transition temperature and the peak is nearly symmetric around the maximum value. In order to evaluate the magnetic cooling efficiency, the RCP(S) values were calculated by using equation (3). The obtained value of about 200 J/kg is higher than for bulk LPMO (50-60 J/kg), due to the fact that the magnetic entropy change has a significant value over a broader temperature range. The RCP(S) value for our sample is comparable with those obtained in other oxide compounds, recommending nanocrystalline LPMO as good magnetic refrigerant materials operating at temperatures around room temperature.

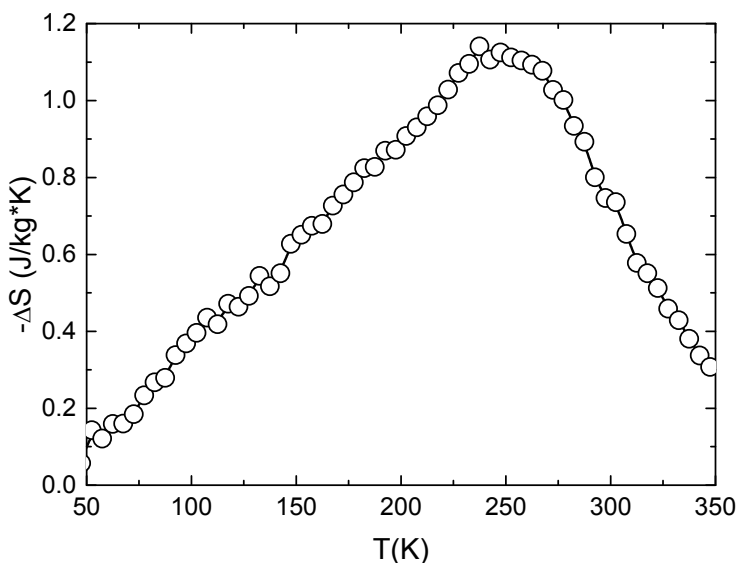


Fig. 3. Magnetic entropy changes for $\text{La}_{0.75}\text{Pb}_{0.25}\text{MnO}_3$ in $\Delta B = 4$ T

CONCLUSIONS

We have shown that nanocrystalline $\text{La}_{0.75}\text{Pb}_{0.25}\text{MnO}_3$ manganite powders can be synthesized at room temperature by high-energy milling of oxide precursors in a single step process. The reaction increases rapidly with the milling time and is completed after 12 h. The obtained powder consists of nanocrystals with sizes smaller than 15 nm. The magnetic measurements indicate that the perovskite nanoparticles obtained by reacting milling have significant defects at the surface, leading to a serious decrease of the magnetic moments in comparison to the bulk material. Our sample shows a significant magnetocaloric effect at temperatures ranging from below to above room temperature. Considering the high RCP(S) value, nanocrystalline $\text{La}_{0.75}\text{Pb}_{0.25}\text{MnO}_3$ can be considered as good magnetic refrigerant material. The results recommend high-energy milling as an effective method to prepare nanosized LPMO manganites.

ACKNOWLEDGEMENTS

This work was supported by the Romanian Ministry of Education and Research - UEFISCDI Project No. PN-II-ID-PCE-2011-3-0583 (85/2011).

REFERENCES

- [1] M. Uehara, S. Mori, C.H. Chen and S.W. Cheong, *Nature* 399 (1999) 560.
- [2] G.L. Liu, J.S. Zhou and J.B. Goodenough, *Phys. Rev. B* 64 (2001) 144414.
- [3] M. Iamada, A. Fujimori, Y. Tokura, *Rev. Mod. Phys.* 70 (1998) 1039.
- [4] O. Chmaissem, B. Dabrowski, S. Kolesnik, J. Mais, J.D. Jorgensen and S. Short, *Phys. Rev. B* 67 (2003) 094431.
- [5] B. Raveau, A. Maignan, C. Martin and M. Hervieu, *Chem. Mater.* 10 (1998) 2641.
- [6] C. Martin, A. Maignan, M. Hervieu and B. Raveau, *Phys. Rev. B* 60 (1999) 12191.
- [7] Y. Tokura and N. Nagaosa, *Science* 288 (2000) 462.
- [8] M. Pissas and G. Kallias, *Phys. Rev. B* 68 (2003) 134414.
- [9] M.-H. Phan, S.-C. Yu, *J. Magn. Magn. Mater.* 308 (2007) 325.
- [10] Nguyen Chau, Hoang Nam Nhat, Nguyen Hoang Luong, Dang Le Minh, Nguyen Duc Tho, Nguyen Ngoc Chau, *Phys. B: Condens. Matter*, 327 (2003), 270.
- [11] A. Rinkevich, A. Nossou, V. Vassiliev, E. Vladimirova, *J. Magn. Magn. Mater.* 285 (2005) 118.

- [12] T. Zhang, G. Li, T. Qian, J.F. Qu, X.Q. Xiang, X.G. Li, *J. Appl. Phys.* 100 (2006) 094324.
- [13] E. Burzo, I. Balasz, M. Isobe, Y. Ueda, *J. Alloys Compd.* 535 (2012) 129.
- [14] R.K. Dwivedi, M. Raghavendra raja, D. Bahadur, *J. Mater. Sci.* 40 (2005) 4801.
- [15] K. Mukherjee, A. Banerjee, *J. Phys.: Condens. Matter* 21 (2009) 106001.
- [16] H. Bahrami, P.Kameli, H.Salamati, *J. Magn. Magn. Mater.* 321(2009) 2533.
- [17] M.A. Lopez-Quintela, L.E. Hueso, J. Rivas, F. Rivadulla, *Nanotechnology* 14 (2003) 212–219.
- [18] P. Dey, T.K. Nath, *Phys. Rev. B* 73 (2006) 214425.

Dedicated to Professor Dr. Sorin Dan Anghel on His 65th Anniversary

FORMATION OF AMMONIA IN A LINEAR PLASMA REACTOR

E. FILEP^a, L. KENÉZ^{a*}, N. KUTASI^a, L. FERENCZ^{2b}

ABSTRACT. A study of ammonia formation in DC plasma discharge is presented in function of gas composition and working temperature by using a laboratory scale plasma nitriding reactor. The nitriding process took place in case of a Hollow Cathode (HC) configuration with treated part on Anodic Potential (HCAPN). It was found that in the temperature range of 500-700 K the yield of ammonia was directly proportional with the discharge current and the coefficient of efficiency was found to be constant. This indicates that ammonia formation in low temperature plasma discharge is electrochemical in nature. During our experiments nitride layers was formed on both the cathode and the inner anode. This indicates that the neutral ammonia molecules have a nitrogen carrying role in the plasma nitriding process.

Keywords: *linear plasma reactor, plasma nitriding, active screen, hollow cathode, anodic potential, formation of ammonia, nitrogen mass transfer.*

1. INTRODUCTION

The study of the formation of ammonia in DC gas discharge has a long history. Brewer and Westhaver [1] have begun its investigation before the 1930's. They detected ammonia in a DC gas discharge containing a mixture of three parts hydrogen and one part nitrogen. The amount of ammonia formed was found to be directly proportional to the current of the discharge and independent of the gas pressure.

^a Sapientia Hungarian University of Transylvania, Human and Technical Sciences Faculty, Electrical Engineering Department, Tîrgu-Mureş/Corunca, RO-540485, Şos. Sighişoarei Nr. 1C, Romania

^b Sapientia Hungarian University of Transylvania, Human and Technical Sciences Faculty, Department of Horticulture, Tîrgu-Mureş/Corunca, RO-540485, Şos. Sighişoarei Nr. 1C, Romania

* Corresponding author: l_kenez@ms.sapientia.ro

They removed the ammonia formed from the discharge space by freezing. According to Auner's patent [2] from 2013, ammonia can be produced using a gas mixture of three parts hydrogen and one part nitrogen in a low power (10 W) gas discharge between two electrodes inside of a quartz tube. This method simultaneously superimposes a high frequency discharge (2.45 GHz, 800 W, 1 msec impulse and 19 msec pauses). The formed ammonia is then frozen in a trap at 77 K, dissolved in water and quantitatively analyzed. Burlakov and others [3] detected ammonia in an active screen plasma nitriding (ASPN) industrial installation. They found that the maximum amount of ammonia (1.2% vol. of the incoming gas mixture supply) is produced when the supplied gas mixture has a ratio of hydrogen to nitrogen is 1:1. They observed that the amount of ammonia formed decreased with the increase of the temperature. They concluded that the role of NH_3 in the ASPN process was not well-defined and needed further study. Skalecki and others [4] studied the influence of plasma treatment parameters, and of the nitrogen to hydrogen ratio on the atmosphere and on the formation of ammonia during plasma nitriding. By correlating the measured ammonia with the treatment parameters, they could predict the ammonia-content of the exhaust gas. Furthermore, they were able to calculate the plasma nitriding potential based on the ammonia content. They also established the correlation of this nitriding potential to the formation of ϵ and γ' nitride phases. This paper presents the results of our study of the formation of ammonia in a DC plasma discharge, in function of gas composition and the working temperature by using a laboratory scale plasma nitriding reactor. We controlled the temperature by concurrently changing the applied voltage and the current intensity. Similarly, we studied the relationship between the amount of ammonia formed and the intensity of the current. It should be noted that the total electric current in the discharge is formed by the sum of electron and ionic currents. For temperatures at the low end of the nitriding process temperature scale we observed a strictly direct proportionality between the total electric current and the amount of ammonia formed ($\mu\text{mols/sec}$). We determined that over the threshold temperature of 780 K, the decomposition rate of the formed ammonia exceeds its formation rate. Presumably, the decomposing ammonia was a nitrogen transporting medium of the anodic nitriding process.

2. EXPERIMENTAL EQUIPMENT AND PROCEDURE

The studies were performed in a laboratory scale plasma nitriding reactor with a diameter of 0.25 m and length of 1.0 m. The hydrogen-nitrogen mixture has been supplied by a gas generator furnished with two flow-meters. Through pin-valves

the gases passed through a low pressure mixer, where they were well mixed as ideal gases. From the mixer the gas mixture entered the reactor and passed by the electrodes made of unalloyed steel. The gases were then removed from the reactor using a vacuum pump. This gas then was passed through a water-trap with a set amount of water, which dissolved and retained the ammonia from the gas mixture. The dissolved ammonia then was determined volumetrically.

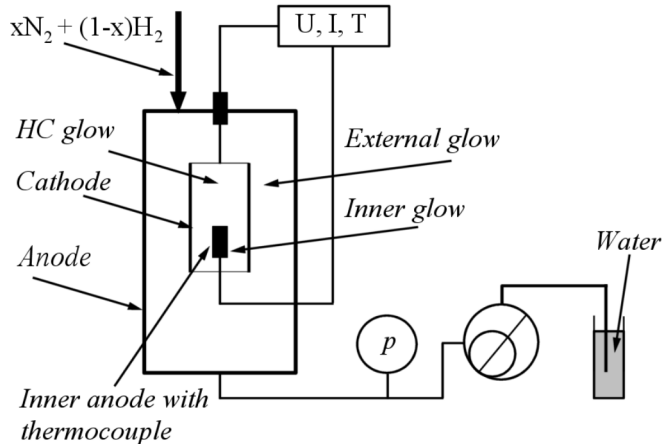


Fig. 1. The diagram of the experimental equipment

In order to increase the amount of ammonia formed, we created a composite discharge space formed by a hollow cathode (0.085x0.2 m) and an auxiliary anode with a thermocouple, placed inside the lower part of the hollow cathode. See Fig. 1. This setup created two abnormal discharges. The first was between the external surface of the hollow cathode and the walls of the reactor (anode). The second one was between the internal wall of the hollow cathode and the auxiliary anode. In addition to these two abnormal discharges, an HC glow discharge was formed in the upper side of the hollow cathode, the anode being the wall of the reactor and the auxiliary anode.

The reactor has been outfitted with a rotary vane pump with a nominal pumping speed of $15\text{m}^3/\text{h}$ or $4.166 \cdot 10^{-3} \text{m}^3/\text{s}$. In function of the volume of the incoming gas supply, the equilibrium pressure was between 200-300 Pa. Varying the voltage of the plasma discharge between 400 to 950 V, the maximum value of the current density has been $22 \text{A}/\text{m}^2$. Under these conditions the electron temperature was 10^4K in the proximity of the anode, while the concentration of electrons was $5 \cdot 10^{14} \text{m}^{-3}$.

3. SAMPLING AND ANALYSIS

The gas mixture exiting the pump was driven through a porous ceramic filter into a known volume of water (250 ml) where the ammonia has been absorbed. Then the samples were stored in airtight containers while awaiting chemical analysis.

The amount of ammonia absorbed during the sampling process has been determined by titration using a hydrochloric acid 0.1 N. A 25 ml ILMABOR Schellbach burette was used to measure the amount of hydrochloric acid solution. Methyl-orange was used as an indicator, its color change occurring at around pH 3.1-4.4. For every experimental setup, we took three samples and we used their averages for our calculations. It should be noted that the values were standardized by dividing the absolute amount of ammonia formed with the sampling time (mMol/sampling time). This standardized amount was transformed into $\mu\text{Mol}/\text{sec}$ or into volumetric percent of the incoming gas mixture - as was needed.

During the first series of experiments, we studied the precision of the analysis methodology i.e. the sample collection and the titration itself. Our assumption was that the absolute amount of ammonia formed in identical conditions had to be proportional with the sampling time.

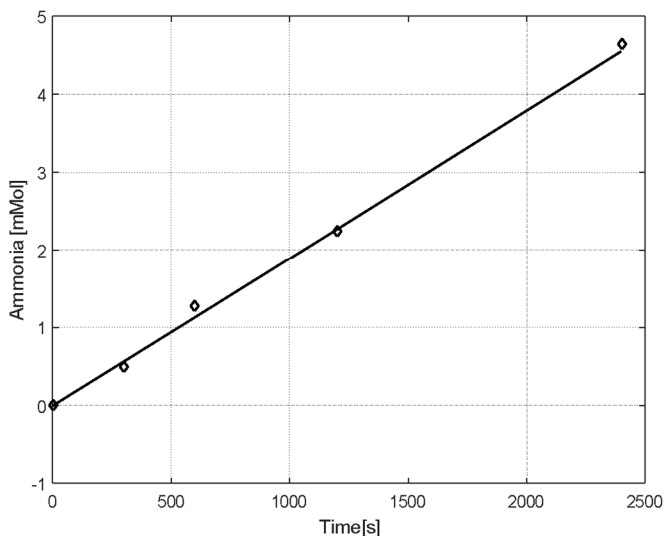


Fig. 2. The absolute amount of ammonia formed in function of sampling time ($T=800\text{ K}$, $Q_v=10^{-5}\text{ m}^3/\text{sec}$)

We used a classical direct current plasma nitriding (DCPN) setup with a central steel cathode (diameter 0.048 m and length 0.2 m). The incoming gas mixture volumes expressed at standard temperature and pressure (STP), were 150 ml/min N₂ and 450 ml/min H₂ i.e. the total volume of 10⁻⁵ m³/sec gas mixture. The temperature of the cathode was 800 K and the sampling times were at 300, 600, 1200 and 2400 seconds. We used 250 ml of bidistilled water to absorb the ammonia from the exhaust gas mixture and a volume of 10 ml of this solution was used for volumetric analysis. The pressure of equilibrium in the reactor was 270 Pa. Based on the results of this experiment, shown in Fig. 2, we were able to state with confidence that the applied methodologies precision was good. The coefficient of determination of the regression line was R²=0.9989.

In the following experiments the sampling times were set at 1200 seconds and we took three samples for each condition of equilibrium. The hollow cathode setup used in our experiments, see Figure 1, allowed the use of higher discharge currents and therefore the formation of larger amounts of ammonia. In doing so, we decreased the relative error of the analysis.

4. FORMATION OF AMMONIA IN FUNCTION OF THE COMPOSITION OF THE GAS MIXTURE

The formation of ammonia has been studied in gas mixtures of composition of xN₂+(1-x)H₂, where the x varied between 0 and 1. During the experiments the volumetric rate of the incoming gas mixture has been maintained at 6.5·10⁻⁶ m³/s and the temperature at 780 K. Based on our previous observations, this was the maximum temperature where the rate of decomposition of the ammonia on the steel electrodes was negligible.

The results of the experiments are presented in Fig. 3. It should be noted that the amount of ammonia formed has been given in terms of volumetric percentage (vol. %) of the incoming gas mixture.

The formation of ammonia started even in a pure hydrogen atmosphere. This phenomenon can be explained by the fact that the cathode was made of low-carbon steel which had been plasma nitrided for more than 100 hours during our previous experiments. The hydrogen dissolved the nitrogen from the ε iron nitride (Fe₂₋₃N) during the plasma discharge and it formed the ammonia.

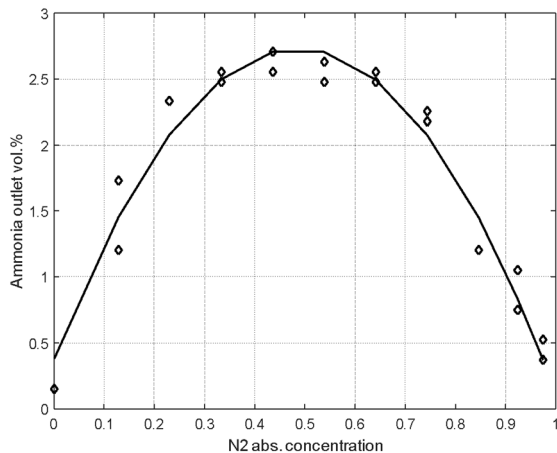


Fig. 3. Formation of ammonia from different gas mixture – $xN_2+(1-x)H_2$.
($T=780\text{ K}$, $Q_v=6.5 \cdot 10^{-6}\text{ m}^3/\text{s}$)

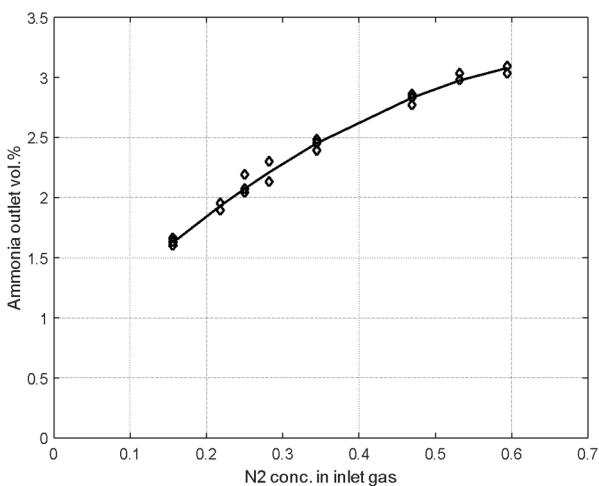


Fig. 4. The amount of ammonia in the outlet gas. ($T=780\text{ K}$, $Q_v=10.67 \cdot 10^{-6}\text{ m}^3/\text{s}$)

The maximum value of the curve occurs at the gas mixture of $0.5\text{ N}_2 + 0.5\text{ H}_2$ and not at the expected theoretical ratio of $0.25\text{ N}_2 + 0.75\text{ H}_2$, just as it has been observed by Burlakov [3] as well. By increasing the volumetric rate of the incoming gas mixture the maximum of the curve moved to the right as shown in Fig. 4. By increasing the volumetric rate of the incoming gas mixture by 60%, from $6.5 \cdot 10^{-6}\text{ m}^3/\text{s}$

to $10.67 \cdot 10^{-6} \text{ m}^3/\text{s}$, the maximum value of the curve moved past the 0.6 N_2 ratio and the amount of ammonia formed has increased substantially. Our assumption is that this behavior depended on the characteristics of the plasma reactor.

5. FROMATION OF AMMONIA IN FUNCTION OF TEMPERATURE

We studied the formation of ammonia in function of the equilibrium temperature. The composition ratio of the gas mixture was set to equal the ratio of nitrogen to hydrogen within the ammonia molecule ($\text{N}_2 + 3\text{H}_2$). During our experimental runs, we kept the volumetric rate of the gas mixture at a constant value of $Q_v = 10.67 \cdot 10^{-6} \text{ m}^3/\text{s}$. The results for the temperatures between 508 – 850 K are shown in Fig. 5.

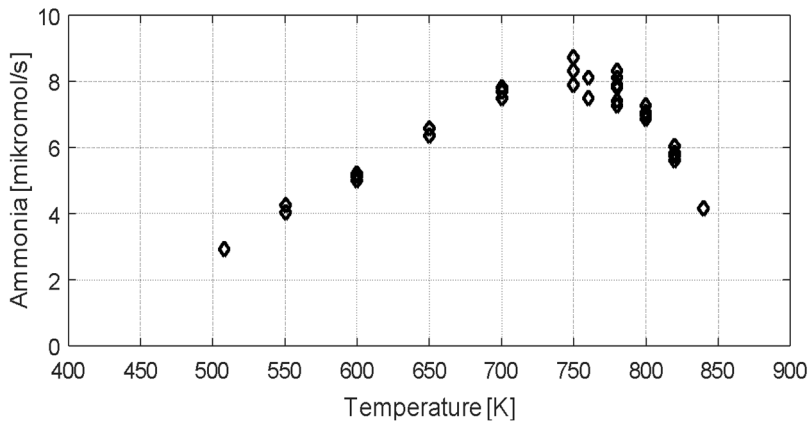


Fig. 5. Yield of ammonia in function of the equilibrium temperature ($Q_v = 10.67 \cdot 10^{-6} \text{ m}^3/\text{s}$; $\text{N}_2/\text{H}_2 = 1/3$).

The lowest equilibrium temperature we used was 508 K. At this temperature the negative light covers the entire surface of the cathode (the condition for an abnormal glow discharge). Up to 750 K, the yield in ammonia is directly proportional to the temperature. At higher temperatures, the yield decreases rapidly. We believe that this decrease is due to the thermal decomposition of the formed ammonia. This decomposition takes place on the surface of the cathode and inner anode, just like in the case of the decomposition that occurs during the classical gas nitriding process [7, 8]. It should be noted that during this process both the cathode and inner anode were nitrided.

6. RELATIONSHIP BETWEEN THE YIELD OF AMMONIA AND CURRENT INTENSITY

We investigated the rate of ammonia formation as a function of current intensity for temperatures lower than the threshold temperature of 750 K. The composition and the volumetric rate of the gas mixture was $N_2/H_2=1/3$ and $Q_v=10.67 \cdot 10^{-6} \text{ m}^3/\text{s}$, respectively. It should be noted that the yield of ammonia ($\mu\text{mol/s}$) has been found to be directly proportional to the temperature at the temperature range at which we performed these tests.

In order to establish a relationship between the amount of ammonia formed and the current intensity, we compared the number of ammonia molecules formed in one second (yield) to the number of elementary electric charge carried by the electric current. We named this ratio coefficient of efficiency:

$$\eta = \frac{v \cdot N_A}{I \cdot n} = \frac{v \cdot N_A}{I \frac{1}{q}}$$

Where the v was the amount of ammonia formed in unit time (mol/s), N_A is the Avogadro number $6.022 \cdot 10^{23}$ molecules/mol, q is the elementary electron charge $1.602 \cdot 10^{-19}$ C, and n is the number of elementary electric charge carried by 1 A current intensity.

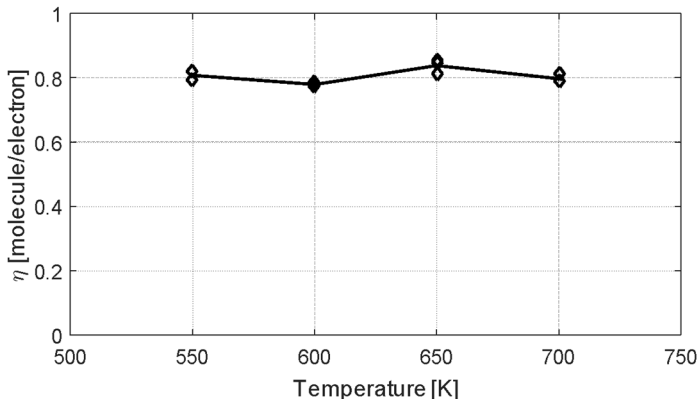


Fig. 6. Relationship of coefficient of efficiency of ammonia formation and temperature

The results of the experiment are summarized in Fig. 6. The coefficient of efficiency was found to be constant, 0.8 NH_3 molecule/elementary electric charge, at the temperatures used in our experiment, i.e. for temperatures below 750 K. We assume that this relationship continued to exist at temperatures higher than

the threshold temperature. This unvarying relationship between the number of ammonia molecules and the elementary electric charge indicates that ammonia formation in low temperature plasma discharge is electrochemical in nature.

7. CONCLUSIONS

Ammonia was formed in a linear plasma reactor using a gas mixture of nitrogen and hydrogen and by applying a DC glow discharge between the electrodes made of steel. From the standpoint of ammonia formation, the optimal composition of the gas mixture depended on the mechanical dimensions of the reactor, the volumetric rate of the supplied gas mixture, and the applied temperature. We studied the formation of ammonia at two different volumetric rates, i.e. at $6.5 \cdot 10^{-6} \text{ m}^3/\text{s}$ and $10.67 \cdot 10^{-6} \text{ m}^3/\text{s}$. The maximum amount of ammonia was formed when the absolute concentration of nitrogen was between 0.5-0.7, depending on the incoming gas mixture volumetric rate. In the temperature interval of 500-700 K the yield of ammonia ($\mu\text{mol/s}$) was directly proportional with the discharge current. The coefficient of efficiency was found to be constant, 0.8 NH_3 molecule/elementary electric charge. This unvarying relationship between the number of ammonia molecules and the elementary electric charge indicates that ammonia formation in low temperature plasma discharge is electrochemical in nature. At temperatures above 750 K the amount of ammonia has decreased in the exhaust gas with the increase of the temperature. This temperature matched the lower limit of the classic gas nitriding process temperature. During our experiments nitride layers have been formed on both the cathode and the inner anode. This indicates that the neutral ammonia molecules have a nitrogen carrying role in the plasma nitriding process. The presence of iron atoms deriving from the cathode sputtering process makes it likely that the mechanism based on intermediary FeNH_{2-3} molecules as proposed by Szabó, A [7] is correct.

9. ACKNOWLEDGEMENT

The authors would like to thank Institute of Research Programs of the Sapientia University (KPI) for supporting the research project and for the accorded research grants over the years. The authors would like to address special thanks to Mr. Szabolcs Farkas for the valuable conversations and suggestions regarding our work and paper.

REFERENCES

- [1] Brewer, A.K., Westhaver, J.W.: Chemical Action in the Glow Discharge II. Further Investigation on Synthesis of Ammonia. *J. Phys. Chem.* 1930. 34 (1), pp 153-164
- [2] Auner, N.: *Method for producing ammonia*, Patent US 20130039834 A1
- [3] Burlakov I., Börner K., Spies. H.-J., Biermann H., Lopatik D., Zimmermann H., Röpcke J.: In-situ monitoring of plasma enhanced nitriding processes using infrared absorption and mass spectroscopy. *Surf. and Coat. Techn.* 206 (2012) 3955-3960
- [4] Skalecki M.G., Klümper-Westkamp H., Hoffmann F., Zoch H-W., Bischoff S., Rohde J.: *Plasma nitriding potential and a new modeling approach for plasma nitriding process control*. HT conf Ohio
- [5] N. Kutasi, L. Kenéz, E. Filep, A. Kelemen, Sz. Mátyási – *Pulsed power supply design for DC and Active Screen Plasma Nitriding*, - MACRO 2013 International Conference on Recent Achievements in Mechatronics, Automation, Computer Science and Robotics Sapientia University, Tg. Mures 2013, pp. 115-122, ISSN 2247 0948.
- [6] Kenéz L., Zsakó Z., Filep E.: Automation of plasma diagnostics measurements performed in a non-isothermal plasma reactor. *Studia UBB Physica* LIII, 1, 2008.
- [7] Szabó A., Wilhelmi H.: *Nitrierung von Stahloberflächen*. HTM 39 (1984) 4 pp 148-181
- [8] Mittemeijer, E.J.: Fundamentals of Nitriding and Nitrocarburizing. *Steel Heat Treating Fundamentals and Processes*, ASM Handbook, 2013; 4(A):619-646.

Dedicated to Professor Dr. Sorin Dan Anghel on His 65th Anniversary

SPIN SUSCEPTIBILITY IN TWO DIMENSIONS

I. GROSU*

ABSTRACT. The static spin susceptibility of a two dimensional electron system is calculated, for two distinct situations. The first system is one with a parabolic dispersion law, and the second system is one with a linear dispersion law, corresponding to graphene systems. The temperature dependence of the static spin susceptibility is analyzed up to room temperatures for both systems.

Keywords: *Static spin susceptibility, two-dimensional systems, parabolic dispersion law, graphene density of states*

INTRODUCTION

The importance of two dimensional electron gas appear in developments in semiconductors through the achievement of structures in which the electronic behavior is two-dimensional. This means that the carriers are confined in a potential such that their motion in one direction is restricted, leaving only a two-dimensional motion in a plane normal to the confining potential. In this respect the important systems with two-dimensional behavior are MOS structures, quantum wells and superlattices [1]. Other important low dimensional systems are high-temperature superconductors [2]. A more recent two-dimensional system discovered is graphene [3,4], with very interesting properties due to its band structure and linear dispersion law. Among these properties are those connected to the magnetic response of the system to an external field [5]. In this paper we will analyze the temperature

* Babes-Bolyai University, Faculty of Physics, 1 Kogalniceanu str., 400084 Cluj-Napoca, Romania, e-mail: ioan.grosu@phys.ubbcluj.ro

dependence of the static spin susceptibility of a two-dimensional system for two different situations, the parabolic and the linear dispersion. The first case correspond to a classical electron gas, and the second correspond to the electronic system of graphene.

MODEL

The static spin susceptibility can be determined using the relation [6,7] :

$$\chi = g_L^2 \mu_B^2 \int dE \frac{\rho(E)}{4k_B T \cosh^2\left(\frac{E - \mu}{2k_B T}\right)} \quad (1)$$

Here: g_L - is the Lande electron g-factor, μ_B - is the Bohr magneton, and μ - is the chemical potential. In the following we will analyze the static spin susceptibility in the case of two-dimensional systems.

The first system we analyze is the electron system with a parabolic dispersion law: $E_k = k^2 / 2m$, where m - is the electron mass. For a unit area, and for both spin orientations ($\hbar = 1$), the electron density of states is [8]:

$$\rho = \frac{m}{\pi} \quad (2)$$

which does not depend on energy. In this case, and in the wide band limit, the static spin susceptibility reduces to:

$$\chi = g_L^2 \mu_B^2 \frac{m}{2\pi} \int_{-\infty}^{\infty} \frac{dx}{\cosh^2 x} = \frac{g_L^2 \mu_B^2 m}{\pi} \quad (3)$$

which is a constant in the entire temperatures interval. In the case of a finite band, $-E_c < E < E_c$, and the spin susceptibility is given by the following formula:

$$\chi = \frac{g_L^2 \mu_B^2 m}{2\pi} \left[\tanh\left(\frac{E_c - \mu}{2k_B T}\right) + \tanh\left(\frac{E_c + \mu}{2k_B T}\right) \right] \quad (4)$$

Here there is an analytical temperature dependence. Additionally, the chemical potential is a function of temperature too. For the parabolic dispersion law, the chemical potential is given by [9]:

$$\mu \equiv \mu(T) = k_B T \ln(e^{E_F/k_B T} - 1) \quad (5)$$

where: $E_F = n\pi/m$ is the Fermi energy, and n - the electron density. Then the spin susceptibility of a two-dimensional system with a finite energy band becomes:

$$\chi = \frac{g_L^2 \mu_B^2 m}{2\pi} \left\{ \tanh \left[\frac{E_c}{2k_B T} - \frac{1}{2} \ln(e^{E_F/k_B T} - 1) \right] + \tanh \left[\frac{E_c}{2k_B T} + \frac{1}{2} \ln(e^{E_F/k_B T} - 1) \right] \right\} \quad (6)$$

In order to estimate this temperature dependence, up to room temperature, we will consider the following parameters: $E_c = 5$ eV, and $E_F = 2$ eV, which are typical values for metallic densities in two dimensions. Up to room temperature ($T \propto 0.03$ eV) the spin susceptibility is not sensitive to temperature. The temperature influence becomes important for temperatures close to the Fermi temperature.

The second system we analyze here is the electron system of graphene, which is a two-dimensional carbon atom based material synthesized about a decade ago [10]. Here the carbon atoms are disposed on a hexagonal lattice. Graphene has unusual properties due to its band structure. The conduction and valence bands touch at six points, two of these being non-equivalent. Around these points the quasiparticle excitations follow a linear Dirac-like energy dispersion:

$$E_{k,\lambda} = \lambda v_F k \quad (7)$$

where: $\lambda = +1$, and: $\lambda = -1$ correspond to the conduction and valence bands respectively, and v_F is the Fermi velocity of graphene. Using eq.(7), the density of states of the graphene is :

$$\rho(E) = \frac{2}{\pi v_F^2} |E| \theta(|E| - E_c) \quad (8)$$

where E_c is the band energy cutoff, and $\theta(x)$ is the Heaviside step function. Using eq.(1) the static susceptibility becomes:

$$\chi = \chi_0 \left\{ \tanh\left(\frac{E_c + \mu}{2k_B T}\right) + \tanh\left(\frac{E_c - \mu}{2k_B T}\right) - \frac{2k_B T}{E_c} \ln \left[\frac{\cosh\left(\frac{E_c + \mu}{2k_B T}\right) \cosh\left(\frac{E_c - \mu}{2k_B T}\right)}{\cosh^2\left(\frac{\mu}{2k_B T}\right)} \right] \right\} \quad (9)$$

with:

$$\chi_0 = \frac{g_L^2 \mu_B^2 E_c}{\pi v_F^2} \quad (10)$$

Here μ is the graphene chemical potential determined using the conservation of the total particle density. For: $T \ll T_F$, where T_F is the Fermi temperature, the approximate value of the chemical potential is given by [11] :

$$\mu \cong E_F \left[1 - \frac{\pi^2}{6} \left(\frac{k_B T}{E_F} \right)^2 \right] \quad (11)$$

The static spin susceptibility in the zero temperature limit, for $E_c > E_F$, reduces to the following result:

$$\chi \equiv \chi(T=0) = \frac{2g_L^2 \mu_B^2 E_F}{\pi v_F^2} \quad (12)$$

If we are interested in the temperature dependence of the spin susceptibility, in the temperature range up to room temperature, and for extrinsic case (when $T_F \propto 1000$ K), we have to approximate eq.(9) to obtain:

$$\chi \cong \chi(T=0) \left[1 - \frac{\pi^2}{6} \left(\frac{k_B T}{E_F} \right)^2 + \frac{2k_B T}{\mu} \cdot \exp\left(-\frac{\mu}{k_B T}\right) \right] \quad (13)$$

This is a slight decreasing function on temperature. For example if: $E_F = 0.1$ eV, and $T = 0.03$ eV, we obtain: $\chi(T = 0.03) \cong 0.893 \cdot \chi(T = 0)$.

CONCLUSIONS

We have calculated the temperature dependence of the static spin susceptibility for two-dimensional electronic systems taking into account the cases of parabolic and linear dispersion law. In the first case the spin susceptibility is not sensitive to temperature, up to room temperature. In the second case, for temperatures up to room temperature, there is a slight temperature dependence. However, these simple results can be drastically affected if one take into consideration other important effects in two-dimensional systems. Among these effects are the presence of disorder [12,13], and the presence of an energy gap in the graphene quasiparticle spectrum [14-17]. These effects affect the temperature dependence of the spin susceptibility [18], and other important physical properties [19] of two-dimensional systems.

REFERENCES

1. T. Ando, A.B. Fowler, F. Stern, *Rev. Mod. Phys.* 54, 437, (1982)
2. E. Dagotto, *Rev. Mod. Phys.* 66, 763, (1994)
3. A.H. Castro Neto, F. Guinea, N.M.R. Pers, K.S. Novoselov, A.K. Geim, *Rev. Mod. Phys.* 81, 109, (2009)
4. S. Das Sarma, S. Adam, E.H. Hwang, E. Rossi, *Rev. Mod. Phys.* 83, 407, (2011)
5. S. Yarlagadda, G.F. Giuliani, *Phys. Rev. B* 40, 5432, (1989)
6. R.K. Pathria, *Statistical mechanics*, Elsevier, (2004)
7. T. Ma, B. Dora, *arXiv*: 0802.2387
8. M.H. Lee, *J. Math. Phys.* 30, 1837, (1989)
9. J.P. McKelvey, *Solid State and Semiconductor Physics*, Harper and Row, New York, (1966)
10. A.K. Geim, K.S. Novoselov, *Nature Mater.* 6, 183, (2007)
11. E.H. Hwang, S. Das Sarma, *Phys. Rev. B* 79, 165404, (2009)
12. B.Y-K. Hu, E.H. Hwang, S. das Sarma, *Phys. Rev. B* 78, 165411, (2008)
13. P.M. Ostrovsky, I.V. Gornyi, A.D. Mirlin, *Phys. Rev. B* 74, 235443, (2006)
14. S.Y. Zhou, et al., *Nature Mater.* 6, 770, (2007)
15. S.Y. Zhou, et al., *Nature Mater.* 7, 259, (2008)
16. G. Li, A. Luican, E.Y. Andrei, *Phys. Rev. Lett.* 102, 176804, (2009)
17. T.L. Makarova, et al., *Sci. Rep.* 5, 13382, (2015)
18. I. Grosu, T.L. Biter, *Physica E* 86, 154, (2017)
19. M. Crisan, I. Grosu, I.Tifrea, *Eur. Phys. J. B* 89, 140, (2016)

Dedicated to Professor Dr. Sorin Dan Anghel on His 65th Anniversary

EFFECT OF STARTING POWDER PREMIXING ON THE INTERPHASE EXCHANGE COUPLING IN Nd₂Fe₁₄B + 10 WT % Fe NANOCOMPOSITES OBTAINED THROUGH MECHANICAL MILLING

R. HIRIAN^a, S. MICAN^a, O. ISNARD^b, L. BARBU^c, V. POP^{a*}

ABSTRACT. In the frame of optimizing the potential, of hard /soft nanocomposites for high performance applications, we report on the effect of starting powder premixing on the structure, microstructure and exchange coupling in hard/soft magnetic phases. Nd₂Fe₁₄B powder was first mixed with Fe powder using two different means: by hand or by using a Turbula Mixer. Moreover, in the hand mixed powders the Fe particle size was changed from 100 to 1 μm, while the samples mixed using the Turbula Mixer contained only Fe particles of around 1 μm in size. The mixed powders were subsequently milled for 6 hours in a planetary ball mill; the calculated impact energy was 77 mJ/impact and 10 kJ/g for the entire duration of process. Good exchange coupling was obtained in all three cases. The samples prepared with Fe < 1 μm particles yielding slightly better results due to better dispersion of the two phases in the final nanocomposite material. The highest energy product was achieved for the sample premixed with the Turbula Mixer ((BH)_{max}=125 kJ/m³) after being annealed at 800 °C for 1.5 min.

Keywords: *spring magnet, milling, short time annealing, mixing method*

^a Babeş-Bolyai University, Faculty of Physics, 1 M. Kogălniceanu, 400084 Cluj-Napoca, Romania

^b Université Grenoble Alpes, Institut Néel, 25 rue des martyrs, F-38042 Grenoble, France ; CNRS, Institut Néel, 25 rue des martyrs, F-38042 Grenoble, France

^c INCDTIM, Cluj-Napoca, RO-400293 Romania; Electron Microscopy Center, Faculty of Biology and Geology, Babes-Bolyai University RO-400006, Cluj-Napoca, Romania

* Corresponding author: viorel.pop@phys.ubbcluj.ro

INTRODUCTION

Permanent magnets are crucial components in many of today's devices, finding their way in a wide range of either ubiquitous or high-tech applications, from windscreen wipers and smart phones to electric cars and wind turbines (Nd-Fe-B magnets have a high end market share of over 50%) [1-3]. Due to the high reliance on rare-earth magnets, pricing issues and the availability of raw materials, several research avenues have been opened to address the problem [4]: the development of new magnetic materials, the investigation of older compounds with potentially high energy products $(BH)_{max}$, the creation of soft/hard magnetic nanocomposites (spring magnets) [5] with a predicted energy product of 1 MJ/m^3 [6], Recycling [1] etc. Soft/hard magnetic nanocomposites are comprised of a fine mixture of exchange coupled hard and soft magnetic phases, ensuring high coercivity, high remanence, and potentially very competitive magnets when comparing the theoretical energy product with current commercial products. The $\text{Nd}_2\text{Fe}_{14}\text{B}/\alpha\text{-Fe}$ spring magnet is interesting not only because of its possible applications, but also from a fundamental research point of view [1-3]. The advantages of spring magnets are numerous: increased thermal stability [7-9], high corrosion resistance [10] and a very high potential energy product [6], but the challenges involved in obtaining such materials are also significant. In order to ensure a good degree of interphase exchange coupling the crystallite size of the soft magnetic phase cannot exceed twice the domain wall thickness of the hard magnetic phase (which presents difficulties with annealing processes), moreover the two magnetic phases must be homogeneously interspersed. The structure and magnetic properties of 6 h mechanically milled (MM) nanocomposites $\text{Nd}_2\text{Fe}_{14}\text{B}/\alpha\text{-Fe}$ were previously studied [11]. After milling, the samples showed poor crystallinity and high defect density. It was shown that the crystallinity of the hard magnetic phase can be restored through short time heat treatment at high temperature, thus limiting the growth of the soft phase crystallites. Therefore, in our current work we have chosen to study the effect of the soft-hard inter-dispersion by mixing the starting powders ($\text{Nd}_2\text{Fe}_{14}\text{B}$ and $\alpha\text{-Fe}$ powder) in several ways, before undergoing the milling and short time annealing procedures, in order to gain a better understanding of the entire synthesis process.

EXPERIMENTAL DETAILS

The $\text{Nd}_2\text{Fe}_{14}\text{B}$ ingots were prepared by first arc-melting the appropriate amount of Fe_{14}B alloy and second a melting along with the stoichiometric amount of Nd in an induction furnace. The resulting ingots were then annealed at $950 \text{ }^\circ\text{C}$ for 72 h in order to stabilize the structure and ensure the homogeneity of the samples. The

Nd₂Fe₁₄B Ingots were crushed and sieved through a sieve with an opening of 500 μm and the resulting powder was mixed with 10 wt% Fe powder. Three powder mixtures were created by varying the type of Fe powder, and mixing method (Table 1).

Table 1. Composition and premixing method for each of the three Nd₂Fe₁₄B + 10 wt% Fe starting powders

Nd ₂ Fe ₁₄ B powder 90 wt%	Fe powder 10 wt%	Mixing Method
Particle size < 500 μm	Particle size < 100 μm	By hand 5 min
Particle size < 500 μm	Particle size < 1 μm	By hand 5 min
Particle size < 500 μm	Particle size < 1 μm	Turbula mixer 15 min

The first mixture was made using Fe < 100 μm and was mixed by hand (HM) for 5 minutes using a spatula. The second mixture was made by using Fe < 1 μm and was also HM for 5 minutes. The last mixture was made using Fe < 1 μm and was mixed for 15 minutes using a Turbula Mixer (TM). Each Nd₂Fe₁₄B + 10 wt% Fe powder mixture was then milled in a planetary ball mill (Frisch Pulverisette 4) for 6 h under Ar gas. The milling vials (80 ml) and balls (15 mm in diameter) were made of 440 C hardened steel. The ratio between the rotation speed of the disc and the relative rotation speed of the vials was $\Omega/\omega = 333/900$ rpm with a ball-to-powder weight ratio of 10:1. The milled samples were then annealed at 700, 750 and 800 °C for 1.5 min and rapidly cooled by immersing in water. The energies involved in the milling process were estimated through computer simulation using the model proposed by M. Abdellaoui and E. Gaffet [12]. The calculations yielded the following values: Shock energy 77 mJ/impact, Friction 10 mJ/impact, Total Shock energy of 26 kJ/g. The effective impact frequency (the frequency with which a ball hits the same powder particle) was also calculated as 0.14 Hz [13]. The structure and microstructure of the annealed samples was investigated by X-ray diffraction (XRD) using a Bruker D8 Advance diffractometer equipped with a Cu source and Bragg Brentano focusing geometry. The mean crystallite sizes were evaluated from Scanning Electron Microscopy (SEM) images and through the Scherrer [14] method from XRD. The full width at half maximum (FWHM) of α -Fe ($2\theta = 82.3^\circ$) and Nd₂Fe₁₄B ($2\theta = 37.3^\circ$) peaks was determined by fitting the peaks with the sum of two Pseudo-Voigt functions of the same shape and an intensity ratio of 0.5 (corresponding to the Cu-K α 1 and K α 2 components of the X-ray radiation). Because the evaluations were made on annealed samples, the influence of internal stress on the FWHM was neglected. For magnetic measurements, the powder samples were blocked in epoxy resin. The demagnetization curves were recorded at 300 K using the extraction method in applied fields of ± 10 T. Considering isolated spherical magnetic particles we used a demagnetization factor of 1/3 for the magnetic data and for the calculation of the internal field, H_{int} .

RESULTS AND DISCUSSIONS

The XRD patterns for all milled and annealed samples, Figure 1, show an increase in the crystallinity of both the $\text{Nd}_2\text{Fe}_{14}\text{B}$ and $\alpha\text{-Fe}$ phases as the annealing temperature increases from 700 to 800 °C. No significant differences could be observed between the samples annealed at the same temperature.

The average crystallite sizes for the soft magnetic phase (Figure 2) present the same behavior for all three starting powder types, the $\text{Fe} < 1 \mu\text{m}$ starting powder yielding the same values (within the experimental error) as the $\text{Fe} < 100 \mu\text{m}$ starting powder.

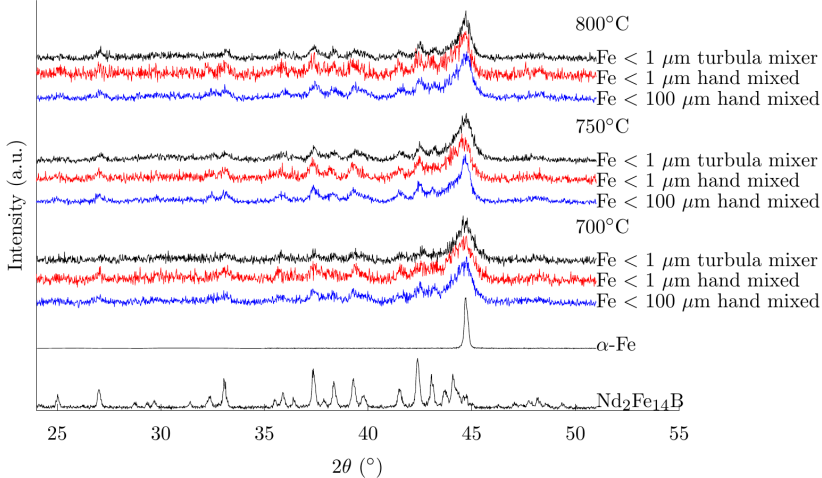


Figure 1. Normalized XRD patterns for the 6 h MM and annealed for 1.5 min at 700, 750 and 800 °C $\text{Nd}_2\text{Fe}_{14}\text{B} + 10 \text{ wt}\% \alpha\text{-Fe}$ nanocomposite samples obtained using the 3 different starting powders

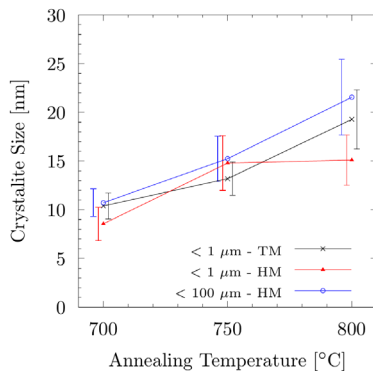
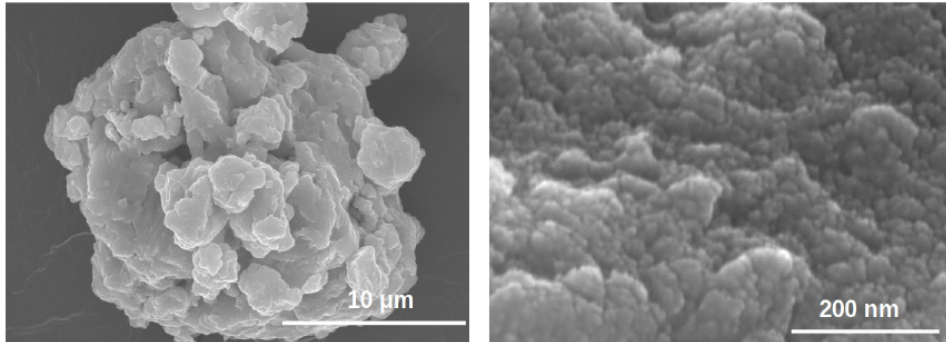
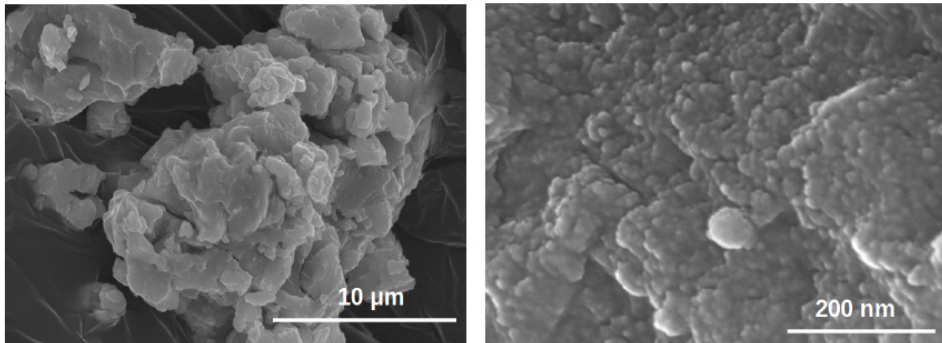


Figure 2. Average crystallite sizes corresponding to soft $\alpha\text{-Fe}$ phase for the 6 h MM and annealed for 1.5 min at 700, 750 and 800 °C $\text{Nd}_2\text{Fe}_{14}\text{B} + 10 \text{ wt}\% \alpha\text{-Fe}$ nanocomposite samples obtained using the 3 different starting powders

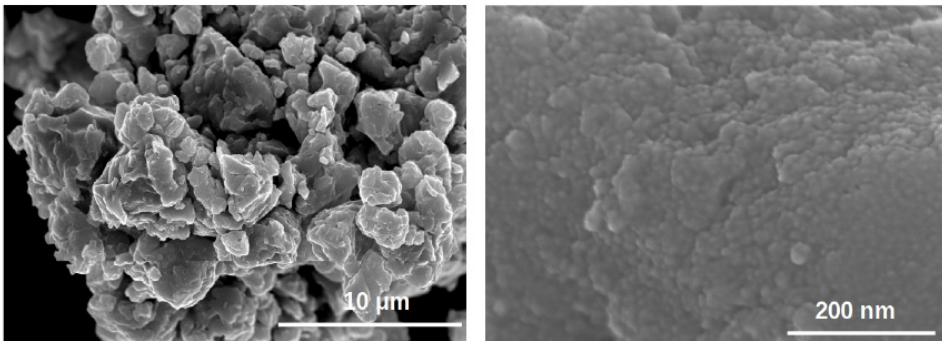
EFFECT OF STARTING POWDER PREMIXING ON THE INTERPHASE EXCHANGE COUPLING
IN $\text{Nd}_2\text{Fe}_{14}\text{B}$ + 10 WT % Fe NANOCOMPOSITES OBTAINED THROUGH MECHANICAL MILLING



(a) $\text{Fe} < 1 \mu\text{m}$ - Mixed using Turbula Mixer



(b) $\text{Fe} < 1 \mu\text{m}$ - Mixed by hand



(c) $\text{Fe} < 100 \mu\text{m}$ - Mixed by hand

Figure 3. SEM images of 6 h MM $\text{Nd}_2\text{Fe}_{14}\text{B}$ + 10 wt% Fe

SEM images of the three different sample sets were taken in Figure 3. At a scale of $10\ \mu\text{m}$ we clearly see that the powder particles are formed of agglomerations of nano-crystallites, while the images taken at a higher magnification ($200\ \text{nm}$) support the values for the average grain sizes assessed through XRD (Figure 2).

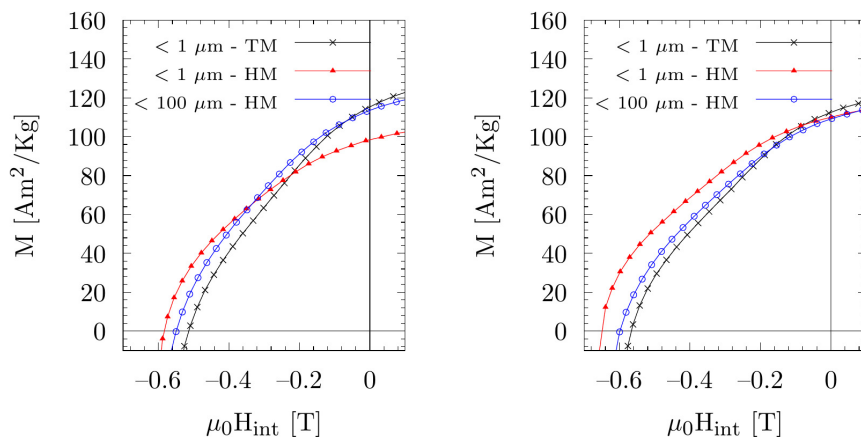
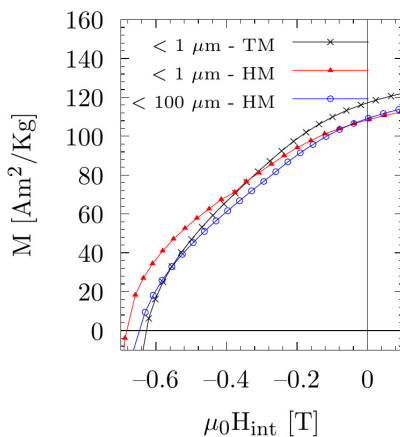
(a) Annealed 1.5 min 700°C (b) Annealed 1.5 min 750°C (c) Annealed 1.5 min 800°C

Figure 4. Demagnetization curves at 300 K for the 6 h MM and subsequently annealed $\text{Nd}_2\text{Fe}_{14}\text{B}+10\ \text{wt}\% \text{Fe}$ nanocomposite powders obtained from the 3 different starting powder mixtures

From the demagnetization curves (Figure 4) we can see that the magnetic properties of all samples improve with increasing annealing temperature: the coercivity, the remanence and the squareness of the demagnetization curves increase. The samples annealed for 1.5 min at 800 °C (Figure 4c) presenting significant improvements over the ones annealed for the same time at 700 °C (Figure 4a). Of these we note the very smooth curve of the sample which was premixed using the Turbula mixer which is indicative of good exchange coupling.

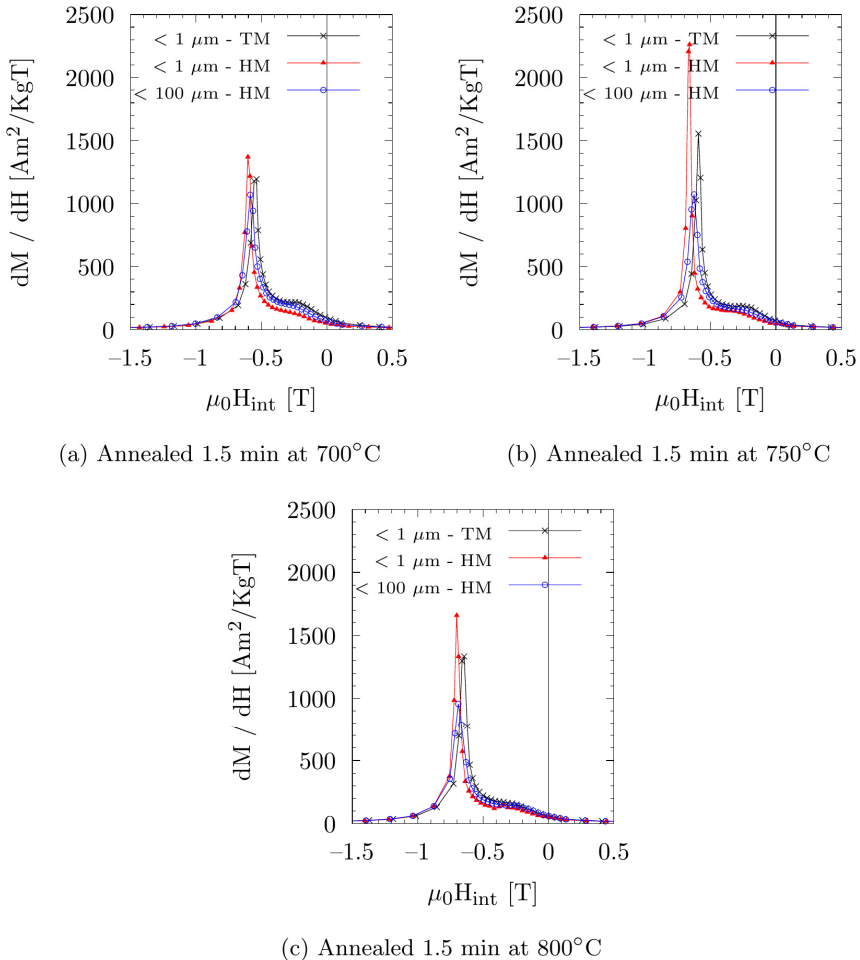


Figure 5. Derivative of the magnetization at 300 K as a function of the internal field for the 6 h MM and subsequently annealed $\text{Nd}_2\text{Fe}_{14}\text{B} + 10 \text{ wt}\% \text{ Fe}$ nanocomposite powders obtained from the 3 different starting powder mixtures

The quality of the magnetic interphase exchange coupling was further evaluated by dM/dH vs H plots (Figure 5) where the peaks at high fields are indicative of good exchange coupling between the two phases, while the peaks at low values of H denote poor exchange coupling of soft phase with high coercivity hard magnetic phase. The samples annealed for 1.5 min at 700 °C (Figure 5a) present a similar behavior, with a large peak at high field and a very small one at low values of H . As the annealing temperature is increased to 750 °C (Figure 5b) the samples produced with $Fe < 1 \mu m$ show a much higher peak at high fields than the sample produces with the starting powder containing larger $Fe < 100 \mu m$. All other things being the same, this implies that the smaller grains allow for a better dispersal of the Fe particles which in turn lead to improved magnetic interphase exchange coupling. At the highest annealing temperature (Figure 5c) the samples produced with $Fe < 1 \mu m$ still present the higher peaks at high field. The samples which were mixed by hand show a very small peak at low field while the ones mixed with a Turbula mixer present a smoother transition. Continuing our previous reasoning we must conclude that the slight improvement in exchange coupling is due to the very good dispersal of α - Fe in the $Nd_2Fe_{14}B + \alpha$ - Fe starting powder by Turbula mixing.

In the case of the coercive field, Figure 6a, we can see that it increases slightly with annealing temperature, for all samples due to the increase in the crystallinity of the hard magnetic phase. Furthermore, across all temperatures, the hand mixed samples present higher values for the coercive field. This could be viewed as an indirect indicator for the efficiency of the magnetic interphase exchange coupling due to the fact that we generally see a drop in H_c and an increasing of M_r when coupling takes place. Furthermore this behavior correlates with the slightly higher remanence exhibited by the samples mixed with a Turbula mixer, Figure 6b.

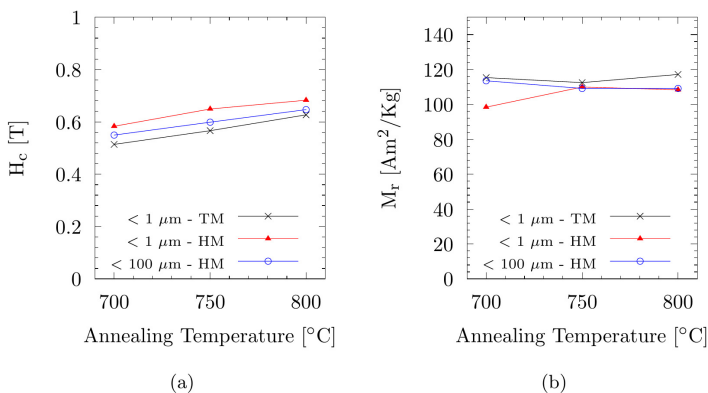


Figure 6. Coercive field (a) and Remanence (b) for the 6 h MM and subsequently annealed $Nd_2Fe_{14}B + 10$ wt% Fe nanocomposite powders obtained from the 3 different starting powder mixtures

EFFECT OF STARTING POWDER PREMIXING ON THE INTERPHASE EXCHANGE COUPLING
IN $\text{Nd}_2\text{Fe}_{14}\text{B} + 10 \text{ WT } \% \text{ Fe}$ NANOCOMPOSITES OBTAINED THROUGH MECHANICAL MILLING

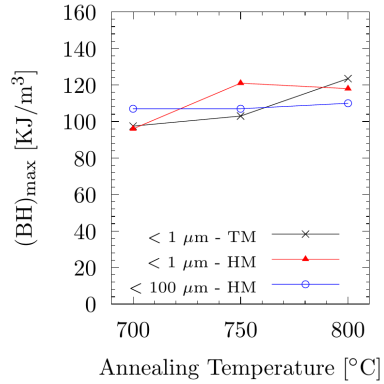


Figure 7. Energy product $(BH)_{\max}$ for the 6 h MM and subsequently annealed $\text{Nd}_2\text{Fe}_{14}\text{B} + 10 \text{ wt}\% \text{ Fe}$ nanocomposite powders produced from the 3 different starting powder mixtures

The energy product $(BH)_{\max}$ was calculated for the 6 h MM and annealed samples (Figure 7). The samples prepared with $\text{Fe} < 1 \mu\text{m}$ show an increase in the energy product with the increase in annealing temperature, while for the samples prepared with the powder mixture containing larger Fe particles the energy product remains relatively constant. The highest energy value 125 kJ/m^3 was recorded for the samples prepared using the Turbula mixer.

CONCLUSIONS

In summary the effect of starting powder premixing on the interphase exchange coupling in $\text{Nd}_2\text{Fe}_{14}\text{B} + 10 \text{ wt}\% \alpha\text{-Fe}$ nanocomposites was studied by varying the size of the initial Fe particles (1 or $100 \mu\text{m}$) and by varying the mixing method (by hand or using a Turbula mixer). After annealing at 700 , 750 and $800 \text{ }^\circ\text{C}$ small improvements in the demagnetization curves were observed for the samples made using the smaller Fe particles as they can disperse better in the nanocomposite. Moreover further improvement was obtained when using the Turbula mixer denoted by the smoothness of the demagnetization curve and by the correlated variation in H_c and M_r .

To conclude, increasing the homogeneity of the starting powder slightly increases magnetic performance in $\text{Nd}_2\text{Fe}_{14}\text{B} + 10 \text{ wt}\% \alpha\text{-Fe}$ obtained by mechanical milling. The highest energy product of 125 kJ/m^3 being obtained for the sample premixed using a Turbula mixer.

ACKNOWLEDGMENTS

Financial support of Romanian Ministry of Education and Research, grants PN-II-ID-PCE-2012-4-0470 and PN-II-RU-TE-2014-4-2360.

We would like to thank the technical support staff at Institut Neel, Grenoble, France for all their help.

REFERENCES

- [1] R. Skomski, *Springer Series in Materials Science*, 231, 359 – 395 (2016).
- [2] J.M.D. Coey, *IEEE Transactions on Magnetics*, 47, 4671–4681, (2011).
- [3] R. Skomski, P. Manchanda, P. Kumar, B. Balamurugan, A. Kashyap, D. Sellmyer, *IEEE Transactions on Magnetics* 49, 3215 - 3220,(2013).
- [4] M.D. Kuzmin, K.P. Skokov, H. Jian, I. Radulov, O. Gutfleisch, *Journal of Physics: Condensed Matter*, 26, 064205, (2014).
- [5] E.F. Kneller, R. Hawig, *IEEE Transactions on Magnetics* 27, 3588–3560, (1991)
- [6] R. Skomski, J.M.D. Coey, *Phys. Rev. B*, 48, 15812–15816, (1993).
- [7] D. Goll, M. Seeger, H. Kronmüller, *Journal of Magnetism and Magnetic Materials*, 185, 49 – 60, (1998).
- [8] D. Suess, M. Dahlgren, T. Schrefl, R. Grössinger, J. Fidler, *Journal of Applied Physics*, 87, 6573-6575, (2000).
- [9] V. Neu, K. Hfner, L. Schultz, *Journal of Magnetism and Magnetic Materials*, 322, 1613 – 1616, (2010), *proceedings of the Joint European Magnetic Symposia*.
- [10] M. Jurczyk, J. Jakubowicz, *Journal of Alloys and Compounds*, 311, 292 – 298, (2000).
- [11] R. Hirian, S. Micán, O. Isnard, L. Barbu-Tudoran, V. Pop, *Journal of Alloys and Compounds*, 697, 19-24, (2017)
- [12] M. Abdellaoui, E. Gaffet, *Acta Metallurgica et Materialia*, 43, 1087-1098, (1995)
- [13] D. Maurice, T.H. Courtney, *Metallurgical and Materials Transactions A*, 26, 2431-2435, (1995)
- [14] P. Scherrer, *Gttinger Nachrichten Gesell*, 2, 98-100, (1918).

Dedicated to Professor Dr. Sorin Dan Anghel on His 65th Anniversary

ON THE STRUCTURE AND STABILITY OF NEUTRON STARS. A GENERAL RELATIVISTIC APPROACH

A.S. MARE^a, A. MARCU^{a*}

ABSTRACT. The structure of Neutron Stars (NS) is still unclear and for this reason this paper serves as an attempt to couple the Tolman-Oppenheimer-Volkoff (TOV) equations with a polytropic Equation of State (EoS). For different EoS models coupled with the relativistic TOV equations it could be calculated the critical mass and radius for a neutron star, underlining consequences of the type of EoS used on the mass-radius stable configurations of the NS. Another briefly investigated topic in this paper is to see if the positive cosmological constant bears any role in the evolution of the neutron star.

Keywords: *Neutron Stars, Computational Physics, Theoretical Physics, Astrophysics*

INTRODUCTION

After a relatively massive star ($\sim 10 - 28 M_{\odot}$) burns out its fuel one of the possible outcomes is the star to become a celestial entity known as a Neutron Star. The remaining matter is a very dense, collapsed core, with masses between $0.9-1.9 M_{\odot}$ and a radius just about 10 km [2]. The core is at several times nuclear density and may be composed of exotic matter. In the interior is superconducting and superfluid, with transition temperatures around a billion degrees Kelvin, the only thing stopping gravitational collapse being neutron degeneracy pressure. This structure represents a key interest in physics, because it gives one the chance to study matter in exotic states, which will probably never be available to scientists in controlled environments here, on Earth.

^a Babeş-Bolyai University, Faculty of Physics, 1 Kogălniceanu str., 400084 Cluj-Napoca, Romania

* Corresponding author: alexandru.marcu@phys.ubbcluj.ro

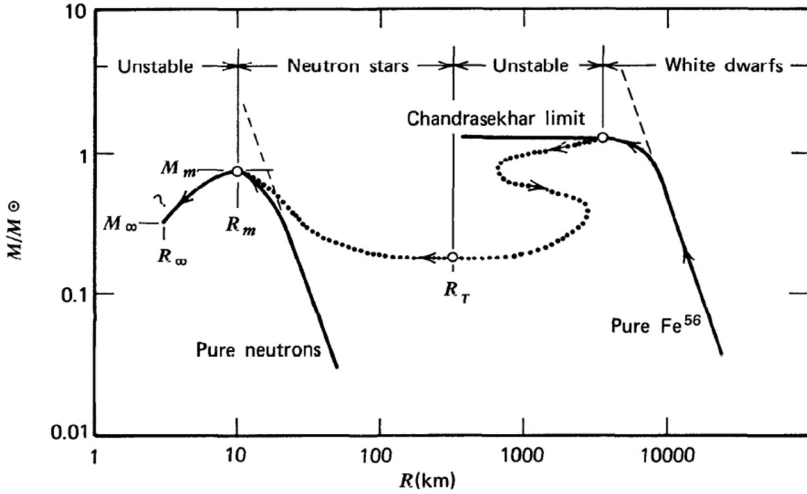


Fig. 1. Different configurations for stellar equilibrium. Note that transitions between stability and instability occur at the maxima and minima points of the curve [1].

The aim of this paper is to tackle the structure problems of this types of stars by analyzing them in a general relativistic framework, using the Tolman-Oppenheimer-Volkoff equations in order to study the internal structure and stable configurations of neutron stars (Figure 1) and the influence of the cosmological constant upon the star. In our approach we used the non-interacting Fermi gas model and, as an ingredient, the introduction of nucleon-nucleon interactions in order to obtain a realistic model.

THEORETICAL DETAILS

Neutron Stars are relativistic objects and for this reason, their structure must be analyzed in a general-relativistic framework. Starting from the Einstein Equations [1],

$$G^{\mu\nu} = \frac{8\pi G}{c^4} T^{\mu\nu} \quad (1)$$

where $G^{\mu\nu}$ is the Einstein tensor, describing the curvature of space-time, and $T^{\mu\nu}$ is the stress-energy tensor, describing matter/energy sources of space-time curvature. The stress-energy tensor, in the case of an ideal fluid, takes the form:

$$T^{\mu\nu} = \left(\rho \left(1 + \frac{\epsilon}{c^2} \right) + \frac{p}{c^2} \right) u^\mu u^\nu + p g^{\mu\nu} \quad (2)$$

where ρ is the baryon rest mass density, ϵ is the specific energy density, p is the fluid pressure, and $g^{\mu\nu}$ is the 4-metric. In the case of vanishing space velocity $u^i = (0,0,0)$ and $T^{\mu\nu} = 0$ (in vacuum) we adopt the form of the interior Schwarzschild metric:

$$ds^2 = -e^{2\Phi(r)} c^2 dt^2 + \left(1 - \frac{2Gm(r)}{rc^2} \right)^{-1} dr^2 + r^2 d\Omega^2 \quad (3)$$

where, $e^\Phi(r)$ is the lapse function, $\Phi(r) = \frac{1}{2} \ln \left(1 - \frac{2GM}{rc^2} \right)$ is the metric potential and $m(r)$ is the gravitational mass inside the radius r . For this model, $m(r) = M(r)$ is the total mass inside the sphere of radius R .

In this framework the Tolman-Oppenheimer-Volkoff equations are [1]:

$$\frac{dp}{dr} = -\frac{G\epsilon(r)M(r)}{c^2 r^2} \left\{ 1 + \frac{p(r)}{\epsilon(r)} \right\} \left\{ 1 + \frac{4\pi r^3 p(r)}{M(r)c^2} \right\} \left\{ 1 - \frac{2GM(r)}{c^2 r} \right\}^{-1} \quad (4)$$

$$\frac{dM}{dr} = 4\pi r^2 \rho \left(1 + \frac{\epsilon(r)}{c^2} \right) \quad (5)$$

$$\frac{d\Phi}{dr} = \frac{m + 4\pi r^3 \frac{p}{c^2}}{r \left(1 - \frac{2Gm}{c^2 r} \right)} \quad (6)$$

In (4) the first two factors in curly brackets, represent special relativity corrections of order v/c^2 (these factors reduce to 1 in the non-relativistic limit) and the last factor is a general relativistic correction. The correction factors are all positively defined. To solve these equations is important to invoke the balance between gravitational forces and internal pressure, the pressure being a function of the Equation of State (EoS). It is necessary to find the conditions to withstand the gravitational attraction (and so the structure equations imply there is a maximum mass that a star can have). Finding the most appropriate and complete EoS will be one of the goals pursued in this paper.

White Dwarfs. Fermi EoS

For free electrons, knowing the number of states, dn , available at momentum k per unit of volume, the electron number density can be calculated [1]:

$$n = \frac{k_F^3}{3\pi^2\hbar^3} \quad (7)$$

where k_F is the Fermi energy, a quantity that varies according to the star's total mass.

Because the electrons are neutralized by protons, accompanied by neutrons, one can neglect the electron mass, m_e , with respect to nucleon mass m_N and so the total mass density of the star is:

$$\rho = nm_N\beta \quad (8)$$

where $\beta = A/Z$ is the number of nucleons per electron.

From (7) and (8) yields:

$$k_F = \hbar \sqrt[3]{\left(\frac{3\pi^2\rho}{\beta m_N}\right)} \quad (9)$$

In the total energy expression the contributions of nucleon masses is proportional with ρ .

$$\epsilon = \beta nm_N + \epsilon_{e^-}(k_F) \quad (10)$$

In the relativist case ($k_F \gg m_e$) the pressure is [8]:

$$p(k_F) = \frac{8\pi}{3(2\pi\hbar)^3} \int_0^{k_F} (k^2 c^2 + m_e^2 c^4)^{-1/2} k^4 dk = \quad (11)$$

simplifies as seen in [8]:

$$p(k_F) = \frac{\epsilon_0}{3} \int_0^{\frac{k_F}{m_e c}} u^3 du = \frac{\hbar c}{12\pi^2} \left(\frac{3\pi^2\rho}{\beta m_N}\right)^{4/3} = K_r \epsilon^{4/3} \quad (12)$$

where $K_R = \frac{\hbar c}{12\pi^2} \left(\frac{3\pi^2}{m_N\beta}\right)^{4/3}$.

For a star having a simple polytropic EoS $p = k\rho^\gamma \sim k\epsilon^\gamma$ it is clear now, from (12), that the relativistic electron Fermi gas has a polytropic EoS with $\gamma = 4/3$.

In a similar way one can establish another polytropic EoS for non-interacting electron Fermi gas model in a non-relativistic case ($k_F \ll m_e$) that yields :

$$K_{NR} = \frac{\hbar c}{15\pi^2 m_e} \left(\frac{3\pi^2}{m_N c^2 \beta}\right)^{\frac{5}{3}} \quad (13)$$

Now the TOV equations(4)(5) can be used, coupled with one of the EoS, to obtain the relationship between $p=p(r)$ and $M=M(r)$ for White Dwarfs(WD). This paper refers to the structural study of neutron stars, but it's simpler to use (8)-(13) for WD (electron degeneracy) and shift to neutrons for the neutron star EoS.

A. Neutron Stars. First EoS model: Fermi neutron gas

Other than (4), we need a EoS for the pure neutron star therefore, our first choice is a Fermi gas model for neutrons instead of electrons.

a. Non-Relativistic Case

For the neutron star the value of K_{NR} is:

$$K_{NR} = \frac{\hbar^2}{15\pi^2 m_N} \left(\frac{3\pi^2}{\beta m_N c^2} \right)^{5/3} = 6.484 \times 10^{-26} \frac{cm^2}{ergs^{2/3}} \quad (14)$$

b. Relativistic Case

The EoS is still polytrope with $\gamma = 1$ [8].

The central pressures expected when computing this case are greater than 10^{-4} . The problem that arises for this EoS because the pressure $\bar{p}(r)$ has never computing zero value and the loop on \bar{r} runs through the whole range, thus giving enormous values for the radii when compared with the expected results. In order to fix this, we need to find a EoS that works for every value of the relativity parameter $\frac{k_F}{m_N c}$. We can do this by trying to fit the energy density as two transcendental functions of pressure [8].

$$\bar{\epsilon}(p) = B_{NR} \bar{p}^{-3/5} + B_R \bar{p}$$

The values of B can be calculated using Mathematica's build in fitting function:

$$B_{NR} = 2.4216, B_R = 2.8663 \quad (15)$$

Eq. (4) can be integrated from $r = 0$ to $r = R$, knowing that $\bar{p}(R) = 0$ and using the EoS from above. The initial values are $\bar{p}(0) > 0$; $\bar{M}(0) = 0$.

Non-Relativistic			Relativistic		
ρ_0	R(km)	$M(M_\odot)$	ρ_0	R(km)	$M(M_\odot)$
10^{-2}	15.0	1.0370	10^{-2}	13.4	0.7166

Using general relativistic corrections, one can see a significant difference between in the star's maximum mass and radius, for a given central pressure (Figures 2 and 3).

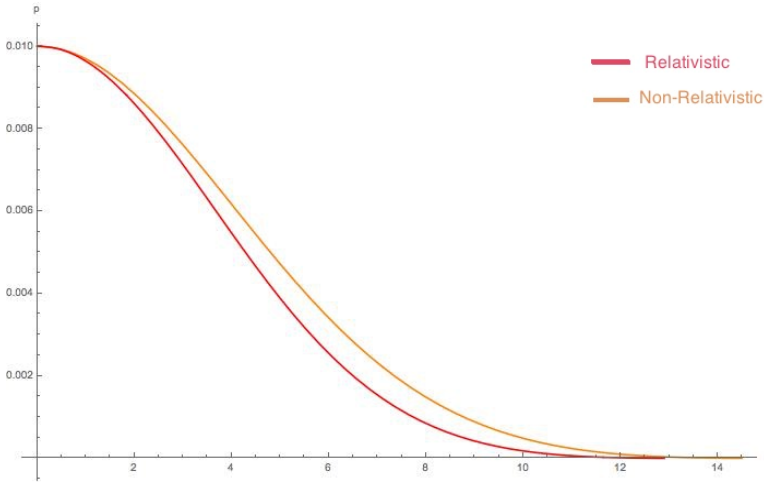


Fig. 2. $\bar{\rho}(r)$ for a neutron star with central pressure of 0.01 with a non-interacting Fermi EoS fit.

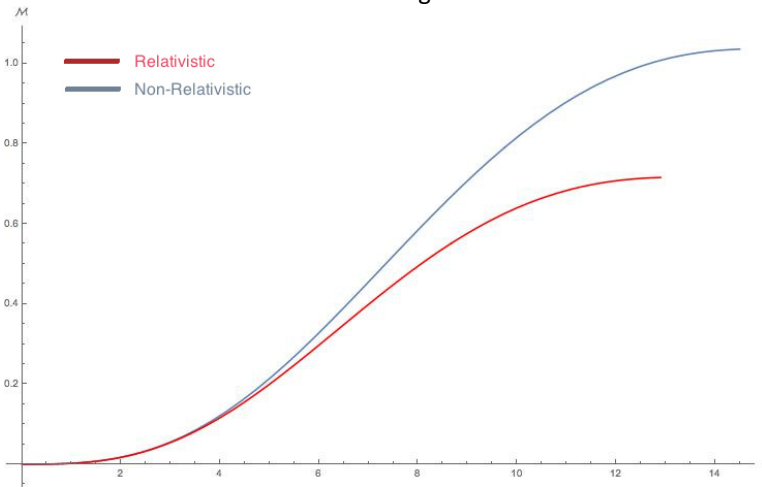


Fig. 3. $\bar{M}(r)$ for a pure neutron star with central pressure of 0.01 using non-interacting Fermi EoS fit.

It can be seen in Figure 3 that for radii bigger than $r = 4$ km, general relativistic (GR) corrections are by all means not negligible, the allowed masses being significantly smaller when using a GR framework.

B. Second EoS model: non-interacting Fermi gas with p^+ and e^-

The presence of protons and electrons in a neutron star is due to the weak decay:

$$n \rightarrow p + e^- + \bar{\nu}_e \quad (16)$$

If this situation is so, and knowing that neutrons have a lifetime of about 15 minutes, then the following question arises: why don't all the neutrons inside the star decay into protons and electrons? Because all the available low-energy levels for the decay proton are already filled up by other protons present and the Pauli exclusion principle kicks, in preventing the neutron beta decay [1].

$$k_{F,p} = k_{F,e} \quad (17)$$

$$\mu_n = \mu_p + \mu_e \quad (18)$$

Charge neutrality is ensured through (17) and weak interaction equilibrium through (18). Integrals for the total pressure and energy density are [8]:

$$p_i(k_{F,i}) = \int_0^{k_{F,i}} (k^2 + m_i)^{-1/2} k^4 dk \quad (19)$$

$$\epsilon_i(k_{F,i}) = \int_0^{k_{F,i}} (k^2 + m_i)^{1/2} k^2 dk \quad (20)$$

where $m_i(i=1,..N)$ is the mass of every individual nucleon and N is the total number of nucleons.

Using Mathematica we can generate a table of values for ϵ_t, p_t over a range of $k_{F,n}$ that can be fitted to the same form used in (15).

The new coefficients obtained are:

$$B_{NR} = 2.572 \quad B_R = 2.891 \quad (21)$$

It can be observed that the coefficients are very similar to those in the case of a pure neutron star and, in fact, the results are extremely similar to that case. We continue on to a more exact EoS, including nuclear interactions.

C. *Third EoS model. Prakash EoS*

In our attempt to introduce nucleon-nucleon interaction we started by developing a simple model for the nuclear potential that reproduces the characteristics of nuclear matter[4].

We know from the von Weizacker mass formula [8] that for symmetric nuclear matter ($N=Z$) the equilibrium density $n_0= 0.16$ nucleons/ fm^3 , that when compared with $m_N = 939 \text{ MeV}/c^2$ tells us that we can use a non-relativistic approach.

$$E_{binding} = \frac{E}{A} - m_N = -16 \text{ MeV} \quad (22)$$

We want our potential to respect (22) by introducing the nuclear compressibility K_0 that is not exactly determined to this day, but it is known to take values between 200-400MeV, and the symmetry energy which brings a contribution of about 30 MeV above the minimum at n_0 [8].

a. *Symmetric nuclear matter*

For symmetric nuclear matter we have:

$$n_n = n_p \quad (23)$$

$$n = n_n + n_p \quad (24)$$

The potential will be constructed with the aid of two functions and three parameters and the nuclear potential will be included in the energy density.

The potential in $\epsilon(n)$ will be [8]:

$$\frac{\epsilon(n)}{n} = m_N + \frac{3 \hbar^2 k_F^2}{5 2 m_N} + \frac{A}{2} u + \frac{B}{\sigma+1} u^\sigma \quad (25)$$

where $u = \frac{n}{n_0}$

In (25) the first term represents the rest mass energy and the second is the average kinetic energy/nucleon.

The kinetic energy term will be abbreviated as $\langle E_F^0 \rangle \cong 22.1 \text{ MeV}$ for $k_F^0 = k_F(n_0)$.

We can find out the values of A,B and σ :

$$\left\{ \begin{array}{l} \langle E_F^0 \rangle + \frac{A}{2} + \frac{B}{\sigma + 1} = E_{binding} \end{array} \right. \quad (26)$$

$$\left\{ \begin{array}{l} \frac{2}{3} \langle E_F^0 \rangle + \frac{A}{2} + \frac{B\sigma}{\sigma + 1} = 0 \end{array} \right. \quad (27)$$

$$\left\{ \begin{array}{l} \frac{10}{9} \langle E_F^0 \rangle + A + B\sigma = \frac{K_0}{9} \end{array} \right. \quad (28)$$

Solving this system we get the values for A, B, σ in terms of K_0 as seen in Table 1.

Table 1. Values obtained by solving the system (26)(27)(28) using Wolfram Mathematica for different values of the compressibility K_0 .

$K_0(\text{MeV})$	$A(\text{MeV})$	$B(\text{MeV})$	σ
200	-366.188	313.348	1.16117
250	-193.367	140.527	1.39891
300	-149.617	96.7769	1.63665
350	-129.658	76.8176	1.8744
400	-118.232	65.3916	2.11214

The pressure is [8] (Figure 4)

$$p(n) = n^2 \frac{d}{dn} \left(\frac{\epsilon}{n} \right) = n_0 \left[\frac{2}{3} \langle E_F^0 \rangle u^{5/3} + \frac{A}{2} u^2 + \frac{B\sigma}{\sigma+1} u^{\sigma+1} \right] \quad (29)$$

where $u=n/n_0$.

We can see that the minima is located at $u=1$ (Figure 4) and has the same depth of -16MeV independent of the compressibility. The second derivatives of these curves correspond to the nuclear compressibility (K_0).

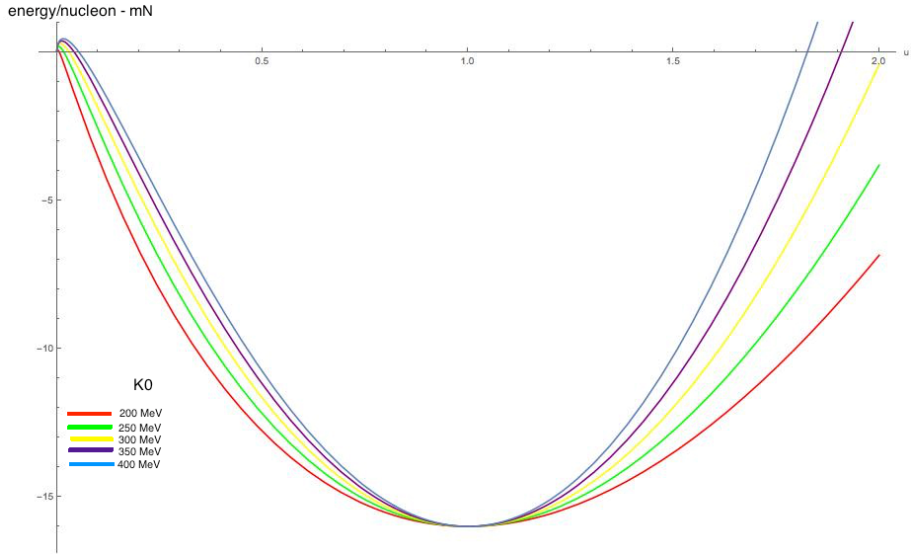


Fig. 4. The average energy/nucleon minus it's rest mass as a function of $u = \frac{n}{n_0}$ for different values of K_0 .

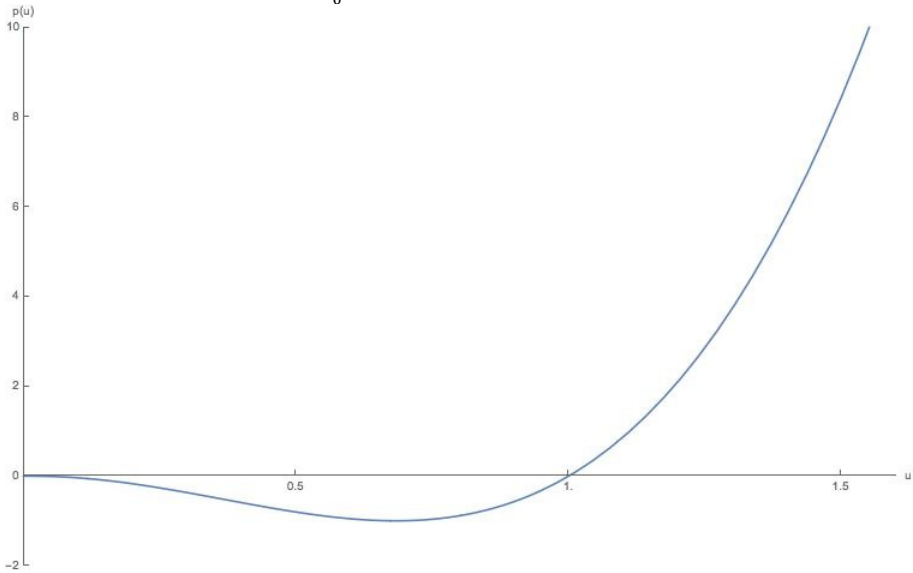


Fig. 5. Dependence of pressure on u.

Figure 5 shows that the pressure is negative for values of u between [0,1] which denotes instability for $u < 1 (n < n_0)$.

b. Non-symmetric Nuclear matter

We tackle the non symmetric nuclear matter by introducing a parameter, α , to represent the neutron and proton densities [4]:

$$n_n = \frac{1+\alpha}{2}n \quad n_p = \frac{1-\alpha}{2}n \quad (30)$$

where $n = n_p + n_n$.

α is real and has a range from 0 to 1, being 1 for pure neutron matter and 0 for symmetric nuclear matter discussed above.

$$\alpha = \frac{n_n - n_p}{n} = \frac{N-Z}{A} \quad (31)$$

Following Prakash[4] we can expect the isospin symmetry breaking interaction to depend through proportionality to α^p , where p is an integer.

Taking into account the kinetic energy contributions of neutrons and protons results:

$$\epsilon_{KE}(n, \alpha) = \frac{3}{5} \frac{k_{F,n}^2}{2m_N} n_n + \frac{k_{F,p}^2}{2m_N} n_p \quad (32)$$

where $m_N \cong m_p$.

The kinetic energy parametrized by α [4] has the expression:

$$\epsilon_{KE}(n, \alpha) = n \langle E_F \rangle \frac{1}{2} \left[(1 + \alpha)^{5/3} + (1 - \alpha)^{5/3} \right] \quad (33)$$

with $\langle E_F \rangle = \frac{3}{5} \frac{\hbar^2}{2m_N} \left(\frac{3\pi^2 n}{2} \right)^{2/3}$ being the mean kinetic energy of symmetric nuclear matter

The excess kinetic energy has the form [8]:

$$\Delta\epsilon_{KE}(n, \alpha) = n \langle E_F \rangle \left\{ \frac{1}{2} \left[(1 + \alpha)^{5/3} - (1 - \alpha)^{5/3} \right] - 1 \right\} \quad (34)$$

Making $\alpha = 1$ (pure neutron matter) yields:

$$\Delta\epsilon_{KE} = n \langle E_F \rangle (2^{2/3} - 1) \quad (35)$$

If we expand to leading order in α , we reach all our goals keeping the terms of order α^2 . Assuming a quadratic approximation in α , for the potential contribution, the total energy per particle will be [8]:

$$E(n, \alpha) = E(n, 0) + \alpha^2 S(n) \tag{36}$$

The isospin symmetry breaking is proportional to α^2 [4], therefore we assume a form for $S(u)$:

$$S(u) = \left(2^{\frac{2}{3}} - 1\right) \frac{3}{5} \langle E_F \rangle \left(u^{\frac{2}{3}} - F(u)\right) + S_0 F(u) \tag{37}$$

where $F(u)$ is a arbitrary function. The following conditions must be satisfied: $F(1) = 1$ because $S(u=1) = S_0$ and $F(0) = 0$. If choosing to use $F(u)=u$ form [4] and [8], then S_0 (the bulk symmetry energy parameter) is 30 MeV (Figure 6).

From Figure 6 it can be seen that, in the vicinity of $u=1$, the average energy per neutron is independent of the values of the compressibility(K_0).

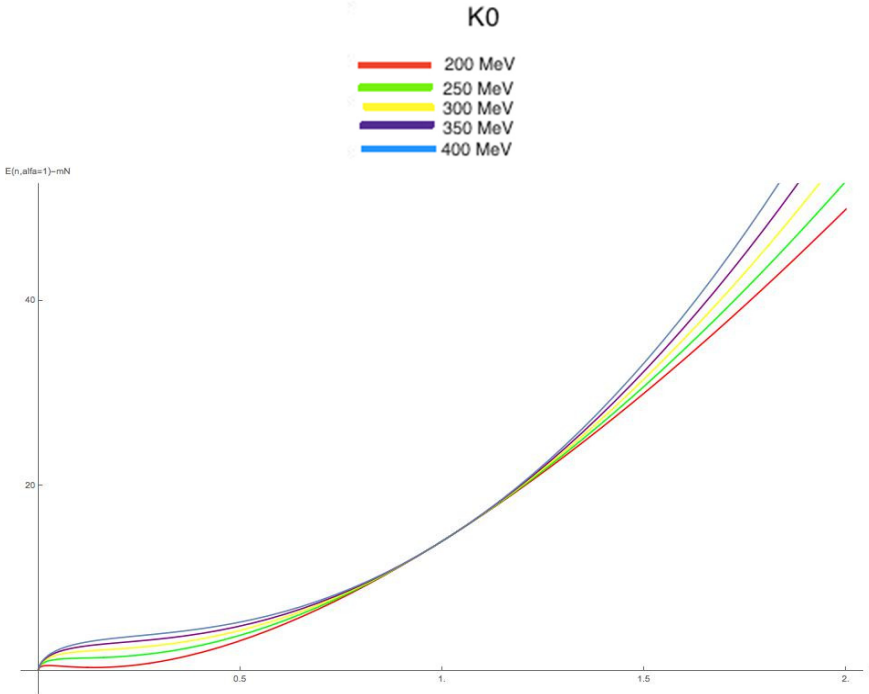


Fig. 6. Average energy per neutron minus it's rest mass as a function of $u=n/n_0$ for different values of compressibility(K_0).

The pressure [8],[4] in this case yields (Figures 7 and 8):

$$p(n, x) = u \frac{d}{du} \epsilon(n, \alpha) - \epsilon(n, \alpha) \quad (38)$$

$$p(n, x) = p(n, 0) + n_0 \alpha^2 \left[\frac{\frac{2}{23}-1}{5} \langle E_F^0 \rangle (2u^{\frac{5}{3}} - 3u^2) + S_0 u^2 \right] \quad (39)$$

where $u = \frac{n}{n_0}$.

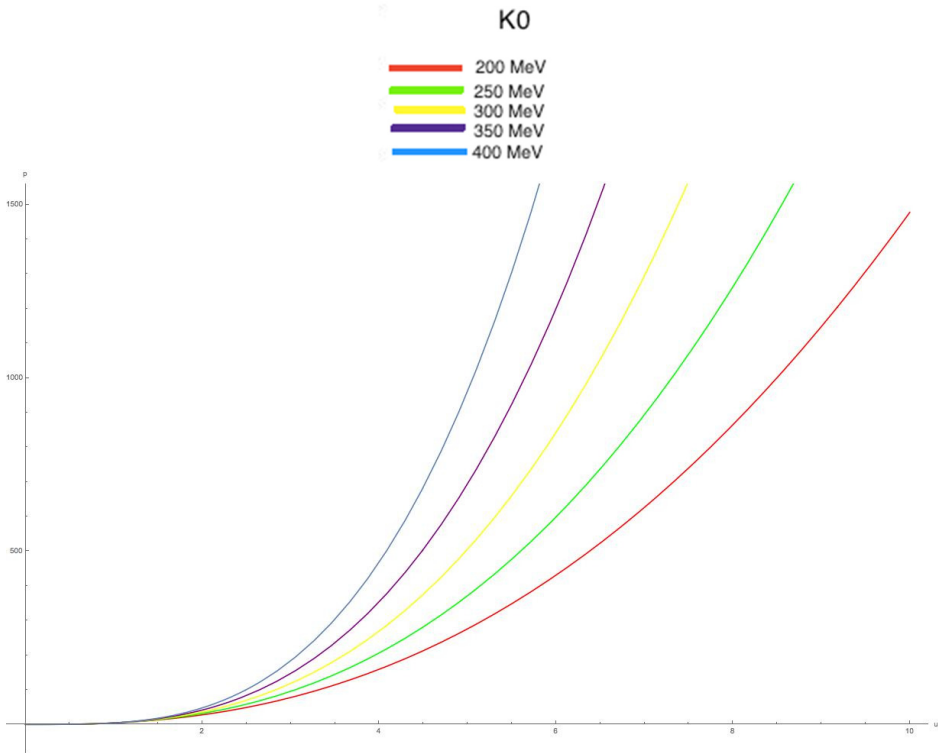


Fig. 7. Pressure as a function of $u=n/n_0$ for different values of K_0 ranging from [200-400]MeV

Figure 7 shows that the pressure increase smoothly from $u=0$, we have a monotonic, non-negative pressure. This suggests that we can try another polytropic fit.

By fitting the data in Mathematica, we have obtained:

$$K_0 = 3.54842 \times 10^{-4}$$

$$\gamma = 2.1$$

Using this polytropic equation now we can repeat the procedures shown above to see the maximum mass and radius of a neutron star using Fermi gas with nucleon-nucleon interactions.

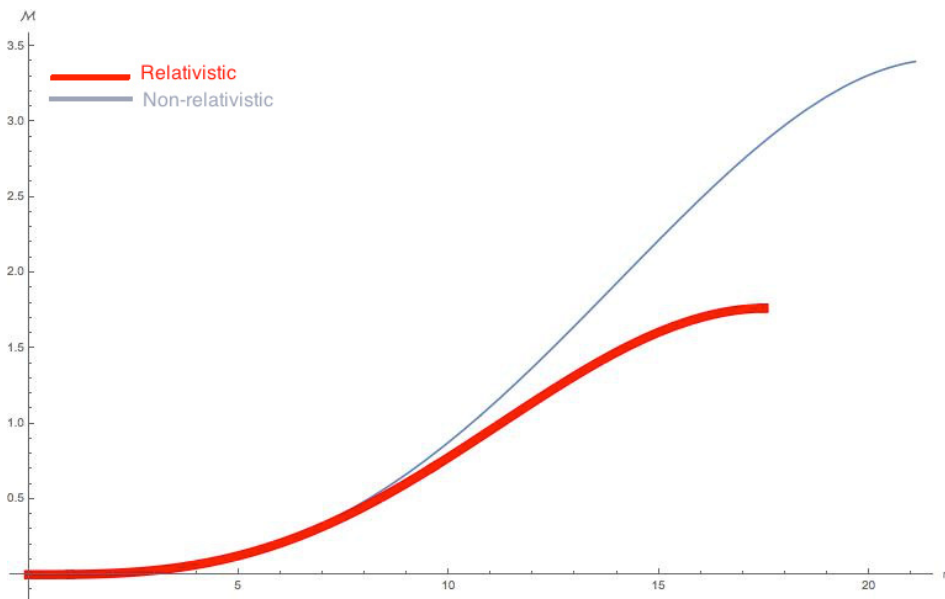


Fig. 8. Mass dependency on r for both relativistic and non-relativistic TOV equation using Prakash EoS

In Figure 8, we have obtained similar curves for $r < 7$ km, but for radii over 7 km, general relativistic effects can not to be neglected, similarly with the Fermi EoS (Figure 3), the actual allowed mass is smaller than it's Newtonian mass.

Figure 9 shows, for general relativistic case, a much steeper decrease in pressure slope for $r > 4$ km.

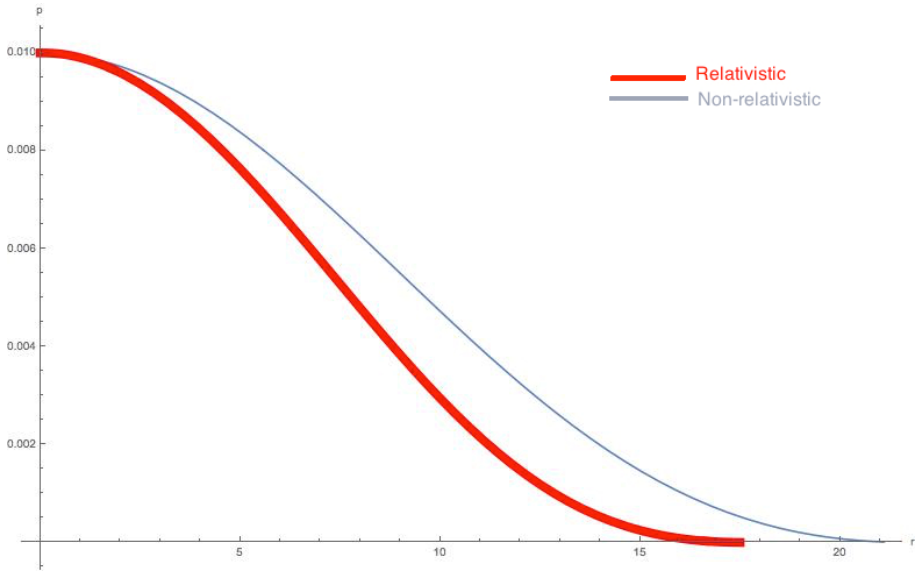


Fig. 9. Pressure dependency on r using Prakash EoS.

RESULTS AND DISCUSSION

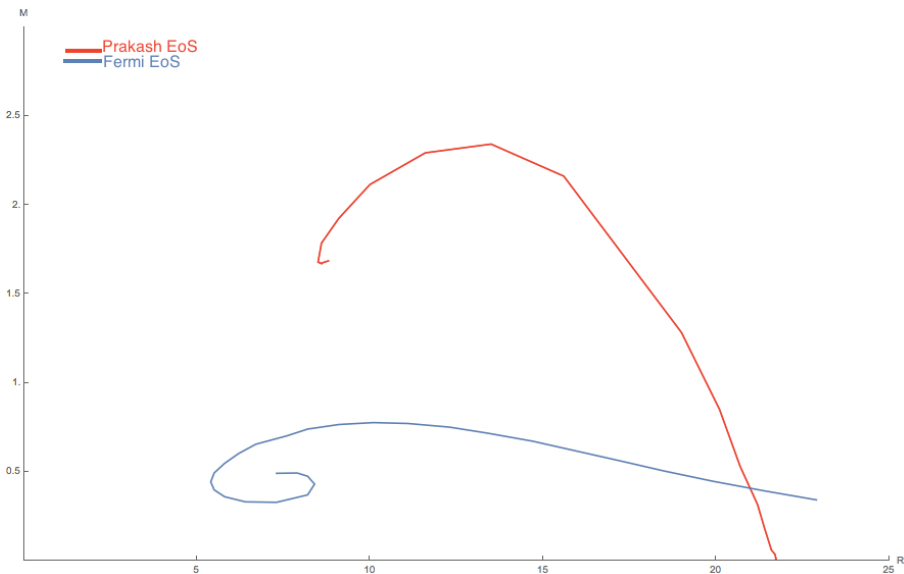


Fig. 10. The mass M (in M_{\odot}) and radius R (in km) for pure neutron stars using a Fermi EoS (blue) and using Prakash EoS.

From Figure 10 one can see that stars that have low-mass and large radius are solutions of the TOV equations for small central pressures. The maxima of this graph occurs at $R=11$ (Fermi EoS) and $R=13.6$ (Prakash EoS) and stars that are positioned to the right of the maximum are stable, while those on the left suffer from gravitational collapse. Thus we can conclude that changes in energy density and pressure are caused by changes in density (given that the thermal component in stars that are cold is negligible). Also it can be seen that including nucleon-nucleon interactions into the EoS has a strong effect on the stability of the star, increasing the maximum mass that a stable neutron star can have.

Including the cosmological constant

For a non-zero cosmological constant the modified Einstein Equations solution get a modified version of equation (4) [8]

$$\frac{dp}{dr} = -\frac{G\epsilon(r)M(r)}{c^2r^2} \left(1 + \frac{p(r)}{\epsilon(r)}\right) \left(1 + \frac{4\pi r^3 p(r)}{M(r)c^2} - \frac{\Lambda r^3}{2GM(r)}\right) \left(1 - \frac{2GM(r)}{c^2r}\right)^{-1} \quad (40)$$

where $\Lambda \approx 1,76 \times 10^{-52} \text{ (m}^{-2}\text{)}$ [9].

Using (40) instead of (4) in our simulations we concluded that there is no noticeable difference in the variation of the pressure and energy density as a function of r (Figures 9 and 10).

CONCLUSIONS

The structure of neutron stars is to the day a very active topic in theoretical and computational physics. Our goal was to construct an Equation of State as simple and efficient as possible, starting with some idealistic approximations and to compute and analyze the consequences. This model is still upgradable, for instance the assumption that inside the neutron star is a QCP(quark-gluon plasma) can be used and then a polytropic EoS of this type won't fit anymore.

REFERENCES

- [1] S. Weinberg, "*Gravitation and Cosmology: Principles and Applications of General Theory of Relativity*", S. Weinberg, John Wiley & Sons Inc, 1972.
- [2] J.R. Oppenheimer, G.M. Volkoff, *Physical Review Letters* Vol.55, Pg.374-381, 1939.
- [3] J.M Blatt, V.F. Weisskopf, "*Theoretical Nuclear Physics*", John Wiley & Sons, 1952.
- [4] T.L. Ainsworth, E. Baron, G.E. Brown, J. Cooperstein and M. Prakash, *Nucl. Phys.* A464 (1987) 740-768.
- [5] Jan Helm, "New Solutions to the TOV equation and on Kerr space-time with matter and the corresponding star models", 2014.
- [6] P. Haensel, A.Y. Potekhin, D.G. Yakovlev, "Neutron Stars I Equation of State and structure", Springer 2007.
- [7] Nicolas Chamel and Paweł Haensel, *Living Rev. Relativity* 11, 2008.
- [8] Richard Silbar, Sanjay Reddy, "Neutron stars", 2004.
- [9] S. Marongwe, *International Journal of Astronomy and Astrophysics*, Vol. 3 No. 3, 2013, pp. 236-242.
- [10] M. Prakash and K.S. Bedell, *Phys. Rev. Rapid Communications* C32 (1985) 1118-1121.

Dedicated to Professor Dr. Sorin Dan Anghel on His 65th Anniversary

STRUCTURAL AND MAGNETIC CHARACTERIZATION OF Fe₃O₄ NANOPARTICLES SYNTHESIZED AT ROOM TEMPERATURE

GABRIELA SOUCA^a, S. MICAN^a, A. STEFANCU^{a,b}, V. CHIȘ^a,
R. TETEAN^a, N. LEOPOLD^{a,b*}

ABSTRACT. Magnetite nanoparticles without surfactants were obtained by room temperature synthesis. X-ray diffraction data show that the nanoparticles crystallize in a cubic single phase structure. An average crystallite size of around 24 nm was calculated. The obtained Fe₃O₄ nanoparticles are ferrimagnetic at 4 K and at 300 K, too. It was shown that a ferrimagnetic to superparamagnetic transition is present, even if the superparamagnetic state is not pure. We assume that the true long-range ferromagnetic coupling is absent due to the small grain size of the sample.

Keywords: magnetite nanoparticles, X-ray diffraction, magnetization

INTRODUCTION

Among engineered nanomaterials, magnetic nanoparticles (MNPs) offer promising possibilities in biomedical field, due to their unique physico-chemical properties, including biocompatibility and magnetic properties that allow them to be manipulated by an external magnetic field gradient [1]. Particularly, nanoparticles made of a ferro- or ferrimagnetic material, i.e., iron oxide nanoparticles (ION), can exhibit a unique form of magnetism called superparamagnetism. This appears when the ION size is below a critical value – depending on the material, but typically around 10 – 20 nm - and the temperature is above a particular temperature which is called

^a Faculty of Physics, Babeş-Bolyai University, Kogălniceanu 1, 400084 Cluj-Napoca, Romania

^b IMOGEN Research Institute, County Clinical Emergency Hospital, Pasteur f.n., 400006 Cluj-Napoca, Romania

* Corresponding author: nicolae.leopold@phys.ubbcluj.ro

the blocking temperature (T_B) [1, 2]. In the superparamagnetic state, the magnetic moments of the nanoparticles fluctuate around the easy axes of magnetization. Thus, each of the MNPs will possess a large magnetic moment that continuously changes orientation. When a magnetic field is applied, MNPs in the superparamagnetic state display a fast response to the changes of the magnetic field without remnant (residual) magnetization. Therefore, in the superparamagnetic state, an MNP behaves as a paramagnetic atom with a giant spin [2]. This superparamagnetic behavior is highly useful in biomedicine for several applications such as contrast agents for magnetic resonance imaging (MRI), sensitizers in hyperthermal methods for cancer treatment, magnetic drug delivery or magnetic biosensors [1, 2].

EXPERIMENTAL

Synthesis of Fe_3O_4 magnetic nanoparticles

A previously reported method was used for synthesis of Fe_3O_4 MNPs without surfactants, at room temperature [3]. Briefly, deionized water (200 ml) was deoxygenated by bubbling nitrogen gas for 1 h in the solution. Afterwards, 25 ml of NH_4OH (1 M) was added and the mixture was stirred with mechanical agitation at 1000 rpm. Then, 1.352 g of $\text{FeCl}_3 \cdot 6\text{H}_2\text{O}$ and 0.695 g $\text{FeSO}_4 \cdot 7\text{H}_2\text{O}$ were separately dissolved in 20 ml and 10 ml deionized and deoxygenated water, respectively. Subsequently, amounts of 10 ml ferrous sulfate and 20 ml ferric chloride solutions were added to the ammonium hydroxide solution and the reaction mixture was stirred for 2.5 min at 1000 rpm. A black precipitate formed (Fig. 1) which was washed four times with deionized water. Finally, the prepared Fe_3O_4 MNPs were separated from the solution with a magnet [4]. Powder samples were obtained by drying on a glass slide, at room temperature.



Fig. 1. Photography of the Fe_3O_4 nanoparticles after synthesis.

X-ray diffraction measurements

The X-ray diffraction (XRD) measurements were performed on powder samples, at room temperature using a Bruker D8 Advance diffractometer with Bragg-Brentano focusing geometry and Cu K_α radiation. The average crystallite size was determined from the full width at half-maximum (FWHM) values of the XRD peaks using the Williamson-Hall method [5]. This method separates size and strain broadening and gives a more accurate value of the average crystallite size [5]. The FWHM values were obtained by fitting each XRD peak using a normalized pseudo-Voigt function. The instrumental broadening, measured from the XRD pattern of a LaB₆ reference sample, was subtracted from the obtained FWHM values. The lattice parameters were determined using Powdercell software version 2.3 made by the Federal Institute for Materials Research and Testing (BAM), Berlin.

Magnetic measurements

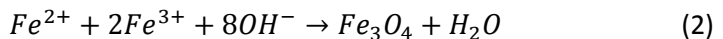
The magnetic measurements between 4 and 300 K were performed using a vibrating sample magnetometer (VSM) made by Cryogenic Limited in applied fields up to 2 T. Both zero-field-cooled (ZFC) and field-cooled (FC) measurements were performed [6]. The saturation magnetization values, M_s , were determined from magnetization curves using the approach to saturation law:

$$M = M_s \left(1 - \frac{b}{H} \right) + \chi_0 H \quad (1)$$

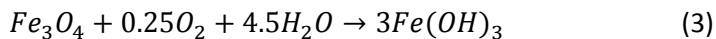
where by b we denoted the coefficient of magnetic hardness and by χ_0 a Pauli-type contribution.

RESULTS AND DISCUSSION

Conventionally, magnetite is prepared by adding a base to an aqueous mixture of Fe²⁺ and Fe³⁺ salt at a 1:2 molar ratio [7]. The overall reaction of Fe₃O₄ precipitation may be written as follows:



The maintaining of a non-oxidizing, oxygen-free environment is critical, otherwise, Fe₃O₄ might also be oxidized as follows:



affecting the physical and chemical properties of the nanosized magnetic particles.

Magnetite particles obtained under different synthetic conditions may display large heterogeneities regarding their magnetic properties. These differences are attributed to changes in structural disorder, creation of antiphase boundaries, or the existence of a magnetically dead layer at the particle surface [7].

Fig 2 shows the XRD patterns at room temperature of the Fe_3O_4 powder. The simulated XRD pattern of Fe_3O_4 generated using the Powdercell software is also shown. The structural model of bulk Fe_3O_4 was used for the simulation [8]. There is a good agreement between the measured and the simulated patterns, indicating that the sample consists of a single phase, Fe_3O_4 .

The nanoparticles crystallize in cubic type structure (space group number 227) [8] as it is demonstrated by the position and the relative intensities of their diffraction peaks, matching well with the standard XRD data for bulk magnetite. There are no peaks of any other phases in the XRD patterns, indicating the high purity of the product. The lattice parameter is $a=8.36 \text{ \AA}$, smaller than the bulk one ($a=8.397 \text{ \AA}$). The sample show very broad peaks which are indicative for small crystallite size of nanoparticles. The average crystallite size was determined to be $24 \pm 1 \text{ nm}$.

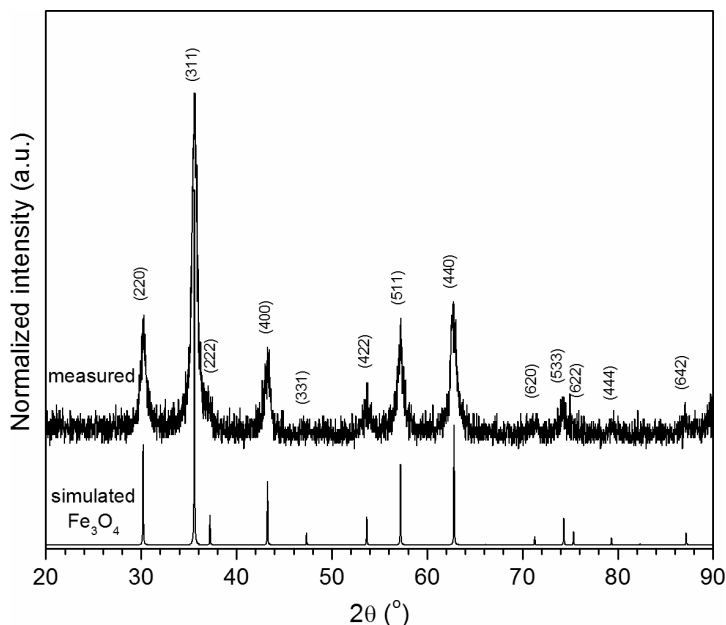


Fig. 2. XRD patterns of the of the Fe_3O_4 powder.

STRUCTURAL AND MAGNETIC CHARACTERIZATION OF Fe_3O_4 NANOPARTICLES
SYNTHESIZED AT ROOM TEMPERATURE

The magnetic measurements indicate that the Fe_3O_4 nanoparticles are ferrimagnetic at 4 K and at 300 K, too (see Fig.3). The saturation magnetization, M_s , values are 77 emu/g at 4 K, respectively 70 emu/g at 300 K. These values are lower than the value of bulk magnetite (~ 92 emu/g at room temperature [9, 10]) and they are comparable with previous reported M_s data [11-13]. The decrease of the saturation magnetization can be attributed to the disorder canting spins at the surface, due to the coordination number imperfections or to the formation of cation vacancies into the crystalline structure during the synthesis [14, 15]. The nanoparticle surface can be composed of some disordered or canted spins and these spins do not allow the core spins to be aligned along the external field direction. This results in a decrease of the saturation magnetization of these small sized nanoparticles.

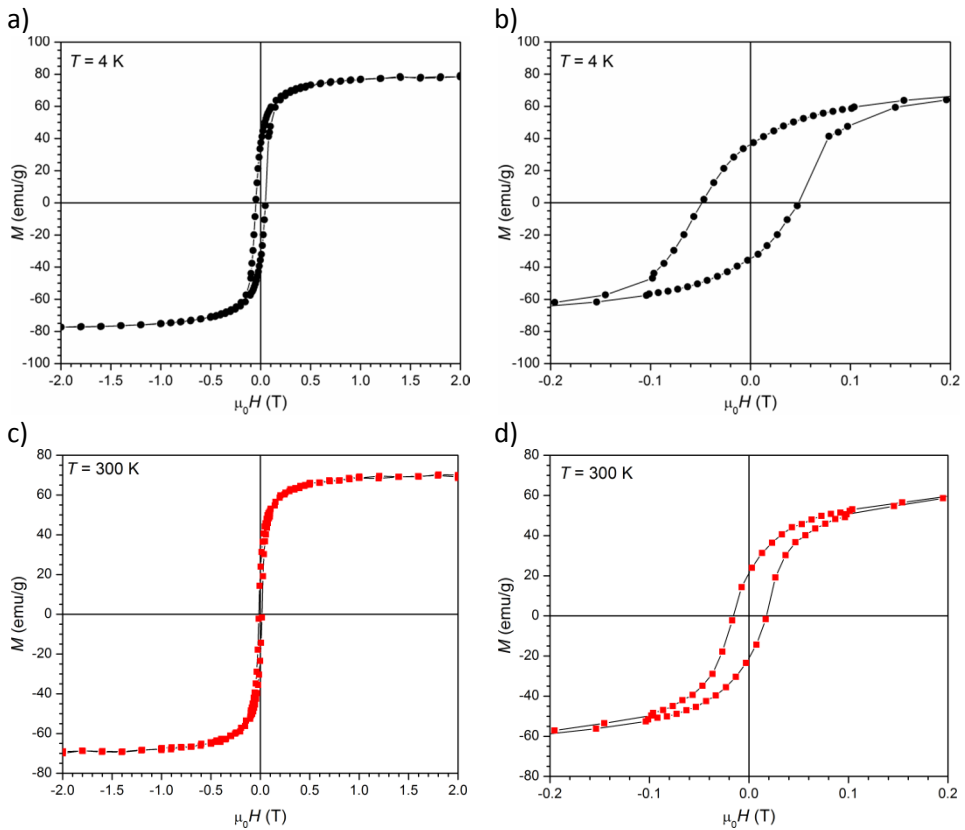


Fig. 3. Magnetic hysteresis loops recorded at 4 K and 300 K.

The coercive field is around 0.046 T at 4 K and decreases to 0.015 T at $T=300$ K which shows that the particles are not in a pure superparamagnetic state. The coercive fields values increase while the temperature decreased suggesting that the nanoparticle undergo a superparamagnetic to ferrimagnetic transition.

To get more insights into the magnetic behaviour, the thermal dependence of the magnetization in field cooling (FC) and zero field cooling (ZFC) has been recorded in a 0.05 T field between 4 K and 300 K. The ZFC curves show a broad maximum centred at around 133 K (see Fig.4) and below this temperature the magnetization decreases with decreasing temperature while the FC magnetization increase continuously down to 4 K. This behaviour indicates a gradual transition which corresponds to the average onset of the ferrimagnetic to superparamagnetic transition, even if the superparamagnetic state is not pure.

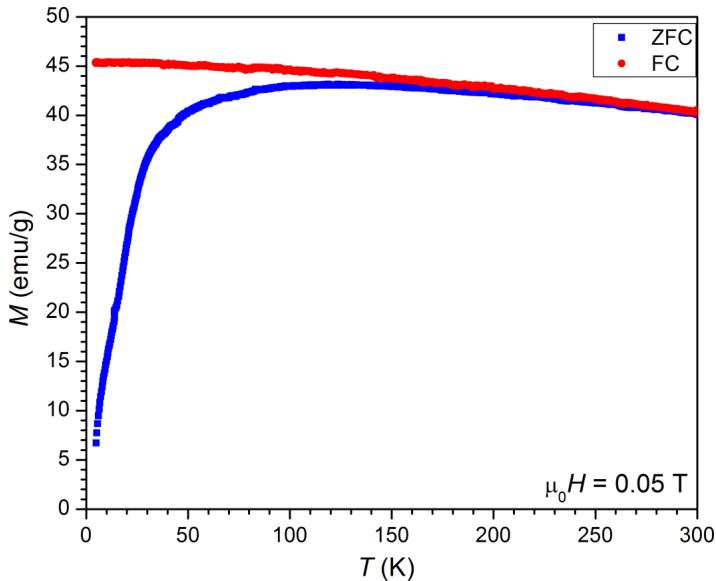


Fig. 4. Temperature dependence of zero-field cooled and field cooled magnetization in 0.05 T.

The $M(T)$ values of FC curves can provide information about the inter-particle interaction strength [16]. It was reported that larger grain-sizes are favourable for stronger long-range ferromagnetic (FM) coupling, while grains with smaller sizes can create heavier strain at the grain boundaries and give rise to more non-FM or weak antiferromagnetic regions which can disturb the long-range FM order [17]. In our system, the true long-range FM coupling is absent due to the small grain size of the samples.

The magnetic properties suggest the possibility of using these nanoparticles on large scale applications.

CONCLUSIONS

Magnetite nanoparticles with crystallite average size of 24 nm were obtained by a simple synthesis route, at room temperature. The magnetic measurements indicate that the Fe₃O₄ nanoparticles are ferrimagnetic at 4 K and at 300 K, too. Their saturation magnetization, M_s , values being 77 emu/g at 4 K, respectively 70 emu/g at 300 K, lower values than the value of bulk magnetite. The coercive field values increase while the temperature decreases, suggesting that the nanoparticles undergo a superparamagnetic to ferrimagnetic transition. The coercive field was found to be around 0.046 T at 4 K and decreases to 0.015 T at $T=300$ K which indicates that the particles are not in a pure superparamagnetic state. The ZFC curve recorded between 4 K and 300 K shows a broad maximum centred at around 133 K and below this temperature the magnetization decreases with decreasing temperature, while the FC magnetization increases continuously, down to 4 K. This behaviour indicates a gradual transition which corresponds to the average onset of the ferrimagnetic to superparamagnetic transition, even if the superparamagnetic state is not pure.

ACKNOWLEDGMENTS

NL and AS acknowledge support from the Competitiveness Operational Programme 2014-2020 POC-A1-A1.1.4-E-2015, financed under the European Regional Development Fund, project number P37_245.

REFERENCES

1. V. Valdiglesias, N. Fernández-Bertólez, G. Kiliç, C. Costa, S. Costa, S. Fraga, M.J. Bessa, E. Pásaro, J.P. Teixeira, B. Laffon, *J. Trace Elem. Med. Biol.*, 38, 53 (2016).
2. B. Issa, I.M. Obaidat, B.A. Albiss, Y. Haik, *Int. J. Mol. Sci.*, 14, 21266 (2013).
3. I. Martínez-Mera, M.E. Espinosa-Pesqueira, R. Pérez-Hernández, J. Arenas-Alatorre, *Mater. Lett.*, 61, 4447 (2007).
4. M. Yazdi, Z.N. Najafi, M. Khorramizadeh, M. Amini, A. Shahverdi, *DARU, J. Pharm. Sci.*, 20 (2012).

5. G.K. Williamson, W.H. Hall, *Acta Metall*, 1, 22 (1953).
6. I.J. Bruvera, P. Mendoza Zélis, M. Pilar Calatayud, G.F. Goya, F.H. Sánchez, *J. Appl. Phys.*, 118, 184304 (2015).
7. A.K. Gupta, M. Gupta, *Biomaterials*, 26, 3995 (2005).
8. N. Tzafaras, W. Adlhart, H. Jagodzinski, *Acta Cryst. A*, 37A, C-104 (1981).
9. A.G. Roca, J.F. Marco, M. Del Puerto Morales, C.J. Serna, *J. Phys. Chem. C.*, 111, 18577 (2007).
10. B. Wang, Q. Wei, S. Qu, *International J. Electrochem. Soc.*, 8, 3786 (2013).
11. C. Salazar-Camacho, M. Villalobos, M.D.L.L. Rivas-Sánchez, J. Arenas-Alatorre, J. Alcaraz Cienfuegos, M.E. Gutiérrez-Ruiz, *Chem. Geol.*, 347, 233 (2013).
12. W.S. Peternele, V. Monge Fuentes, M.L. Fascineli, J. Rodrigues Da Silva, R.C. Silva, C.M. Lucci, R. Bentes De Azevedo, *J. Nanomater.*, 2014 Article ID 682985, (2014).
13. S. Rajput, C.U. Pittman, D. Mohan, *J. Colloid. Interface Sci.*, 468, 334 (2016).
14. Y. Zhang, Z. Yang, D. Yin, Y. Liu, C. Fei, R. Xiong, J. Shi, G. Yan, *J. Magn. Magn. Mater.*, 322, 3470 (2010).
15. V. Kumar, A. Rana, M.S. Yadav, R.P. Pant, *J. Magn. Magn. Mater.*, 320, 1729 (2008).
16. I. Andreu, E. Natividad, L. Solozábal, O. Roubeau, *ACS Nano*, 9, 1408 (2015).
17. E. Taşarkuyu, A. Coşkun, A.E. Irmak, S. Aktürk, G. Ünlü, Y. Samancıolu, A. Yücel, C. Sarikürkçü, S. Aksoy, M. Acet, *J. Alloys Compd.*, 509, 3717 (2011).

Dedicated to Professor Dr. Sorin Dan Anghel on His 65th Anniversary

SIMPLE METHOD FOR INVESTIGATION OF LOW FREQUENCY DAMPED OSCILLATIONS OF ELASTOMERS

M. TODICA^{a*}, C. V. POP^a AND O. BALIBANU^a

ABSTRACT. A simple method for digital data recording of mechanical low frequency oscillations has been proposed. The methods was applied to measurements the elastic constant, attenuation and viscosity coefficients of elastomers. Such parameters can be difficult measure by other methods for polymers with low flow, like the elastomers.

Keywords: *digital data recording, low frequency oscillations, elastomers*

INTRODUCTION

Studding the mechanical oscillation in not a novelty, being performed with simplest methods since the eve of modern physics, but the methods of performing such study are subject of continuously change, in function of the development of new equipments for observation and data acquisition. The classic methods suppose the use of very simplest instruments, watch, for time measuring, ruler, for distance measurement, and scale, for mass measurements. Such method allows better observation and understanding of physical phenomena and measuring principles, but the precision of the measurement is low. Other disadvantage is the fact that the data must be collected and introduced manually in the computer for digital analyze. The modern methods are based on the use of complex equipments, containing a lot of different kind of sensors, which can be regarded as “black box”, with one entry and one output. The user starts the experiment, the equipment collects and processes the data and provides directly on its output the parameters of the

^a “Babes-Bolyai” University, Faculty of Physics, M. Kogalniceanu No 1, 400084 Cluj-Napoca, Romania
* Corresponding author: mihai.todica@phys.ubbcluj.ro

physical phenomena. The user cannot see how the data were collected and processed. It is a great disadvantage. On the other hand such equipments are expensive and not accessible for all the scholar communities, especially for poor regions.

The aims of this work in to present a method of investigation of low frequency oscillations which combines the advantages of classic observation of the phenomena with the new method of digital data acquisition. The great advantage is that the equipment can be "home made", the most expensive component being an ordinary computer. In addition the user can themselves set the parameters of the experiment and data acquisition, fact that allows better understanding of the process. Finally the method can be used for effective investigation of very low frequency oscillation of polymeric systems, allowing the measurement of elastic modulus and viscosity coefficient.

The elastomers, below the glass transition temperature, have predominant elastic behavior and look like solid elastics, without flow, [1-4]. However they have also viscoelastic properties, but the viscosity parameters cannot be measured in solid state with standard viscosimetric methods. For viscosity measurements the material must be melts or dissolved in good solvent [5]. The parameters obtained by this way are not consistent for the characterization of the material in the solid state phase. A method for measuring these parameters in solid state is necessarily. That is a new feature of our experiment. The viscoelastic parameters can be obtained from the parameters of damped oscillations.

EXPERIMENTAL

The main piece of the experimental set-up is the unbalanced transformers, home made. It has symmetrically structure consisting on three coils, wired linearly along a cylindrical support, 8 cm length and 1.1 cm inner diameter (Fig. 1). In the middle of the structure is the inductor coil L , 1 cm length, which contains 200 turns of cooper wire with $\Phi = 0.35$ mm, (CuEm 0.35), wired on multi layers. Symmetrically, on the right and the left sides, there are the two coils, L_1 and L_2 of the induced part of the transformer. Each coil is 2.5 cm long and contains 200 turns, CuEm 0.35 mm, wired on multilayer. These coils are wired in the same direction, but theirs ends are connected in opposite position, so that the induced tensions will be in opposite phase. The core of the transformer consists on the ferrite bar with 8 mm diameter and 11 cm length. This bar represents the mass of the oscillating system. It is attached to the rubber strip of 30 cm length. The strip and the ferrite bar together form the

oscillating system. The polymeric strip is introduced inside a glass tube, with inner diameter 3 cm, containing a thermometer and a heating resistor. This represents a simple heating system, allowing the study of oscillations at many temperatures. The ferrite bar oscillates freely inside the transformer. All the components are placed in vertical position, avoiding the apparition of the friction between the ferrite bar and the inner part of the transformer. At equilibrium the ferrite bar is situated in the middle of the transformer. The inductor coil of the transformer is connected to the headphone jack or line output of sound card of the PC. It will be supplied by the audio frequency signal provided by the generator signal of the Scope software. The induced coils are connected to the microphone entry of the PC and will provide the signal which will be visualized and recorded by the Scope software.

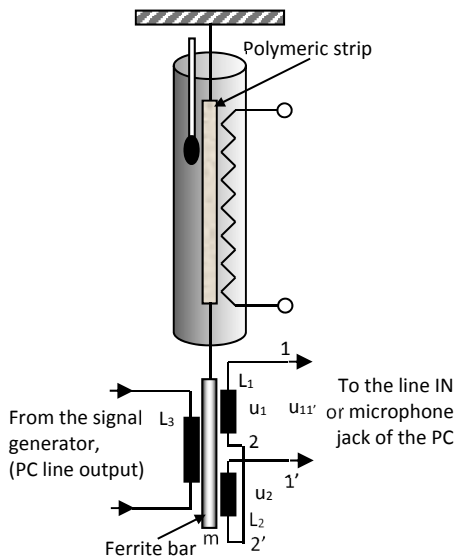


Fig. 1. Experimental set-up of the oscillating system

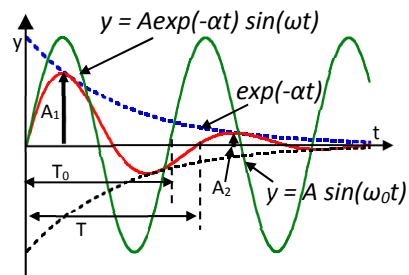


Fig. 2. Graphic representation of the ideal and damped oscillations for a system with elastic constant k , mass m and attenuation coefficient α .

The second element of the set-up is the software Scope 1.4.1., offered freely on the internet by Zeinitz [6]. This software allows the use of any PC with sound card as oscilloscope with 2 channels in the range 20 – 20000 Hz. It provides also a signal generator in the same range of frequencies. The entry of scope is set to be connected to the microphone or line IN of the PC, and will receive the signal induced into the coils L_1 and L_2 . The output of the signal generator is set to be

connected to the line output or headphone output of the sound card of PC. The connections and all the parameters of the experiment, the frequency, the base time, the gain and the amplitude of the generated signal, can be set from the software. We set the frequency at 824 Hz and the amplitude of generated signal 0.5 V. When the ferrite bar is situated in the middle of the transformer, the tensions u_1 and u_2 induced in the coils L_1 and L_2 of the transformer are identically, but in opposite phase, so that the tension available on the ends 1 and 1' of the transformer is zero. If the ferrite bar is displaced from its equilibrium position, the tensions induced in the coils L_1 and L_2 are not equals, and the resulting tensions on the ends 1-1', $u_{11'} = u_1 - u_2 \neq 0$ will be different from zero. The difference is proportional with the displacement of the ferrite bar from its equilibrium position. If the ferrite is oscillating, the tension $u_{11'}$ will have the amplitude depending on the elongation of the oscillation. We obtain an oscillation with frequency $\nu_0 = 824\text{Hz}$ modulated in amplitude by the mechanical oscillation.

RESULTS AND DISCUSSIONS

Low frequency damped oscillations can appear in polymeric systems, especially in the elastomers, above the glass transition temperature. The attenuation of oscillations is very high, so that the duration of the oscillating motions involves only few oscillations. Depending on the elastic modulus of the polymer, and the mass of the oscillating system, the frequency of the oscillations can be of few hertz. Such oscillations cannot be seen directly with the oscilloscope as continuously trace curve due to the refresh rate of the screen, which is much greater than the frequency of the oscillation. Only a fraction of oscillation

$\frac{T_{osc}}{T_{refresh}} = f$ will be displayed on the screen of the oscilloscope. The oscilloscope

can easily displays signals with higher frequencies, [9]. The idea is to modulate a relatively high frequency signal, the carrier frequency, with the low frequency of mechanical oscillation. The oscilloscope is set to display stable image of the carrier signal. The stability of image is not affected by the modulation. As presented in the experimental section this purpose is achieved with an unbalanced transformer. The modulation is realized by the mechanical oscillation.

An elastomer is a viscoelastic system which can be represented by an ideal spring connected in parallel with a shock absorber. The oscillating behavior of the spring is described by Hook's law, $\vec{F} = -k \cdot \vec{y}$, where the k represents the elastic

constant of the polymer and y represents the elongation of the spring. The shock absorber is described by Newton's law, $F = \eta \cdot \frac{dy}{dt}$, where η represents the viscosity of the material and $\frac{dy}{dt}$ represents the rate of deformation [7]. The motion of such oscillating system is described by the equation:

$$m \frac{d^2 y}{dt^2} = -ky - \eta \frac{dy}{dt} \quad (1)$$

The solution of this equation is a damped oscillation:

$$y = A \cdot \exp(-\alpha t) \cdot \sin(\omega t) \quad (2)$$

A represents the amplitude, α the attenuation coefficient and ω the pulsation of the damped oscillation. The relation existing between the parameters α , ω , m and k are described by the equations:

$$\alpha = \frac{\eta}{2m}, \quad \omega^2 = \frac{k}{m} - \frac{\eta^2}{4m^2} \quad (3)$$

The period of the damped oscillation $T = \frac{2\pi}{\omega}$ is greater than the period of the ideal oscillations $T_0 = \frac{2\pi}{\omega_0}$, where $\omega_0^2 = \frac{k}{m}$ and $T_0 = \sqrt{\frac{m}{k}}$, [8]. The graphic representation of ideal and damped oscillation is presented in figure 2. Experimentally we can measure the period and the amplitude of the damped oscillations. The amplitude is affected only by the attenuation coefficient α following an exponential law. Measuring the amplitude of damped oscillations at the moments T_i , we can calculate the attenuation coefficient α from the representation:

$$A(T_i) = A_0 \exp(-\alpha T_i) \quad (4)$$

Another way is the use of logarithmic decrement of the oscillations, $A = \frac{A_2}{A_1}$. To do this we must measure the amplitudes A_1 , A_2 of two successive

oscillations separated by a time interval equal with a period. Λ represents the rate of loss of mechanical energy W during a period. Taking into account the attenuation of the amplitude, we can find a direct relation between α and Λ .

$$\frac{W_2}{W_1} = \exp(-2\alpha T) = \Lambda^2 \quad \alpha = -\frac{\ln \Lambda}{T} \quad (5)$$

Knowing α , η , m , T we can calculate the viscosity coefficient η . This result is very important, allowing the calculation of the viscoelastic coefficient for polymeric materials with very low flow, as the elastomers. For such materials the classic measurements with viscometers are not possible because the materials are in solid state.

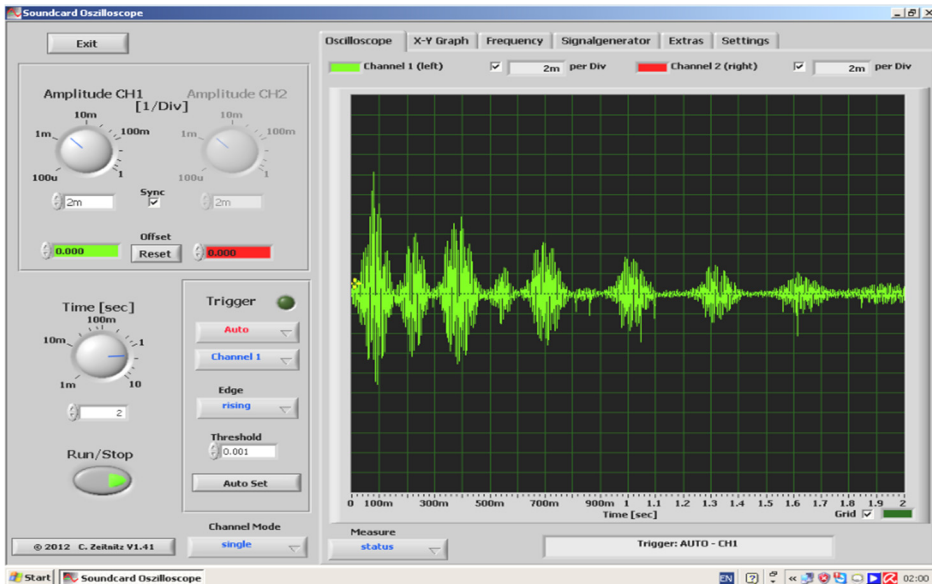


Fig. 3. The set-up control panel of the oscilloscope and the recorded damped oscillations

The experimental oscillations obtained by us are presented in figure 3 and the set-up of the signal generator in figure 4. The data, on digital form, were collected directly and stored with the Scope 1.4.1. software and then processed with Kaleidagraph software. The data, as recorded, contain both the carrier frequency and the modulator signal, Fig. 3. In the first stage of analyze, the carrier

frequency is eliminated, Fig. 5. From this data we calculated the period T of the damped oscillations and we read the amplitudes $A(T_i)$ of the oscillations. We found the value $T = 0.25$ s. Using the equation $A(T_i) = A_0 \exp(-\alpha T_i)$ we calculated the attenuation coefficient α . We found the value $\alpha = 6.4$ s⁻¹. The value of α was also calculated from the logarithmic decrement of the oscillations. We took two successively values of amplitudes $A_1 = 1.86$ and $A_2 = 0.37$. We used the equation 5 for calculation. We obtained the value $\alpha = 6.46$ s⁻¹. The values determined by both methods are in good agreement. Using this value of α , the measured values of T and m , we calculated the viscosity coefficient η with the equation $\eta = 2m \cdot \alpha$. We found the value $\eta = 0.5$ Ns/m. We calculated also the elastic constant k with the equation (3). We found the value $k = 25$ N/m. To verify our result, we used the values α , η , m and T to fit the experimental data with the equation (2). The result of the fit is shown in figure 6. We can see a good agreement between experimental data and simulation.

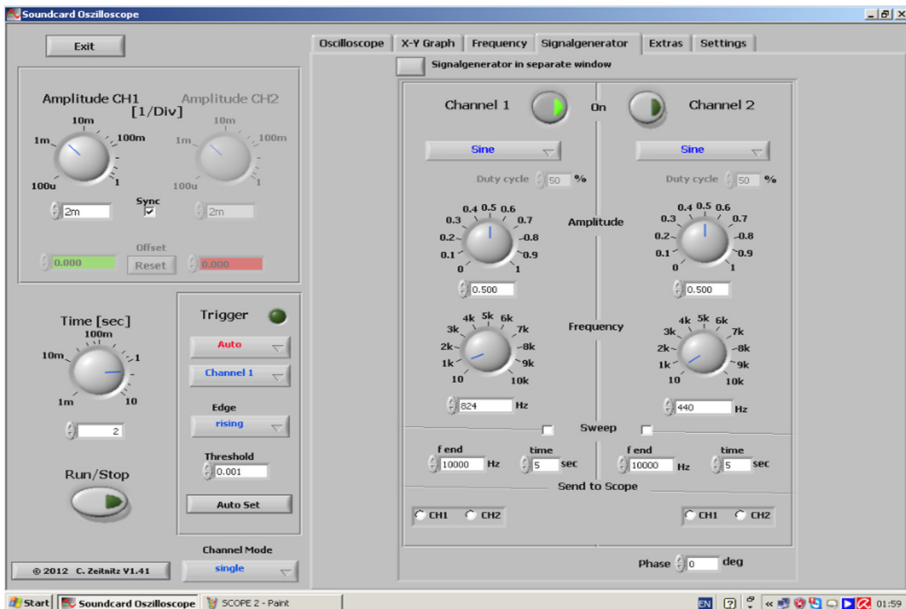


Fig. 4. The set-up control panel of the signal generator

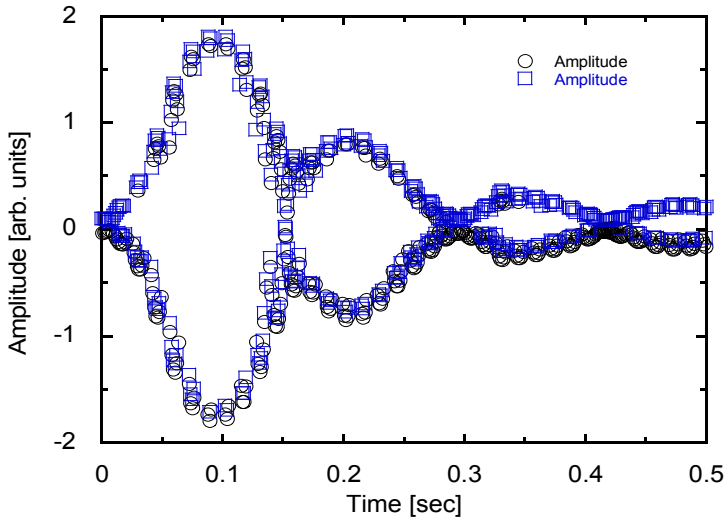


Fig. 5. The modulator signal after elimination of the carrier signal

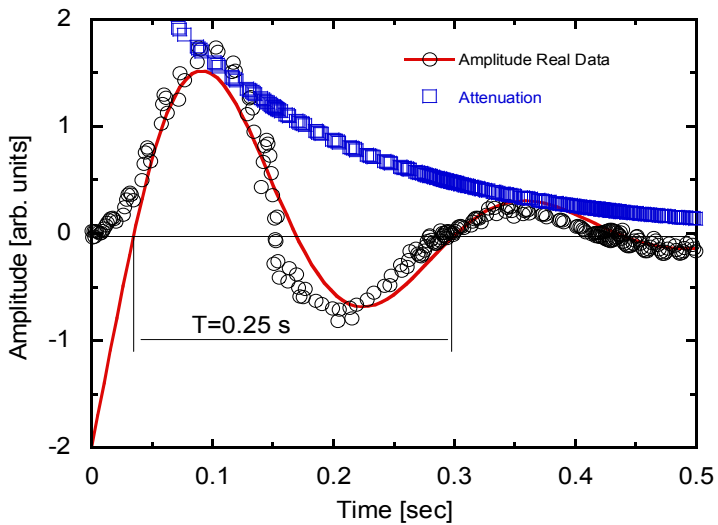


Fig. 6. The fit of the modulator signal with the equation 2

CONCLUSION

A simple method for digital data recording of low frequency mechanical oscillations was presented. The method can be used for the investigation of the elastomers, allowing quantitative measurement of some parameters, like the elastic constant, attenuation and viscosity coefficients. Such data can be difficult to obtain by other ways for such materials. The method is based on the use of very simple equipment, which can be "home made", and free software available on the internet. Apart from the scientific character and the usefulness for the characterization of the elastomers, the method has a pronounced didactic character, allowing the user to better understand the principle of digital recording of low frequency mechanical oscillations.

REFERENCES

1. J. P. Cohen-Addad, *NMR and Fractal Properties of Polymers Liquids and Gels*, Pergamon Press, London, 1992.
2. J. P. Cohen-Addad, *Physical Properties of Polymeric Gels*, John Wiley and Sons, Chichester, New-York, Toronto, 1996.
3. P. G. de Gennes, *Scaling Concepts in Polymer Physics*, Cornell University Press, Ithaca, London, 1979.
4. P. J. Flory, *Principles of Polymer Chemistry*, Cornell University Press, Ithaca, New York, 1953.
5. M. Todica, C. V. Pop, *Fizica generala aplicata*, Presa Universitara Clujeana, 2007, ISBN (10)973-610-498-2; ISBN (13) 978-973-610-498-5
6. <http://en.freedownloadmanager.org/Windows-PC/Soundcard-Oscilloscop.html>
7. M. Todica, *Proprietati fizice ale polimerilor*, Presa Universitara Clujeana, 2005, ISBN 973-610-376-5
8. Robert M. Eisberg, Lawrence S. Lerner, *Physics Foundations and Applications*, ISBN 0-07-066268-1, McGraw-Hill, London, 1982
9. S. D. Anghel, *Bazele Electronicii analogice si digitale*, Presa Universitară Clujeană, ISBN: 978-973-610-554-8, 2007

Dedicated to Professor Dr. Sorin Dan Anghel on His 65th Anniversary

FORMULATION AND OPTIMIZING OF A ANTI-AGING COSMETIC CREAM

A. M. JUNCAN^{a*}, C. LUNGB

ABSTRACT. The research and development of cosmetics, especially the composite active ingredients, should be based on their clarified sources, structures, interactive mechanisms with the skin, and, most importantly, their efficacy and safety on the targeted components of skin. This study has as main objective the development and formulation of a anti-aging cosmetic product which incorporates effective and innovative ingredients, used in the developed formulation to support the cosmetic claimed of the product. An important study is the quality control of the anti-aging cream by determining the physico-chemical characteristics and appropriate pharmacotechnical (pH, viscosity) characteristics, both initially and over time (30 days from the preparation of the product).

The formulation is monitored under accelerated stability studies over a period of 30 days while maintaining the product at 4, 20 and 40 °C.

Keywords: *anti-aging cosmetic cream, physico-chemical characteristics, accelerated stability studies.*

INTRODUCTION

Cosmetics are commercially available products that are used to improve the appearance of the skin. Consumer demand for more effective products that more substantively beautify the appearance has resulted in increased basic science research and product development in the cosmetics industry. The result

^a "Lucian Blaga" University of Sibiu, Faculty of Medicine, Lucian Blaga Str. 2A, Sibiu, 550169, Romania.

^b "Babes-Bolyai" University, Faculty of Physics, Mihail Kogalniceanu Str. 1, 400084, Cluj-Napoca, Romania.

* Corresponding author e-mail: ancamaria.juncan@ulbsibiu.ro

has been more ingredients that may actually improve not just the appearance of the skin, but the health of the skin as well. We now have products that renew, restore, and rejuvenate—not just cleanse, protect, and moisturize. [1,2].

Skin aging is characterized by a progressive deterioration of the skin's functional properties, linked to alterations of dermal connective tissue due to the changes at the cell, gene and protein levels. Skin aging can be divided into two basic processes: intrinsic aging and photoaging [3].

Cutaneous ageing can be defined as the result of two different and cumulated processes: intrinsic and extrinsic ageing (also known as photoageing). While intrinsic ageing is natural and mainly due to the passage of time (influence of genetic factors, oxidative stress, cellular senescence etc.) and its consequences, photoageing is mainly linked with the detrimental effects of solar exposure on the skin, although pollution, diet and smoking are also contributing factors [4].

Skin barrier function, principally the stratum corneum, is the primary line of defence against extrinsic stress such as UV-induced photo-damage, microbial infections and physical deterioration resulting from ageing and environmental exposure. Scientific evidence suggests that both intrinsic and environmental factors contribute to „compromised” skin barrier function. The stratum corneum functions as an effective barrier and is critical for controlling and preventing water loss [5].

Ageing affects all levels of the skin. From the stratum corneum downwards aging creates corneocyte dysfunction, epidermal atrophy, dysplasia and abnormal pigmentation (Figure 1) [6, 7]. Aging occurs in all organs of the body; however, the skin appearance, such as wrinkles and furrows, is markedly observed for aging notices. It is a challenging work for cosmetic scientists to find the means for reducing the changes on the skin appearance due to aging. Wrinkles appear over time due to changes in the support structures of the skin from chronological ageing, but photoageing speeds the process considerably leading to quickly formed, deep wrinkles [8].

Skincare products that affect wrinkles are a reality and are well established in consumer, practitioner and corporate perspectives. In the broadest definition, “products” range from classic and simple cosmetic preparations through vitamins, antioxidants, topical and oral cosmeceutical and pharmaceutical preparations, and even to surgical and laser interventions [9]. Application of cosmetic products containing oils with antioxidant activity is widely acceptable to benefit healthy skin [10].

Regardless of the etiology of skin aging, there are important characteristics of aged skin that must be considered. These changes occur throughout the epidermis, dermis, and subcutaneous tissue and can result in wide-ranging alterations in the topography of the skin [11].

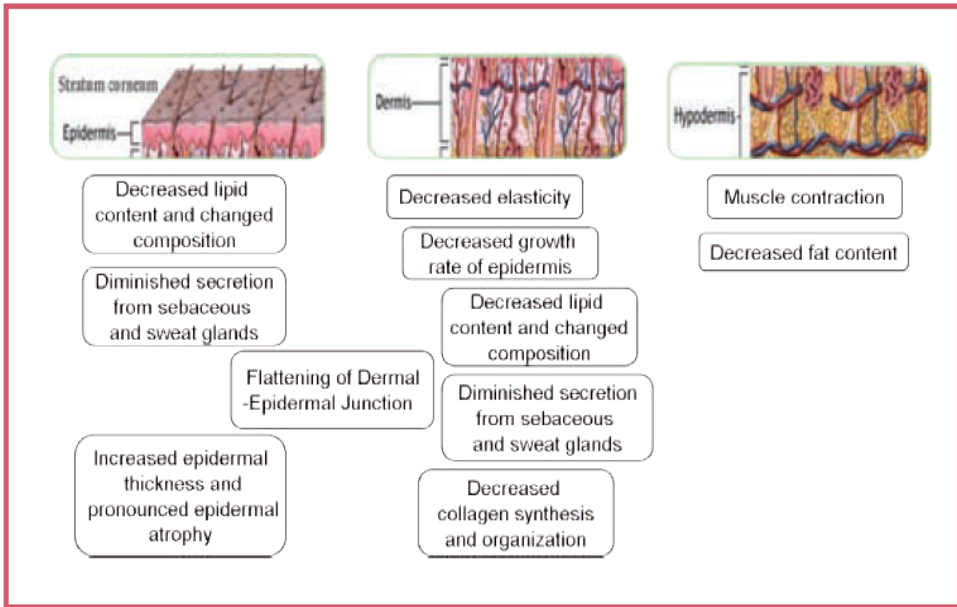


Fig. 1. Changes occurring in aged skin layers

The clinical characteristics of photoaged skin are more pronounced compared with those observed in intrinsic aging (Table1) [12]:

Table 1. Clinical characteristics of intrinsic aging and photoaging

Clinical characteristic	Intrinsic aging	Photoaging
Pigmentation	Pale, white, hypopigmentation	Mottled, confluent, and focal hyperpigmentation
Wrinkling	Fine lines	Deep furrows
Hydration	Dry and flakey	Dry and rough
Growths	Benign	Cancerous and benign

There are a lot of treatments boasting the capability to improve wrinkles: pharmaceutical, surgical and cosmetic solutions. These treatments are intended to change the nature of ageing collagen, stretch the skin, fill in the depressions of the skin or paralyse the muscles that cause the wrinkle. Retinoid products, for example, act by inhibiting enzymes from breaking down collagen, but they may produce redness, burning and general discomfort [10]; alpha-hydroxy acids penetrate

into the top layer of the skin, producing only subtle improvement, though, and causing a mild and temporary irritation, increasing the skin's sensitivity to the sun and particularly increasing the possibility of sunburn [13].

Wrinkle cosmetic treatment is exerted by a variety of active functional ingredients: modern anti-ageing cosmetics go well beyond the simple moisturizing function of traditional anti-wrinkle creams, by exerting a more complex function in protecting the skin from external injuries, nourishing it, and removing its superficial layers. That is the reason why the term "cosmetceuticals" is increasingly used: there are many cosmetic products that fit into this category defined in the regulatory systems of some countries [14].

The anti-aging "active" ingredients, are cosmetic products with properties very similar to a pharmaceutical product (drug-like benefits)- cosmeceuticals [9].

EXPERIMENTAL

Qualitative data of the anti-aging cream formulation is presented in Table 2.

Figure 2 shows by comparison, the composition of the studied cream. The different ratios between lipophilic and hydrophilic components are noticed.

Table 2. Qualitative formulation Anti-aging cream

Anti-Aging Cream				
Phase	Ingredient	INCI designation	Function	Supplier
A	Deionised Water	Aqua	solvent	
	Glycerol	Glycerin	denaturant/humectant/ solvent	Dr. Straetmans
	dermofeel® PA-3	Sodium Phytate, Aqua	chelating	Dr. Straetmans
	dermosoft® LP	Caprylyl Glycol, Glycerin, Glyceryl Caprylate, Phenylpropanol	preservative	Dr. Straetmans
A1	Rapithix A 100	Sodium Polyacrylate	viscosity controlling / binding / film forming	ISP
	Keltrol RD	Xanthan Gum	binding/emulsion stabilising/viscosity controlling/gel forming	CP Kelco
B	symbio® muls CG	Glyceryl Stearate Citrate, Cetearyl Alcohol, Glyceryl Caprylate	emollient / emulsifying/ skin conditioning	Dr. Straetmans
	Plantec Natural Shea Butter	Butyrospermum Parkii	skin conditioning/emollient	SOPHIM

FORMULATION AND OPTIMIZING OF A ANTI-AGING COSMETIC CREAM

Phase	Ingredient	INCI designation	Function	Supplier
	Fitoderm	Squalane	emollient/skin conditioning	Cognis
	dermofeel® sensolv	Isoamyl Laurate	emollient / skin conditioning	Dr. Straetmans
	DC 345 Fluid	Cyclopentasiloxane, Cyclohexasiloxane	emollient /	Dow Corning
	Almond oil	Prunus Amygdalus Dulcis Oil	emollient / skin conditioning	SOPHIM
	dermofeel® E 74 A	Tocopheryl Acetate, Helianthus Annuus (Sunflower) Seed Oil	antioxidant	Dr. Straetmans
C	<i>Biomimetic Collagen</i>	<i>Glycine, Proline, Hydroxyproline</i>	active ingredient	M&G Cosmetics
	<i>Red Wine Extract</i>	<i>VITIS VINIFERA EXTRACT</i>	active ingredient	M&G Cosmetics
D	Parf. Kenzomo D'ete	Parfum	parfum	CPL

STANDARDS AND REAGENTS

Sample preparation of the anti-aging cream

Phase A (demineralized water, dermorganics® Glycerin (Glycerin), dermofeel® PA-3 (Sodium Phytate, Aqua), dermosoft® LP (Caprylyl Glycol, Glycerin, Glyceryl Caprylate, Phenylpropanol)) was heated at 80°C. Phase A1 (xanthan gum and Sodium Polyacrylate) was dispersed in phase A.

Phase B (symbio®muls CG (Glyceryl Stearate Citrate, Cetearyl Alcohol, Glyceryl Caprylate), Plantec Natural Shea Butter (Butyrospermum Parkii), Fitoderm (Squalane), dermofeel®sensolv (Isoamyl Laurate), DC 345 Fluid (Cyclopentasiloxane, Cyclohexasiloxane), dermofeel® E 74 A (Tocopheryl Acetate, Helianthus Annuus (Sunflower) Seed Oil) and almond oil) was melted on water bath at 75°C. Phase A was emulsified with phase B under stirring and cooling down to 40°C was started under medium stirring.

Phase C (Biomimetic Collagen (Glycine, Proline, Hydroxyproline) and red grape extract (Vitis Vinifera Extract) was added under stirring.

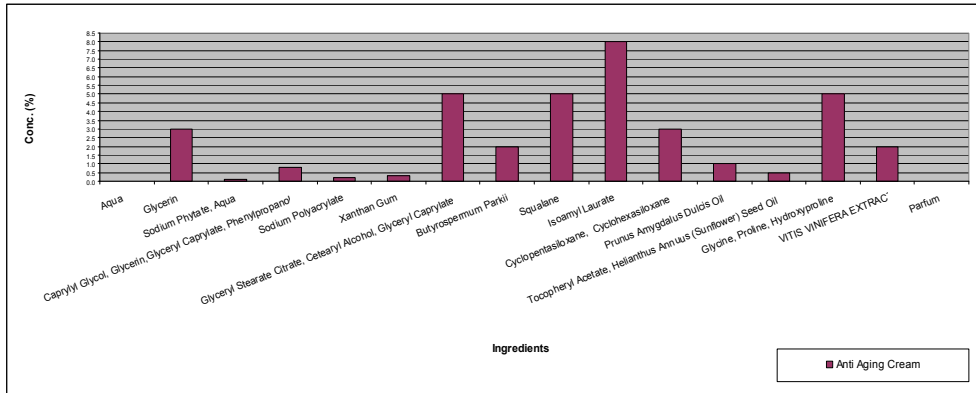


Fig. 2. The composition of the Anti-aging cream

Physico-chemical characteristics of the developed Anti-aging cream-relevant characteristics, acceptance criteria, test methods

Quality control consisted of the following determinations:

Appearance

The appearance, color and odor were tested organoleptically.

pH determination

Was performed using a pH meter (Mettler Toledo (Schwerzenbach, Switzerland)).

Determination of the viscosity

Was performed using a HAAKE Viscotester VT550 (spindle R = 6, shear rate $D=5 \text{ s}^{-1}$, temperature $T=20^{\circ} \text{C}$).

Accelerated stability studies

The developed cosmetic formulation was monitored under accelerated stability studies. Accelerated stability tests were performed over a period of 30 days while maintaining the product at 4, 20 and 40 ° C.

RESULTS AND DISCUSSION

Presentation of the developed cosmetic formulation

The anti-aging cream formulation associates a complex of fats and oils that play an essential role in restoring the hydro-lipid protective skin barrier, contributing to a highly softening, nourishing and moisturizing the sensitive skin, affected by external factors, dehydrated and wrinkled, with red wine extract having regenerative properties, collagen and alpha tocopherol acetate with anti-aging action for the skin.

Natural almond oil is recognized for its excellent emollient properties, soothing and nourishing the skin with a good spreadability and without leaving any greasy feeling. Rich in essential fatty acids (oleic, linoleic), triglycerides, proteins, vitamins A, D and E, having a good spreadability almond oil has a geriatric activity on wrinkled skin, reducing fine lines and wrinkle and, improving scleroderma. It concerns cell regeneration, epithelization of superficial wounds, relieves pruritus and sunburn generally to the treatment of inflammation and dryness of the skin caused by eczema, psoriasis, dermatitis.

Phytosqualane has a geriatric type activity on wrinkled skin, reducing fine lines.

Shea butter is known for its excellent softening, moisturizing and nourishing properties with a good spreadability and leaving a non greasy feeling to the skin.

α -tocopheryl acetate (dermofeel[®] E 74 A) is an effective antioxidant, helping to combat skin aging processes caused by free radicals. It softens the skin and improves skin elasticity.

Red wine extract rich in polyphenols, sugars, vitamins and minerals, stimulates, protects, hydrates and regenerates the skin.

The beneficial presence of collagen, natural component of the skin, stimulates young neo-fibrillogenesis and ensures permanent maintenance of skin hydration.

Applied regularly, the anti-aging cosmetic product developed slows the aging process of the skin, reduces wrinkles, improves the appearance of sensitive, irritated, dry skin.

Physico-chemical characteristics of the developed anti-aging cream

Quality control of the developed cosmetic cream revealed: achieving an acceptable cosmetic preparation with elegant appearance and appropriate physico-chemical and pharmacotechnical (pH, viscosity) characteristics.

The initial determination results are shown in Table 3:

Table 3. Initial physico-chemical determination of the cosmetic cream

<i>Nr.</i>	<i>Properties</i>	<i>Admissibility conditions</i>
1.	Appearance	homogeneous emulsion
2.	Colour	soft light white
3.	Odour	characteristic
4.	pH	5- 5,5
5.	Viscosity	20.000 mPas

Accelerated stability studies performed over a period of 30 days, while maintaining the product at 4, 20 and 40°C, showed that the formulated and studied dermatocosmetic product is stable. The results are shown in Table 4:

Table 4. Physico-chemical determination of the cosmetic cream

<i>Test</i>	<i>Admissibility conditions (initial)</i>	<i>Admissibility conditions (after 30 days)</i>
Appearance	homogeneous emulsion	proper
Odour	characteristic	proper
Colour	soft light white	proper
pH	5-5,5	5- 5,5
Viscosity	20.000 mPas	40.000 mPas

CONCLUSIONS

Cosmetics are commercially available products that are used to improve the appearance of the skin. Consumer demand for more effective products that more substantively beautify the appearance has resulted in increased basic

science research and product development in the cosmetics industry. The result has been more ingredients that may actually improve not just the appearance of the skin, but the health of the skin as well. We now have products that renew, restore, and rejuvenate—not just cleanse, protect, and moisturize [1].

The latest innovation in the field of cosmetics is the development of active cosmetics. Currently, cosmetics are not only intended for the improvement of the appearance or odor of the consumer, but are also intended for the benefit of their target, whether it is the skin, the hair, the mucous membrane, or the tooth. With this functional approach, products became diversified and started to claim a multitude of actions on the body. In order for cosmetic products to support these activities, raw materials became more efficacious, safe, bioavailable, and innovative, while remaining affordable. Subsequently, the cosmetic market greatly expanded, becoming accessible to millions of consumers worldwide [9].

The research presented in this paper had as main objective the development and formulation of a anti-aging cosmetic formulation. The developed cosmetic formulation associates valuable emollients- Shea butter, a known emollient in cosmetics for its regenerative and moisturizing effects and Phytosqualane having a geriatric type activity on wrinkled skin, reducing fine lines. The emollient raw materials, respectively Shea butter was added in a 2% concentration in the formulation and Phytosqualane 5%. The concentration of active ingredient has been introduced in the formulation at a concentration of 5% collagen and 2% red wine extract. The cream slows the aging process of the skin, reduces wrinkles and, improves the appearance of sensitive, irritated, dry skin.

Quality control of the developed cosmetic cream revealed: achieving an acceptable cosmetic preparation with elegant appearance and appropriate physico-chemical and pharmacotechnical (pH, viscosity) characteristics (after preparation and after 30 days of preparation).

Accelerated stability studies performed over a period of 30 days, while maintaining the product at 4, 20 and 40°C, showed that the formulated and studied dermatocosmetic product is stable.

ACKNOWLEDGMENTS

Special thanks are extended to Azelis Romania for providing cosmetic ingredients used for the anti-aging cosmetic product formulation.

REFERENCES

1. M. P. Lupo, *Clin.Dermatol.*, 19 (2001).
2. A. M. Juncan, A. L. Vonica-Gligor, „Tendine în dezvoltarea și formularea produselor dermatocosmetice cu efect anti-aging” in *Tendințe și progrese în Medicina Sibiiană VI*, Editura Universității “Lucian Blaga” din Sibiu, Sibiu, **2016**, chapter 10.
3. Y. H. Kim, K. H. Kim, C. S. Han, H. C. Yang, S. H. Park, H.-I. Jang, J.-W. Kim, Y.-S. Choi, N. H. Lee, *J. Cosmet. Sci.*, 61, 2010.
4. F. Perin, *Personal Care Magazine*, 5 (2016).
5. S. Rao, F. Muia, S. Bennett, J. V. Gruber, *Personal Care Magazine*, 5 (2013).
6. N. J.Lowe, *Personal Care Magazine*, 2 (2013).
7. D. Ainbinder, E. Touitou, *H&PC Today - Household and Personal Care Today*, 8, 2 (2013).
8. D. Whitby, J. Allen, *Personal Care Magazine*, 7 (2012).
9. A. Barel, M. Paye, H. I. Maibach, *Handbook of Cosmetic Science and Technology*, Marcel Dekker, New York, **2001**, chapter 46.
10. P. Boonme, *H&PC Today - Household and Personal Care Today*, 6, 1 (2011).
11. L. Baumann, *Cosmetic Dermatology. Principles and Practice*, McGraw-Hill Professional Publishing, New York, 2nd Ed., **2016**, chapter 6.
12. C. M. Burgess, *Cosmetic Dermatology*, Springer, Heidelberg, **2005**, chapter 3.
13. A. Sparavigna, B. Tenconi, I. Deponti, F. Scarci, M. Caserini, F. Mailland, *JCDSA*, 3 (2013).
14. C. Rona, F. Vailati, E. Berardesca, *J. Cosmet. Derm.*, 3 (2004).